

U.S. DEPARTMENT OF COMMERCE
National Technical Information Service

AD-A014 863

THIN FILM OPTICAL WAVEGUIDES IN III-V SEMICONDUCTORS

MONSANTO COMPANY

PREPARED FOR
AIR FORCE CAMBRIDGE RESEARCH LABORATORIES
DEFENSE ADVANCED RESEARCH PROJECTS AGENCY

JANUARY 1975

272114

AFCRL-TR-75-0279

AD A 014863

THIN FILM OPTICAL WAVEGUIDES
IN
III-V SEMICONDUCTORS

by

M. G. Craford
D. L. Keune
D. Finn
W. O. Groves
A. H. Herzog

Monsanto Company
Electronic Products Division
800 N. Lindbergh Boulevard
St. Louis, Missouri 63166

and

W. S. C. Chang
B. L. Sopori
M. W. Muller

Laboratory for Applied Electronic Sciences
Washington University
St. Louis, Missouri 63130

January, 1975

FINAL REPORT
For Period
July 1, 1972 to December 31, 1974

Approved for Public Release; Distribution Unlimited.

Sponsored by

Defense Advanced Research Projects Agency
ARPA Order No. 2074

Monitored by

AIR FORCE CAMBRIDGE RESEARCH LABORATORIES
AIR FORCE SYSTEMS COMMAND
UNITED STATES AIR FORCE
HANSCOM AFB, MASSACHUSETTS 01731

Reproduced by
NATIONAL TECHNICAL
INFORMATION SERVICE
US Department of Commerce
Springfield, VA. 22151

PRICES SUBJECT TO CHANGE

ARPA Order No.:

2074

Contract No.:

F19628-72-C-0324

Program Code No.:

3D10

Principal Investigator & Phone No.:

Dr. D. L. Keune/314 694-3647

Contractor:

Monsanto Co.

AFCRL Project Scientist & Phone No.:

Dr. Andrew C. Yang/617 861-2225

Effective Date of Contract:

1 July 1972

Contract Expiration Date:

31 December 1974

ACCESSION for	
NTIS	White Section <input checked="" type="checkbox"/>
DEC	Black Section <input type="checkbox"/>
UNANNOUNCED	<input type="checkbox"/>
JUSTIFICATION	
BY	
DISTRIBUTION/AVAILABILITY CODES	
Dist.	AVAIL. and/or SPECIAL
A	

Qualified requestors may obtain additional copies from the Defense Documentation Center. All others should apply to the National Technical Information Service.

DOCUMENT CONTROL DATA - R&D		
<i>(Security classification of title, body of abstract and indexing annotation must be entered when the overall report is classified!)</i>		
1. ORIGINATING ACTIVITY (Corporate author) Monsanto Company/Electronic Division 800 N. Lindbergh Boulevard St. Louis, Missouri 63166		2a. REPORT SECURITY CLASSIFICATION Unclassified
		2b. GROUP
3. REPORT TITLE THIN FILM OPTICAL WAVEGUIDES IN III-V SEMICONDUCTORS		
4. DESCRIPTIVE NOTES (Type of report and inclusive dates) Scientific. Final. For period July 1, 1972 to December 31, 1974		
5. AUTHOR(S) (First name, middle initial, last name) M. George Craford, David L. Keune, Donald Finn, Warren O. Groves, and A. H. Herzog, Monsanto Company, and W. S. C. Chang, B. L. Sopori, and M. W. Muller, Laboratory for Applied Elec. Sci., Washington Univ.		
6. REPORT DATE January 1975	7a. TOTAL NO. OF PAGES 164	7b. NO. OF REFS 50
8a. CONTRACT OR GRANT NO. F19628-72-C-G324	8b. ORIGINATOR'S REPORT NUMBER(S) AFCRL-TR-75-0279	
A. PROJECT, TASK, WORK UNIT NOS. 2074 n/a n/a	9b. OTHER REPORT NOS. (Any other numbers that may be assigned this report)	
C. DOD ELEMENT 61101E		
D. DOD SUBELEMENT n/a		
10. DISTRIBUTION STATEMENT A - Approved for public release; distribution unlimited.		
11. SUPPLEMENTARY NOTES This research was supported by the Defense Advanced Research Projects Agency. ARPA Order No. 2074	12. SPONSORING MILITARY ACTIVITY Air Force Cambridge Research Laboratories (LQ) Hanscom AFB, Massachusetts 01731 Contract Monitor: Andrew C. Yang/LQD	
13. ABSTRACT The objectives of this program are (1) to grow a variety of epitaxial GaAs, GaAsP, and GaAlAs waveguide structures, (2) to evaluate their performance for guided wave propagation, and (3) to use and to optimize them for device applications. Most of the samples were grown by the vapor phase epitaxial technique. A few samples were grown by the liquid phase epitaxial technique. The effect of such parameters as layer thickness, alloy composition, surface quality and carrier concentrations on waveguide attenuation has been evaluated at 10.6 μ m wavelength. Some attenuation data have also been collected at 1.06 μ m wavelength. Waveguides with attenuation rate in the range of one to two db/cm have consistently been obtained at both the 10.6 μ m and the 1.06 μ m wavelengths. The use of these waveguides for electrooptical modulation at 10.6 μ m wavelength was analyzed and demonstrated. Comparison of the various waveguides and optimization of the waveguide design for electrooptical modulation has been carried out. A limited amount of effort has also been made to investigate grating couplers and fiber to film coupling. This final report covers the work accomplished during the entire contract period from July 1, 1972, to December 31, 1974. The program may be viewed as consisting of four elements: vapor phase epitaxy, liquid phase epitaxy, waveguide evaluation, and device evaluation. The growth of the epitaxial waveguide structures was carried out in the Electronic Products Division of the Monsanto Commercial Products Company, and the waveguide and device evaluation was subcontracted to the Laboratory for Applied Electronic Sciences, Washington University, St. Louis, Missouri.		

Unclassified

Security Classification

14. KEY WORDS	LINK A		LINK B		LINK C	
	ROLE	WT	ROLE	WT	ROLE	WT
Gallium arsenide Gallium arsenide phosphide Gallium aluminum arsenide Vapor phase epitaxy Liquid phase epitaxy Integrated optics Thin film waveguides Electrooptical modulation Optical attenuation						

ia

Unclassified

Security Classification

TABLE OF CONTENTS

<u>SECTION</u>	<u>PAGE NO.</u>
TABLE OF CONTENTS	i
LIST OF TABLES	iii
LIST OF FIGURES	iv
ABSTRACT	vii
1. INTRODUCTION	1
2. VAPOR PHASE EPITAXY (VPE)	5
2.1 VPE Growth in Production Scale Reactors	6
2.1.1 GaAs/n+GaAs Waveguides	6
2.1.2 GaAs/GaAs _{1-x} P _x Waveguides at 10.6um Wavelength	16
2.1.3 GaAs/GaAs _{1-x} P _x Waveguides at 1.06um Wavelength	31
2.1.4 GaAs/Ga _{1-y} Al _y As Waveguides	33
2.2 Growth of High Resistivity GaAs in Research Scale Reactors	39
3. LIQUID PHASE EPITAXIAL GROWTH OF GaAlAs	43
4. WAVEGUIDE EVALUATION	57
4.1 Planar Waveguide Propagation and Attenuation at 10.6um	57
4.1.1 GaAs/n+GaAs Waveguides	63
4.1.2 GaAs/GaAs _{1-x} P _x Waveguides	69
4.1.3 GaAs/Ga _{1-y} Al _y As Waveguides	73
4.2 Two Dimensional Waveguides at 10.6um	75
4.3 Planar Waveguide Propagation and Attenuation at 1.06um	80
5. DEVICE EVALUATION	84
5.1 Electrooptical Modulation at 10.6um Wavelength	84
5.1.1 Theoretical Calculation	85
5.1.1.1 Phase Modulation in Uniform Thin-Film Waveguides	87

TABLE OF CONTENTS (Cont.)

<u>SECTION</u>	<u>PAGE NO.</u>
5.1.1.2 Amplitude Modulation in Uniform Thin-Film Waveguides	92
5.1.1.3 Electrooptical Modulation in Two-Dimensional Waveguides	96
5.1.2 Experimental Demonstration	109
5.2 Grating and Prism Couplers	114
5.3 Fiber to Thin-Film Coupling	116
6. CONCLUSION	121
7. REFERENCES	123
APPENDIX 1 List of Waveguide Samples Submitted for Evaluation	125
APPENDIX 2 List of Publications	130
APPENDIX 3 Refractive Indices of GaAs, $\text{Ga}_{1-x}\text{Al}_x\text{As}$ and $\text{GaAs}_{1-x}^{\text{P}}_x$	131
A.3.1 Introduction	131
A.3.2 Refractive Index of GaAs	132
A.3.3 Refractive Index of $\text{Al}_x\text{Ga}_{1-x}\text{As}$	133
A.3.4 Refractive Index of $\text{GaAs}_{1-x}^{\text{P}}_x$	138
A.3.5 Conclusion	146
REFERENCES FOR APPENDIX 3	147
APPENDIX A.3.a Refractive Index n and Extinction Coefficient k of Gallium Phosphide as a Function of Wavelength λ .	149
APPENDIX A.3.b Refractive Index of GaP.	151
APPENDIX A.3.c Refractive Index n and Extinction Coefficient k of Gallium Arsenide As a Function of Wavelength λ at 300K.	152

LIST OF TABLES

<u>TABLE NO.</u>	<u>TITLE</u>	<u>PAGE NO.</u>
1	Epitaxial GaAs Film Thickness Uniformity Using a Rotating Disk Holder	10
2	Background Silicon Contamination Level at Original Operating Conditions	11
3	Emission Spectroscopic Analysis of Undoped Epi GaAs - Run No. 5-201	12
4	Effect of Predeposit on the Background Contamination Level	13
5	Effect of Water Addition on the Background Contamination Level	14
6	Effect of the Addition of NH ₃ on the Background Silicon Level in Undoped GaAs	15
7	Undoped Epitaxial GaAs Grown at Modified Growth Conditions	17
8	Undoped GaAs _{1-x} P _x Growth	22
9	Undoped GaAs _{1-x} P _x Growth	23
10	Undoped Epitaxial GaAs Grown on LED GaAs _{1-x} P _x Material	27
11	Undoped GaAs Grown on GaAlAs	38
12	Typical LPE GaAlAs Growth Data from the Large-Area Slider Boat System	54

LIST OF FIGURES

<u>FIGURE NO.</u>	<u>TITLE</u>	<u>PAGE NO.</u>
1	A Typical Wafer Size.	7
2	Schematic diagram of production scale vertical epitaxial reactor.	8
3	Carrier Concentration Profile for VPE GaAs n/n+ Epitaxial Structure	18
4	Schematic of the GaAs/GaAs _{1-x} P _x Waveguide Structure	19
5	Surface alloy composition of GaAs _{1-x} P _x Wafer	25
6	Bow of 5cm GaAs/GaAs _{1-x} P _x wafers as a function of step reduction in phosphorus composition at end of grading period during growth of the alloy	30
7	Surface Corrugations of GaAs/GaAs _{1-x} P _x Waveguides	32
8	Surface of GaAs/GaAlAs VR5-439/MRC 6074-1 50X	35
9	Surface of GaAs/GaAlAs VR5-438/MRC 6074-1 200X	36
10	Surface of GaAs/GaAlAs, VR5-440/MRC 6074-1	37
11	Research Scale LPE Graphite Boat	44
12	Schematic Diagram of Graphite Sliding-Boat Sys.	46
13	Radiant Heat Furnace and Melt Saturation Sys.	47
14	Gas-phase Graphite Melt Saturation Boat	48
15	12-inch Graphite Slider Boat for Growth of Larger-Area GaAlAs Layers	49
16	Loading End of LPE Growth Furnace	51
17	LPE GaAlAs	52
18	Schematic Diagram of the CO ₂ Laser Stabilizer	58
19	The Prism-Prism Coupler Assembly	60
20	Measurements of Attenuation Rate by the Prism-Prism Coupler	61
21	Relative Output Power as a Function of the Path Length	62

LIST OF FIGURES (Cont.)

<u>FIGURE NO.</u>	<u>TITLE</u>	<u>PAGE NO.</u>
22	Attenuation Rate of GaAs/n+GaAs Waveguide	64
23	Attenuation Rate of the GaAs/n+GaAs Waveguides	66
24	Contour Map of β for Graded Refractive Index Waveguide	68
25	Attenuation Rate of Graded Index Waveguide	70
26	Attenuation Rate of GaAs/GaAsP Waveguides	72
27	Schematic Diagram of an Etched Two-Dimensional Waveguide.	76
28	Photograph (500X) of a Part of the 50u Wide Two-Dimensional Waveguide Fabricated on VR5-422	78
29	Dektak Trace Showing Profile of the 50u Wide Two-Dimensional Waveguide.	79
30	Determination of Waveguide Attenuation at 1.06um Wavelength	82
31	Modulation Efficiency of Uniform Thin Film Guided Wave Modulators	89
32	The Power per unit Bandwidth Required for Uniform Thin Film Waveguide Modulators	90
33	The Equivalent B_y and B_z Representing Propagating Modes in Two-Dimensional Waveguides	97
34	Efficiency of Two-Dimensional Waveguide Phase Modulator	100
35	The Power Per Unit Bandwidth Required for Two-Dimensional Waveguide Phase Modulators	101
36	Illustration of Amplitude Modulation in Two-Dimensional Waveguides	103
37	Amplitude Modulation Efficiency of Two-Dimensional Thin Film Guided Wave Modulators	106
38	The Power Per Unit Bandwidth Required for Two-Dimensional Waveguide Amplitude Modulators	107

LIST OF FIGURES (Cont.)

<u>FIGURE NO.</u>	<u>TITLE</u>	<u>PAGE NO.</u>
39	Illustration of the Fabrication Processes for Bragg's Modulation Electrode	110
40	Illustration of Bragg's E-0 Modulator	112
41	Microscope Picture of the Grating Electrodes	113
42	The Normalized Propagation Constant in the Tapered Thin-Film Directional	118
43	Illustration of the Tapered Velocity Coupling Experiment Between Two Glass Waveguides	120

1. INTRODUCTION

GaAs thin film has been suggested by many researchers as the most promising material to use for integrated optical (IO) circuits. Many components, such as electrooptical modulators, thin film sources, or detectors may be realized in the same material system (consisting of GaAs, GaAlAs, GaInAs, or GaAsP). This opens the possibility of monolithic fabrication on a single wafer for near infra-red applications. In the far infra-red, performance of GaAs waveguide modulators is expected to be an order of magnitude better than that of bulk modulators. Low-loss, large area GaAs thin films are essential for realizing all these integrated optical components and circuits.

The major objectives of this program are to grow a variety of large area epitaxial waveguides, to evaluate their performance as waveguides and IO devices, and to optimize their design for applications at the $10.6\ \mu\text{m}$ wavelength. Since a reduced refractive index can be obtained for the substrate by using either n^+ GaAs, GaAsP, or GaAlAs materials, investigations of the epitaxial growth of all these waveguide structures were undertaken. The results obtained in our material growth programs are discussed in Sections 2 and 3. A list of the various waveguides submitted for evaluation at Washington University is given in Appendix I.

There are no fibers that can be used effectively to transmit optical signals over kilometers of distance in the far infra-red. On the other hand, there exists a need for improvement of the performance of conventional components such as electrooptical modulators for $10.6\ \mu\text{m}$ communication

systems by two or three orders of magnitude. Thus the main objective of our device research at $10.6 \mu\text{m}$ is to utilize the guided wave technique and the superior material properties of GaAs epitaxial thin films to achieve efficient and wide band modulation and switching of CO_2 laser radiation. Considerations of device performance, in turn, have affected the directions of our material growth program (e. g. emphasizing low carrier concentrations, large area waveguides, and $\text{GaAs}/\text{GaAs}_{1-x}\text{P}_x$ waveguides). The results of our waveguide and device evaluations are discussed in Sections 4.1, 4.2, 5.1, and 5.2.

The success with epitaxial waveguides at the $10.6 \mu\text{m}$ wavelength encouraged us to fabricate and to evaluate GaAs/GaAsP waveguides for $1.06 \mu\text{m}$ applications. These results are discussed in Sections 2.1.3 and 4.3. No evaluation of any active device was made at $1.06 \mu\text{m}$. However, a limited amount of effort was brought to bear on a novel idea of fiber to film coupling and on the input and output coupling of a high index waveguide. This is discussed in Sections 5.2 and 5.3. An extension of this idea to provide efficient coupling from a fiber to a GaAs waveguide and conversely from a GaAs waveguide to a fiber has been proposed to our sponsor and to the office of Naval Research.

Major accomplishments during this contract:

(a) $\text{GaAs}/\text{n}^+\text{GaAs}$ waveguides have been successfully grown by vapor phase epitaxy using the Group V hydride feed system and HCl transport of the Gallium with minimum free carrier concentrations as low as 10^{13} cm^{-3} .

- (b) The minimum measured attenuation of thick GaAs/n⁺GaAs waveguide is below 1 db/cm. The film thickness uniformity is better than 5% over the entire wafer 5 cm in size.
- (c) GaAs/GaAs_{1-x}P_x waveguides have been successfully fabricated with maximum dimensions on the order of 7 cm.
- (d) The carrier concentration of the GaAs_{1-x}P_x layer can be as low as $5 \times 10^{14} \text{ cm}^{-3}$. Its surface alloy composition variation is less than 1%. The carrier concentration of the GaAs layer on top of the GaAs_{1-x}P_x layer is in the range of 10^{13} cm^{-3} .
- (e) A single mode GaAs/GaAs_{1-x}P_x waveguide has an attenuation rate of 2 db/cm at $10.6 \mu\text{m}$. A two mode GaAs/GaAs_{1-x}P_x waveguide has an attenuation rate of 1.5 db/cm at $10.6 \mu\text{m}$. Very thick GaAs/GaAs_{1-x}P_x waveguides have attenuation rates less than 1 db/cm.
- (f) GaAs/Ga_{1-y}Al_yAs waveguides have been successfully fabricated with the GaAs layer grown by VPE and the Ga_{1-y}Al_yAs layer grown by LPE. A GaAs/Ga_{1-y}Al_yAs waveguide has an attenuation rate of 3 db/cm for the TE₀ mode, 5 db/cm for the TE₁ mode at $10.6 \mu\text{m}$.
- (g) High performance two dimensional (channel) waveguides have been realized. A chemically etched, $50 \mu\text{m}$ wide, two dimensional waveguide showed the same attenuation rate in its E_{1q}^y mode as in the TE₀ mode before etching.

- (h) Theoretical analysis, backed by experimental evidence, indicates that at $10.6\ \mu\text{m}$ the voltage performance of waveguide electrooptical modulation in the UHF-VHF range will be optimized by using $\text{GaAs}_{1-x}\text{P}_x/\text{GaAs}/\text{GaAs}_{1-x}\text{P}_x$ structures, with the central GaAs waveguide 5 to $6\ \mu\text{m}$ thick. Such structures will be several cm long, and back biased to create a depletion layer coincident with the waveguiding layer.
- (i) The calculated r.f. drive power requirement per unit modulation bandwidth can be as low as 100 mW/MHz if two dimensional waveguide modulators are used to modulate the CO_2 laser radiation.
- (j) Bragg deflection modulation has been experimentally demonstrated in a GaAs/n+GaAs waveguide.
- (k) GaAs/GaAs_{1-x}P_x waveguides for $1.06\ \mu\text{m}$ with 1 db/cm attenuation rates have been realized.
- (l) Grating couplers for both $10.6\ \mu\text{m}$ and the $1.06\ \mu\text{m}$ have been successfully fabricated and used. Grating mode converters have been fabricated and evaluated for the $10.6\ \mu\text{m}$ wavelength.
- (m) Tapered velocity coupling between two glass waveguides has been realized at $0.6328\ \mu\text{m}$ with a maximum efficiency of 100% and a reproducible coupling efficiency of 85%.

A list of the published work, input by this contract, is given in Appendix II.

2. VAPOR PHASE EPITAXY (VPE)

The objectives of the Vapor Phase Epitaxy (VPE) portion of this program were to grow various n/n^+ GaAs, GaAs/GaAs_{1-x}P_x, and GaAs_{1-x}P_x/GaAs/GaAs_{1-x}P_x structures to determine the effect of various parameters including film thickness, carrier concentration and alloy composition on waveguide and device properties at 10.6 μ m. Achievement of these objectives in terms of the requisite low carrier concentration, thickness uniformity and surface quality necessitated considerable investigation and refinement of the standard VPE techniques. The success of the GaAs/GaAs_{1-x}P_x waveguides at 10.6 μ m wavelength encouraged us in 1974 to fabricate a very thin film of GaAs on the standard layer of GaAs_{1-x}P_x for waveguiding at 1.06 μ m. In addition some work was also done on the VPE growth of GaAs films on Ga_{1-y}Al_yAs surfaces produced by a Liquid Phase Epitaxial (LPE) Technique (Section 3).

Since the GaAs/ n^+ GaAs waveguide was shown in the earlier phase of this program to be less desirable than either the GaAs/GaAs_{1-x}P_x or GaAs/Ga_{1-y}Al_yAs waveguides for electrooptical modulation, and since the materials technology for producing large area, defect free waveguides seems more advanced for the GaAs/GaAs_{1-x}P_x system than for the GaAs/Ga_{1-y}Al_yAs system, most of our work was concentrated on GaAs/GaAs_{1-x}P_x structures. Emphasis has been placed on the growth of large area waveguide structures because, as shown in Section 5.1, efficient electrooptical modulation can only be obtained in modulators 3 or 4 cm long.

2.1 VPE Growth in Production Scale Reactors

2.1.1 GaAs/n⁺GaAs Waveguides

The GaAs/n⁺GaAs waveguide structure consists of an undoped GaAs film grown on a silicon doped ($n^+ \approx 1 - 4 \times 10^{18} \text{cm}^{-3}$) GaAs substrate oriented 2° off the $\langle 100 \rangle$. The misorientation is necessary to produce planar surfaces by VPE. The wafer, limited by the size of the available GaAs slices, has maximum dimensions of $\approx 7 \text{ cm} \times 5 \text{ cm}$. A typical sample is shown in Figure 1. The reflection of the camera can be seen on the surface of the wafer.

Undoped GaAs films were grown using arsine and HCl transport of gallium in the vertical flow, laminar type reactor⁽¹⁻⁴⁾ shown schematically in Figure 2. Details of the construction of the reactor, except for two minor modifications and some dimensional changes are given in Reference 1. The bottom section of the reactor incorporating the mixing and deposition zones was enlarged to 10 cm I.D. to accommodate crystals up to 9 cm in length. The quartz joint on top of the reactor was eliminated and the bottom was converted to a flange type vacuum O-ring seal to facilitate loading and unloading the reactor.

A rotating flat disk (9.5 cm dia.) substrate holder was used to maximize thickness uniformity and homogeneity of the epitaxial films. Evaluation of the substrate holder was initially made with two substrates (approximately 2.5 cm in length) in each run placed at different radial positions on the disk. After deposition the wafers were cleaved along the major dimension, stained and the film thickness measured microscopically.



Figure 1: A typical wafer size. This sample has an area of 7 cm x 5 cm.
The reflection of the camera is also shown on the wafer surface.

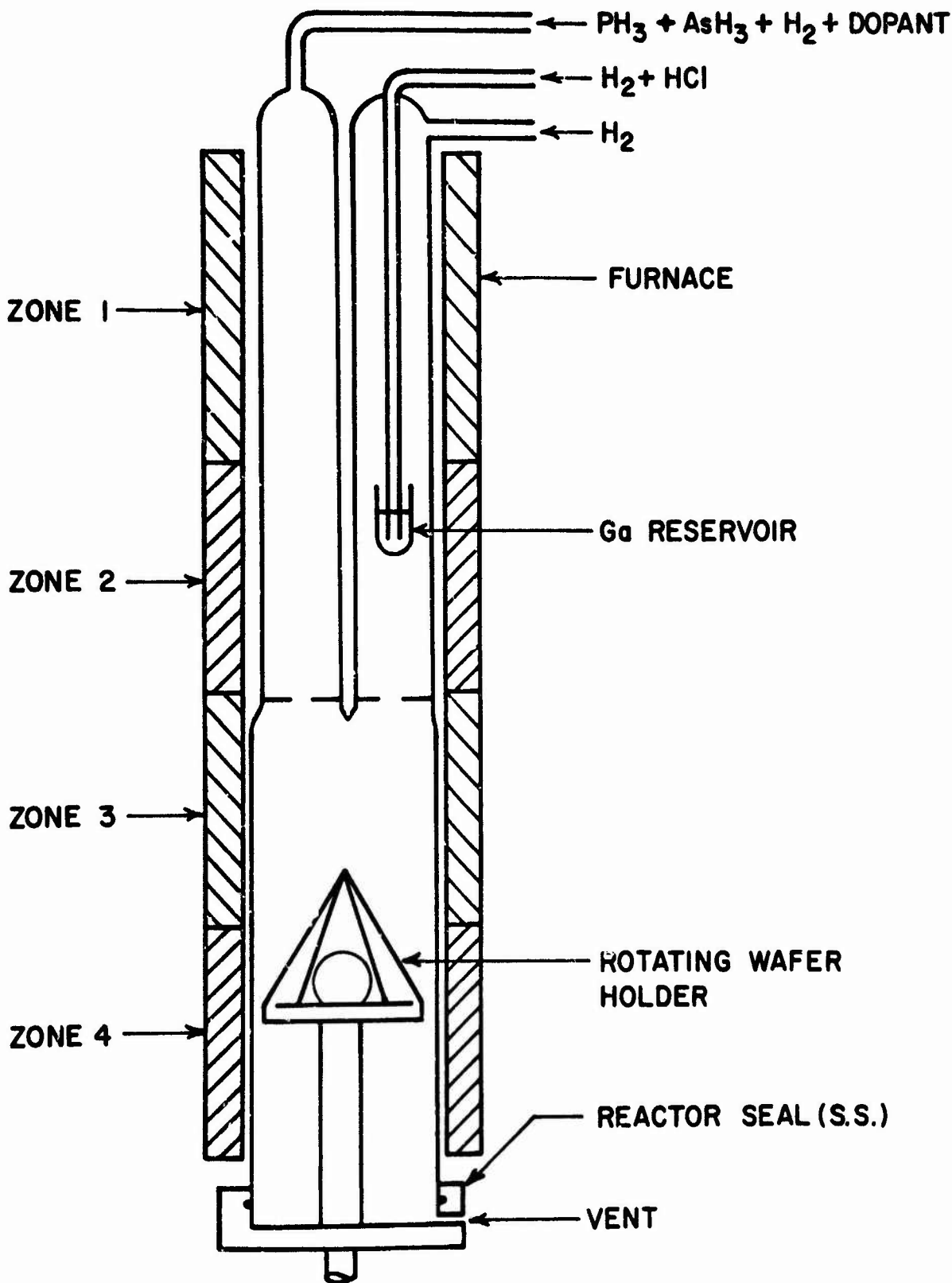


Figure 2: Schematic diagram of production scale vertical epitaxial reactor.

The results of the measurements on two different runs are given in Table 1. The variation in film thickness, not counting edge crown effects or off-orientation flats, did not exceed $\pm 5\%$ within or between wafers. These results were subsequently checked with larger wafers.

In the earlier phase of this program, control of the background carrier concentration, which ranged from 10^{15} to over $10^{16}/\text{cm}^3$ (Table 2), proved to be a major problem. The major background impurity was identified as silicon by emission spectroscopic analysis. The analysis of an undoped film approximately $90\ \mu\text{m}$ thick, Table 3, shows the silicon concentration to be an order of magnitude higher than the net carrier concentration. The production of silicon contamination in the reactor is believed to result from reactions of hydrogen and/or HCl with the quartz reactor.

Although some improvement in background carrier concentration was demonstrated by such measures as precoating the reactor with a GaAs deposit (Table 4), injecting water vapor (Table 5), or injecting ammonia (Table 6) to suppress formation of the volatile silicon species, these techniques all introduced serious drawbacks. Attempts to modify the reactor design to reduce the background doping level were generally unsuccessful although later in the program an order of magnitude improvement was observed for $\text{GaAs}_{1-x}\text{P}_x$ alloys grown using a modified reactor of proprietary design.

The most significant parameters affecting background carrier concentrations have been found to be reactant gas concentrations and

TABLE I
Epitaxial GaAs Film Thickness Uniformity
Using a Rotating Disk Holder

Run 5-102		Run 5-134	
<u>Distance</u> <u>mm</u>	<u>Film Thickness</u> <u>μm</u>	<u>Distance</u> <u>mm</u>	<u>Film Thickness</u> <u>μm</u>
0	34.2	0	49.0
5	29.4	5	45.1
10	29.4	10	46.6
15	29.4	15	46.6
20	29.4	20	42.7
25	31.9	22	44.1
28	33.8		

TABLE 2

Background Silicon Contamination Level at Original Operating Conditions

<u>Run No.</u>	<u>Deposition Temp, C</u>	<u>Net Carriers n, cm⁻³</u>	<u>Mobility @ 300K cm²/volt-sec.</u>	<u>Film Thickness, μm</u>
5-206	748	1.7 x 10 ¹⁶	6230	28
5-208	746	2.1 x 10 ¹⁶	5230	28
5-209	743	2.2 x 10 ¹⁶	5190	29
5-211	749	1.8 x 10 ¹⁶	5130	30

TABLE 3
Emission Spectroscopic Analysis of Undoped Epi GaAs

Run No. 5-20i

<u>Element</u>	<u>Atoms/cm³</u>
Al	9×10^{15}
Cr	N. D.
Ge	N. D.
Fe	3×10^{15} (EST.)
Pb	N. D.
Mn	N. D.
Mo	N. D.
Pt	N. D.
Si	1.0×10^{17}
Sn	N. D.
V	N. D.
Zn	N. D.
Sb	N. D.
Ni	N. D.
In	N. D.
Cu	9.0×10^{13}
Mg	3.0×10^{15}
Ti	N. D.
Ag	N. D.

N. D. --- Not Detected

EST. --- Estimated

Measured Net Electrical Carriers = $1.0 \times 10^{16}/\text{cm}^3$

TABLE 4

Effect of Predeposit on the Background Contamination Level

<u>Run No.</u>	<u>Deposition Temp, C</u>	<u>Net Carriers n, cm⁻³</u>	<u>Mobility @ 300K cm²/volt-sec</u>	<u>Film Thickness, μm</u>
5-212	747	2.3 x 10 ¹⁵	7510	29
5-213	752	2.9 x 10 ¹⁵	7040	23
5-220	749	3.0 x 10 ¹⁵	7150	26
5-228	744	2.2 x 10 ¹⁵	7180	25
5-229	763	2.6 x 10 ¹⁵	6610	25

Reactor coated for 30-60 min. before deposition.

TABLE 5

Effect of Water Addition on the Background Contamination Level

<u>Run No.</u>	<u>Deposition Temp, C</u>	<u>H₂O Feed Point</u>	<u>H₂O/H₂ Feed, sccm</u>	<u>Overall H₂O Conc. in Reactor</u>	<u>Net Carriers n, cm⁻³</u>
5-233	755	Flush H ₂ Group III Side	400	30 ppm	1.0 x 10 ¹⁶
5-234	762	Main H ₂ Group V Side	800	60 ppm	8.4 x 10 ¹⁵
5-236	755	H ₂ /HCl Feed to Ga	50	3.8	6.4 x 10 ¹⁵
5-237	759	H ₂ /GCl Feed to Ga	50	3.8	5.8 x 10 ¹⁵

300 ppm H₂O/H₂ mixture.

TABLE 6

Effect of the Addition of NH₃ on the BackgroundSilicon Level in Undoped GaAs

<u>Run No.</u>	<u>Deposition Temp, C</u>	<u>NH₃ Feed Conc. Mole %</u>	<u>Net Carriers n, cm⁻³</u>	<u>Mobility @ 300K cm²/volt sec.</u>
5-241	762	8.5	1.7 x 10 ¹⁵	5540
5-244	763	5.0	3.2 x 10 ¹⁵	5180
5-245	761	2.5	2.7 x 10 ¹⁵	5220

Film Thickness = 25-30 μm

deposition temperatures. Under the optimum growth conditions for minimizing carrier concentrations, production of smooth, blemish free surfaces becomes more difficult but can be achieved by careful substrate selection and preparation. The background carrier concentrations obtained, representing a 50 fold reduction, are shown in Table 7. The high liquid nitrogen temperature mobility of sample 5-287 attests to the purity of the material. Typically, at growth temperature of 750°C, the carrier concentration is in the low 10^{14}cm^{-3} range. Figure 3 depicts a typical carrier concentration profile for a GaAs/n⁺GaAs sample determined by a capacitance-voltage (C-V) measurement. This particular sample is 17.4 μm thick and the GaAs substrate is doped with silicon at a concentration of $2 \times 10^{18}\text{cm}^{-3}$. The carrier concentration is relatively constant throughout the film except for a region less than 2 μm thick adjacent to the epitaxial layer-substrate interface. The higher doping in this region is believed to be auto-doping from the substrate. Since the refractive index is related to the carrier concentration and becomes relatively constant for carrier concentrations below 10^{16}cm^{-3} , we consider the epitaxial film to have a uniform refractive index throughout its cross section.

2.1.2 GaAs/GaAs_{1-x}P_x Waveguides at 10.6 μm Wavelength

The GaAs/GaAs_{1-x}P_x heterostructures as optical waveguides provide the advantage that the substrate carrier concentration can be made arbitrarily low while the waveguiding effect is achieved because of the lower refractive index of GaAs_{1-x}P_x ($\Delta n \approx -0.4x$). The structure is shown in Figure 4. Typically the GaAs_{1-x}P_x graded region and uniform alloy region were each grown ~ 40 μm thick and the uniform alloy composition

TABLE 7
Undoped Epitaxial GaAs Grown
at Modified Growth Conditions

<u>Run No.</u>	<u>Deposition Temp, C</u>	<u>Net Carriers n, cm⁻³</u>	<u>Mobility @ 300K μ, cm²/volt-sec</u>	<u>Film Thickness μm</u>
5-278	745	8.5 x 10 ¹⁴	7800	12.7
5-279	749	4.2 x 10 ¹⁴	7860	9.8
5-280	745	7.5 x 10 ¹⁴	7600	21.5
5-287	730	1.4 x 10 ¹⁴	8340	8.8
		1.59x10 ¹⁴	92330 @ 77K	
5-289	736	3.0 x 10 ¹⁴	8110	13.8
5-415	753	4.3 x 10 ¹⁴	5837	5.5
5-416	752	1.1 x 10 ¹³	7097	5.7
5-417	740	1.3 x 10 ¹⁵	4531	6.0
5-421	754-744	2.9 x 10 ¹⁴	7717	21.1
5-422	749	3.5 x 10 ¹⁴	7490	25.4
5-423	744	6.9 x 10 ¹⁴	6079	23.7
5-424	744	No readings	--	21.5
5-427	745	3.1 x 10 ¹⁴ (C-V)	--	5.5
		1.4 x 10 ¹⁴ (C _{0.5})*		
5-428	758	5.6 x 10 ¹⁴ (C-V)	--	4.9
		4.8 x 10 ¹⁴ (C _{0.83})*		

* Calculated from capacitance measurement at indicated forward bias.

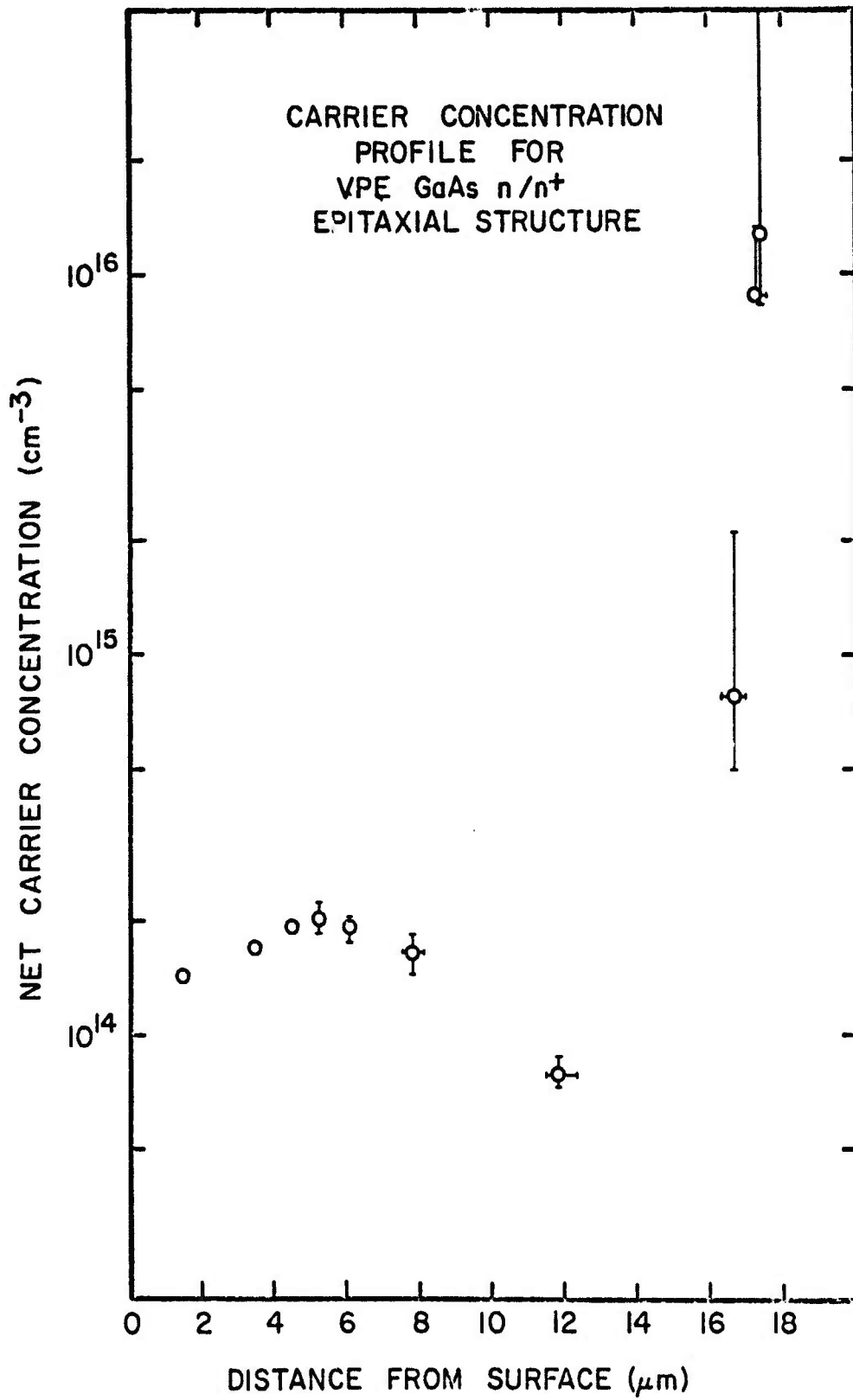


Figure 3

AIR

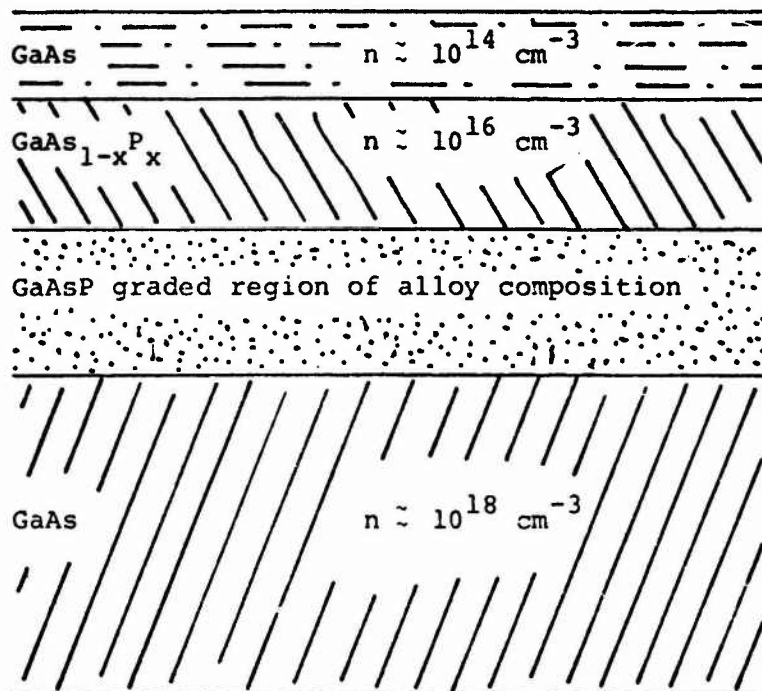


Figure 4: Schematic of the GaAs/GaAs_{1-x}P_x Waveguide Structure.

was $\sim 35\%$ GaP ($x = 0.35$). The composition change in the graded region is approximately linear. The background free carrier concentration of $\sim 10^{16}\text{cm}^{-3}$ in the alloy was reduced into the 10^{15} and 10^{14}cm^{-3} range later in the contract period while the GaAs film in many samples had carrier concentrations in the 10^{13}cm^{-3} range.

The $\text{GaAs}_{1-x}\text{P}_x$ layers were VPE grown in the reactor illustrated in Figure 2 and described in the previous section, and the GaAs was subsequently grown on top to form a waveguide. In growing $\text{GaAs}_{1-x}\text{P}_x$ on GaAs substrates, the graded region appears to be necessary to accommodate the lattice mismatch between GaAs and the $\text{GaAs}_{1-x}\text{P}_x$ layer and minimize structural defects, particularly stacking faults, in the latter. (2) Surprisingly, however, GaAs layers of excellent appearance can be grown directly on a $\text{GaAs}_{1-x}\text{P}_x$ surface without an intermediate graded region.

Success in growing GaAs films on the $\text{GaAs}_{1-x}\text{P}_x$ surface was found to depend critically on surface preparation. The alloy surface must be clean but not etched. Either acid or vapor etching of the $\text{GaAs}_{1-x}\text{P}_x$ surface appears to produce surface irregularities or inhomogeneities that cause nonuniform growth of the GaAs layer. Thus the layer will appear hazy or show an enhancement of the cross-hatch pattern normally present on the alloy surface.

$\text{GaAs}/\text{GaAs}_{1-x}\text{P}_x$ structures of good surface quality were grown in either single, continuous runs, or in two separate runs. In the former case, growth was actually discontinued for a period while furnace temperatures were reduced from those required to grow good quality $\text{GaAs}_{1-x}\text{P}_x$ to

those necessary for low carriers in the GaAs layer. While this procedure would appear to eliminate the necessity for cleaning the $\text{GaAs}_{1-x}\text{P}_x$ surface prior to GaAs deposition, in many cases wafers were spoiled by debris falling onto the surface from the walls of the reactor, presumably particles of the predeposit formed during growth of the alloy loosened by the temperature change. Therefore, the second procedure was adopted for all of the later waveguide structures. Initially some GaAs films had been grown on wafers of off-specification standard red LED material with limited success.

The first $\text{GaAs}_{1-x}\text{P}_x$ layers of acceptable surface quality required a deposition temperature of $\sim 820^\circ\text{C}$ and had carrier concentrations in the range of $3 - 5 \times 10^{16} \text{ cm}^{-3}$, as shown by the data of Table 8. Improvement in substrate preparation techniques eventually permitted reduction in growth temperature to $\sim 800^\circ\text{C}$, but carrier concentrations remained in the mid to low 10^{16} cm^{-3} range as indicated by data for the first three runs listed in Table 9. Installation of a new reactor, identical to that described above in the lower, deposition end, but differing in the design of the Ga reservoir and gas input tabulation, resulted in immediate improvement in the background carrier concentration. This is evident in the data listed in Table 9 for runs 6-69 through 6-85 and again for runs 6-100 through 6-114 in which the same reactant gas sources were used in both types of reactor. With the lower silicon background level achieved in the new reactor, impurities originating in the AsH_3 and PH_3 supply sources become apparent. At least a six-fold decrease in carriers accompanied the change in PH_3 cylinders at run 6-175 and at least as large an increase

TABLE 8

Undoped GaAs_{1-x}P_x Growth

<u>Run No.</u>	<u>Deposition Temp. (C)</u>	<u>Thickness, (μm) Grade</u>	<u>Alloy</u>	<u>Net Carriers n (cm⁻³)</u>	<u>Surface Quality</u>
5-472	793	44.5	59.3	1.07 x 10 ¹⁶	Bad, pyramids, faults
5-473	806	24.7	29.6	1.4 x 10 ¹⁶	Many faults some areas
5-474	805	14.8	31.1	2.3 x 10 ¹⁶	Few pyramids, many faults
5-475	810	99	108	7.4 x 10 ¹⁵	Fairly good
5-476	817	39.5	64.2	3.5 x 10 ¹⁶	Solvent stain traces
5-477	818	59.3	54.3	4.6 x 10 ¹⁶	Debris on surface
5-478	818	24.7	34.6	5.3 x 10 ¹⁶	Very good, some debris
5-479	818	50.9	64.2	3.0 x 10 ¹⁶	Very good
5-484	819	31.2	40.0	3.5 x 10 ¹⁶	Good
				7.2 x 10 ¹⁶	CV (to depth of 0.45 μm)
5-490	816	39.5	39.5	5.1 x 10 ¹⁶	Good
5-492	816	34.6	29.6	4.9 x 10 ¹⁶	Very good, 2.39 in ²

TABLE 9

Undoped GaAs_{1-x}P_x Growth

Run No.	Deposition Temp. (C)	Thickness (μm) Grade	Alloy	Net Carriers n (cm ⁻³)	Remarks
6-51	807	--	--	4.3 x 10 ¹⁶	Old style reactor
6-58	809	24	27	3.2 x 10 ¹⁶	
6-69	798	29	29	4.5 x 10 ¹⁶	AsH ₃ changed
6-75	788	47	45	5.9 x 10 ¹⁵	New style reactor
6-81	792	37	39	1.4 x 10 ¹⁶	
6-85	798	49	51	3.3 x 10 ¹⁵	
6-100	794	--	--	4.7 x 10 ¹⁵	PH ₃ changed
6-101	798	--	--	2.8 x 10 ¹⁶	Old style reactor
6-102	785	--	--	3.5 x 10 ¹⁶	
6-103	796	--	--	1.5 x 10 ¹⁵	New style reactor
6-104	788	--	--	6.3 x 10 ¹⁵	
6-114	805	45	47	9.4 x 10 ¹⁵	
6-146	803	41	45	7.0 x 10 ¹⁵	New AsH ₃
6-148	805	--	--	1.35 x 10 ¹⁶	New AsH ₃
6-159	803	47	44	2.5 x 10 ¹⁶	New PH ₃
6-166	810	37	41	3.9 x 10 ¹⁶	New AsH ₃
6-169	808	43	41	4.0 x 10 ¹⁶	
6-176	808	42	29	4.4 x 10 ¹⁵	New PH ₃
6-178	804	44	35	7.9 x 10 ¹⁵	
6-202	796	--	--	3.8 x 10 ¹⁵	New operation condition New AsH ₃ and PH ₃
6-210	796	42	35	1.73 x 10 ¹⁵	
6-219	796	39	44	1.27 x 10 ¹⁵	
6-221	799	44	44	2.24 x 10 ¹⁴	New AsH ₃ and PH ₃
6-234	798	43	43	2.04 x 10 ¹⁴	New AsH ₃
6-238	805	42	49	5.30 x 10 ¹⁴	
6-244	800	42	68	1.47 x 10 ¹⁵	New AsH ₃
6-246	798	44	79	1.10 x 10 ¹⁵	
6-251	798	74	44	2.39 x 10 ¹⁵	

on changing AsH_3 cylinders at run 6-244. The change in mode of operation of the new reactor, noted at run 6-202, may also have contributed to the subsequent low carrier concentration by further reducing the silicon background.

The carrier concentrations listed in Tables 8 and 9 were obtained by Hall measurements of the composite layers grown on high resistivity substrates included in each run. The effect of the relatively high mobility, initial graded region on these measurements is to reduce the apparent carrier concentration by about a factor of two below the true value as determined by the C-V method. This effect is shown by the data for run 5-484, listed in Table 8.

The uniformity of the phosphorus content in the $\text{GaAs}_{1-x}\text{P}_x$ alloy layer was checked by measuring the wavelength of the 77K photoluminescent (PL) emission at five points of a 4cm x 4cm wafer. The results, expressed as mole % GaP, are illustrated in Figure 5. It is readily seen that the surface alloy uniformity is excellent with a variation of less than 1%. Hence we are assured of a uniform $\text{GaAs}_{1-x}\text{P}_x$ substrate with a refractive index constant over the whole wafer.

The net electrical carrier concentration in the GaAs film grown on $\text{GaAs}_{1-x}\text{P}_x$ substrate layers was determined mainly by the C-V technique. Hall measurements of $\sim 5 \mu\text{m}$ layers grown on companion high resistivity substrates proved to be unreliable. In many cases p-type readings were obtained, traceable to copper contamination of the semi-insulating chromium doped GaAs substrate. Spectroscopic analysis of

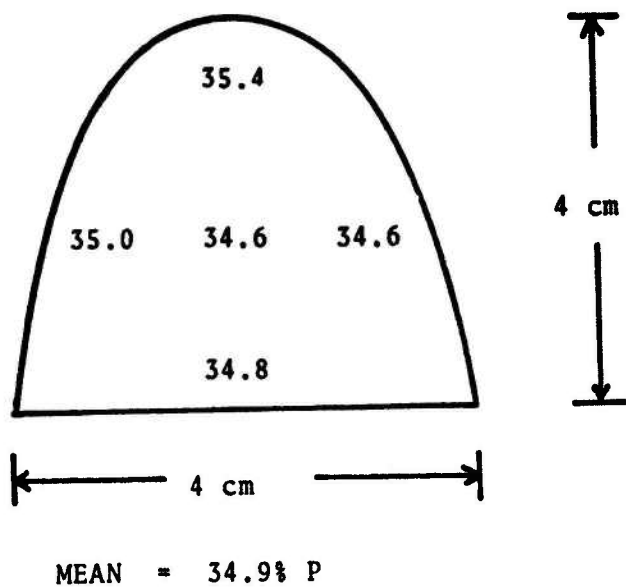


Figure 5. Surface alloy composition of $\text{GaAs}_{1-x}\text{P}_x$ Wafer.

samples from two different lots of Cr doped GaAs showed Cu concentrations of 1.7×10^{16} a/cm³ and 4.9×10^{14} a/cm³, respectively. Rapid diffusion of Cu from the substrate into the epi layer of the Hall sample at growth temperatures of 750C could easily convert a thin layer to p-type while not affecting the n-type growth on other substrates in the run. Thicker layers or more heavily doped n-type layers, as in the case of the GaAs_{1-x}P_x layers, would be less affected. In addition to the possibility of this type of contamination, is the difficulty of making low resistance ohmic contacts to low carrier material. Reliable contacts to material of much less than 10^{14} carrier/cm³ have not been demonstrated.

A comparison of results using both the C-V measurement and Hall measurement is shown in the data of Table 10 for GaAs film grown on LED GaAs_{1-x}P_x material. C-V measurements lose some of their utility for thin layers of low carrier material because of the dependence on carrier concentration of the zero-bias depletion depth in a Schottky barrier junction. At 5×10^{13} carriers/cm³ in GaAs this is already about 5 μm, the thickness of the active layer. In practise, excessive leakage has prevented accurate C-V measurements under forward bias to obtain data at depths much less than the zero-bias depth. Thus, only an estimate of an upper limit to the carrier concentration can be obtained from the zero-bias capacitance. This is the interpretation that should be placed on the carrier concentration data for the thin GaAs films listed in Appendix 1.

The earlier, large area GaAs/GaAs_{1-x}P_x structures, although appearing flat to the eye, were so severely bowed as to prevent both

TABLE 10

Undoped Epitaxial GaAs Grown on LED GaAs_{1-x}P_x Material

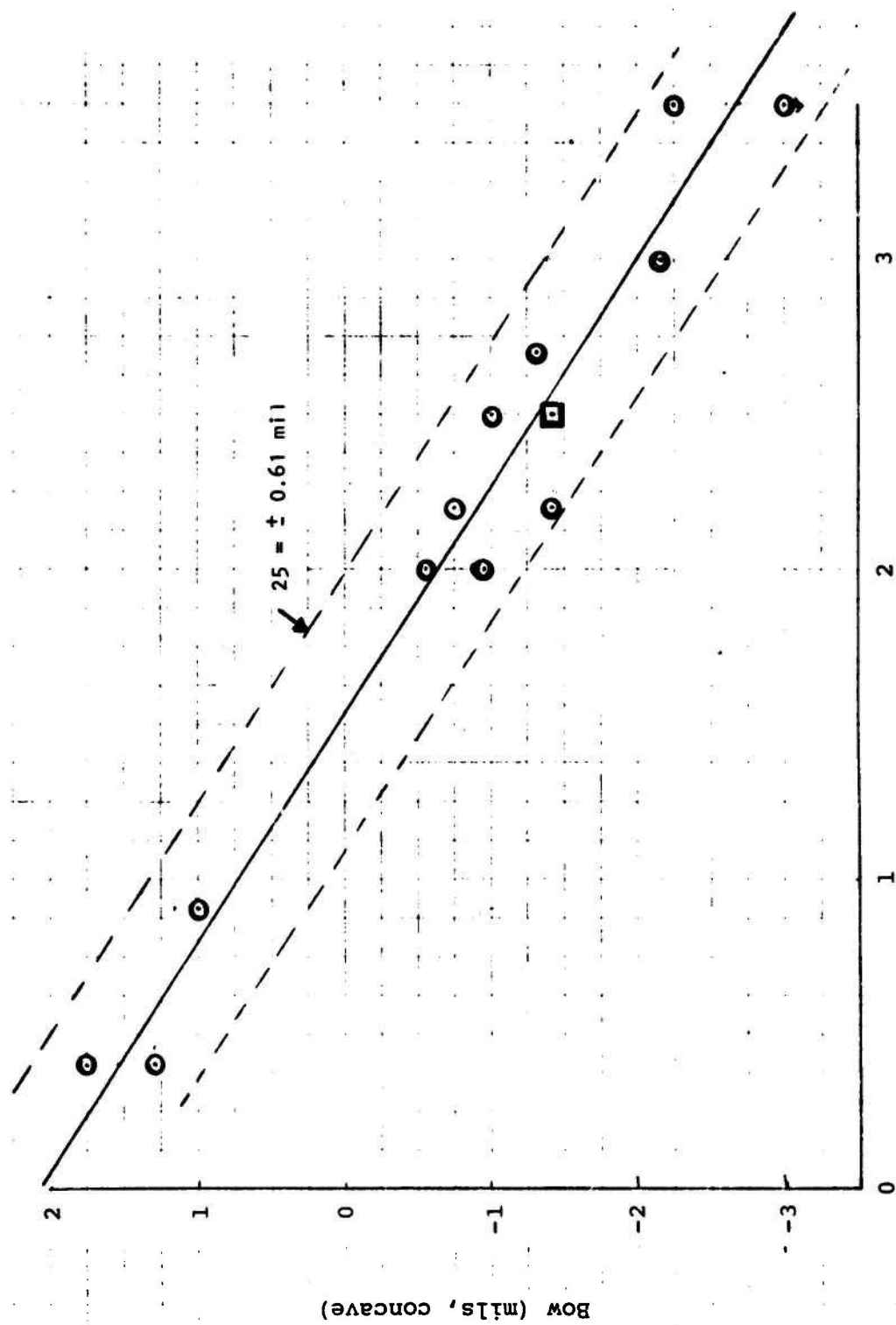
<u>Run No.</u>	<u>Deposition Temp. °C</u>	<u>Net Carriers n, cm⁻³</u>	<u>Mobility, μ cm²/volt-sec</u>	<u>Epi Film Thick, μm</u>	<u>Surface Appearance</u>
453	786	7.6×10^{15}	5590	18	Hazy
456	788-741	2×10^{15}	5340	5.9	
457	757	No readings		6.2	
458	757	3.4×10^{14}	3680	5.8	Good
		4.2×10^{14} (CV)			
459	760	4.2×10^{14} (p)	188	2.5	Hazy
460	748	No stable readings		--	Good
		2.4×10^{14} (CV)		13.9	
		4.4×10^{14} (C ₀)			
461	746	8.1×10^{14}	5520	4.7	Good
462	748	8.6×10^{13}	1306	4.9	Good
		6.6×10^{13} (C ₀)		4.9	
463	744	5×10^{15}	4040	--	Good
		6.8×10^{13} (C ₀)		4.7	
464	748	5.0×10^{14}	5103	6.2	Good, scattered specks
		4.9×10^{13} (C ₀)		6.5	
465	747	5.3×10^{13}	2189	7.8	Fairly good, some faults
		4.5×10^{13} (C ₀)		6.0	
466	736	7.8×10^{13}	3779	7.8	Rows of faults
		3.4×10^{13} (C ₀)		7.1	

TABLE 10 (Continued)

<u>Run No.</u>	<u>Deposition Temp °C</u>	<u>Net Carriers n, cm⁻³</u>	<u>Mobility, μ cm²/volt-sec</u>	<u>Epi Film Thick. μm</u>	<u>Surface Appearance</u>
467	737	1.5×10^{13}	8801	~ 7	Poor, many faults
468	748	No readings		---	Poor, many faults
		$6.4 \times 10^{13}(C_0)$		5.2	
469	749	$5 \times 10^{14}(p)$	137	5.9	Rows of faults
470	758	$7.3 \times 10^{14}(p)$	203	5.9	Rows of faults
471	760	No readings		---	Very bad

efficient prism coupling into the waveguides and application of photolithography techniques. The concave bowing of the wafers is thought to be due to residual strain in the alloy-grade composite not relieved by the generation of mismatch dislocations. It can be reversed by introducing an abrupt step reduction of phosphorus concentration in the vapor composition at the end of the grading period. The experimentally determined relationship between the wafer bow and the magnitude of the vapor composition change for our particular growth conditions is displayed graphically in Figure 6. The presence or thickness (in the range up to $11.7 \mu\text{m}$) of a GaAs film produced no detectable effect on the degree of bow. The scatter indicates the repeatability from run to run. Subsequent samples were grown with a step composition change of 2% to insure a surface bowed convex between 0 and 1 mil.

To determine the uniformity of the GaAs films, photoluminescence measurements were performed on ten GaAs/GaAs_{1-x}P_x samples with GaAs film thicknesses varying from $1 \mu\text{m}$ to $10 \mu\text{m}$. Only the $1 \mu\text{m}$ thick sample indicated a 10\AA shift in the photoluminescence peak. The other samples gave a constant reading. This small shift is understandable. The residual elastic stress in the thin layer due to the lattice mismatch or the difference in thermal expansion coefficient between GaAs and GaAs_{1-x}P_x might be expected to shift the band gap. A further study of photoluminescence on a step-etched sample again indicated a uniform GaAs layer as well as a uniform GaAs_{1-x}P_x layer. Measurements were taken as close as $2 \mu\text{m}$ from the GaAs/GaAs_{1-x}P_x interface. The uniformity was also confirmed



Vapor Composition Change (%)

Figure 6: Bow of 5 cm GaAs/GaAs_{1-x}P_x wafers as a function of step reduction in phosphorus composition at end of grading period during growth of the alloy.

by X-ray diffraction patterns. The GaAs/GaAs_{1-x}P_x waveguide is formed by an abrupt change from GaAsP to GaAs so the lattice mismatch produces a large number of dislocations at and near the interface. Although our photoluminescence measurements reveal uniformity in both GaAs and GaAsP layers, the high dislocation density near the interface might be expected to interfere with the waveguiding effects, especially at 1.06 μm.

2.1.3 GaAs/GaAs_{1-x}P_x Waveguides at 1.06 μm Wavelength

The structures grown for this investigation are identical to those described in the previous section except for the reduced thickness of the GaAs film. Achievement of good surfaces in such thin layers of GaAs grown directly on GaAs_{1-x}P_x did present a special problem as evidenced by the following observation. Under growth conditions that yielded good, shiny 2 μm thick layers, 1 μm thick layers appeared hazy. This is interpreted as being due to a very slight roughening of the alloy surface by etching or decomposition prior to deposition of the GaAs film which could not be completely covered by a 1 μm thick film. Of course, such a rough interface would be expected to be detrimental in guiding 1.06 μm waves. Ultimately several fairly good 1 μm film surfaces were produced.

Another possible detriment to 1.06 μm waveguiding is the cross hatch pattern inherent in the surface of as grown GaAs_{1-x}P_x wafers. Waveguide evaluation results (Section 4.3) indicated that the slight cross hatch pattern might be causing significant amounts of mode conversion. Figure 7(a) shows the surface profile of a typical waveguide as measured

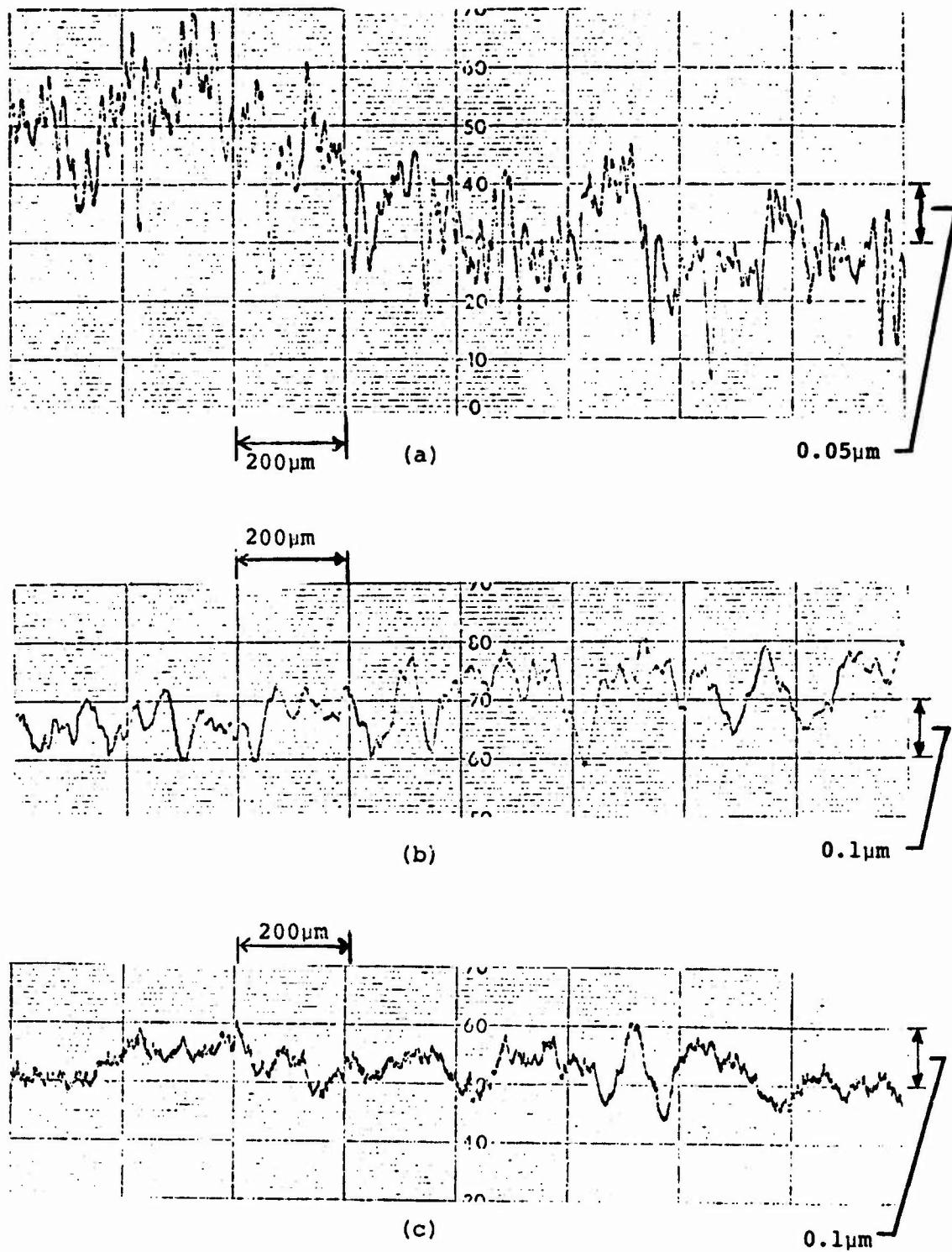


Figure 7: Surface Corrugations of $\text{GaAs}/\text{GaAs}_{1-x}\text{P}_x$ Waveguides
 (a) $x = 0.4$ (b) $x = 0.2$ (c) $\text{GaAs}_{1-z}\text{P}_z/\text{GaAs}_{1-x}\text{P}_x$,
 $z = 0.2, x = 0.4$

by the DEKTAK thickness monitor. Attempts to polish the $\text{GaAs}_{1-x}\text{P}_x$ layer before growth of the GaAs film were unsuccessful. However, some reduction in the severity of the cross hatch is obtained by reducing the alloy composition in the $\text{GaAs}_{1-x}\text{P}_x$ to $x = 0.2$. This is shown in Figure 7 (b). Figure 7 (c) shows that the cross hatch pattern is also reduced in a $\text{GaAs}_{1-z}\text{P}_z/\text{GaAs}_{1-x}\text{P}_x$ ($z = 0.21$, $x = 0.42$) waveguide. Note that the gross cross hatch pattern is reduced in (b), while both the gross and the fine cross hatch patterns are reduced in (c). The $\text{GaAs}_{1-z}\text{P}_z/\text{GaAs}_{1-x}\text{P}_x$ waveguides were fabricated for applications in the $0.9\ \mu\text{m}$ wavelength.

2.1.4 GaAs/Ga_{1-y}Al_yAs Waveguides

Exploratory runs for growing films of GaAs on GaAlAs substrates were attempted using $\langle 100 \rangle$ oriented substrates obtained from Monsanto Electronic Special Products. While layers grown simultaneously on GaAs for Hall samples were of good quality, equivalent to those listed in Tables 5, 6, and 7, very poor epi layers were grown on the GaAlAs. This was to be expected from the poor quality of the substrate surfaces and the tendency of pyramids to grow on near $\langle 100 \rangle$ surfaces. Subsequently LPE layers grown 2° off $\langle 100 \rangle$ were obtained in the LPE portion of this program. Since LPE growth on off-orientation substrates produces a step-like surface, it was necessary to lap and polish the wafers before using them in an attempt to grow planar VPE films.

The best VPE GaAs surfaces using standard growth conditions were rather dull and contained pronounced growth steps as evident in

Figures 8 and 9. This result is believed due to initial nucleation and growth of discrete islands whose edges continue to grow as steps even after overlapping. It resembles growth on a very rough or pitted surface even though the interface is flat. A more extreme case is shown in Figure 10 (b), in which prior to growth the substrates were vapor etched for two minutes in the presence of AsH_3 . This treatment evidently effectively masked the surface and delayed nucleation and growth of GaAs except along surface scratches. The size of the growth islands must be related to the time of nucleation. These effects are thought to be related to the stability of aluminum oxide and the greater tendency of GaAlAs to form a stable oxide surface.

Some improvement in nucleation was achieved by increasing the deposition temperature, but the best results were obtained by increasing both temperature and total gas flows and switching directly into the growth cycle after bringing the substrates to temperature under hydrogen flow. After a total of twenty-three runs, a fairly good GaAs layer was obtained on a large ($3/4'' \times 1''$ plus) GaAlAs substrate in the twenty-fourth run. Table 11 summarises the results.

Due to the inherent difficulty in combining VPE processing with LPE, differences in preferred growth orientation, additional handling required and critical nature of the substrate surfaces, this approach was abandoned in 1974 in favor of concentration on the GaAs/GaAs_{1-x}P_x structures. The latter is suited to and requires an all VPE process, whereas GaAs/GaAlAs structures can and are being grown in all LPE

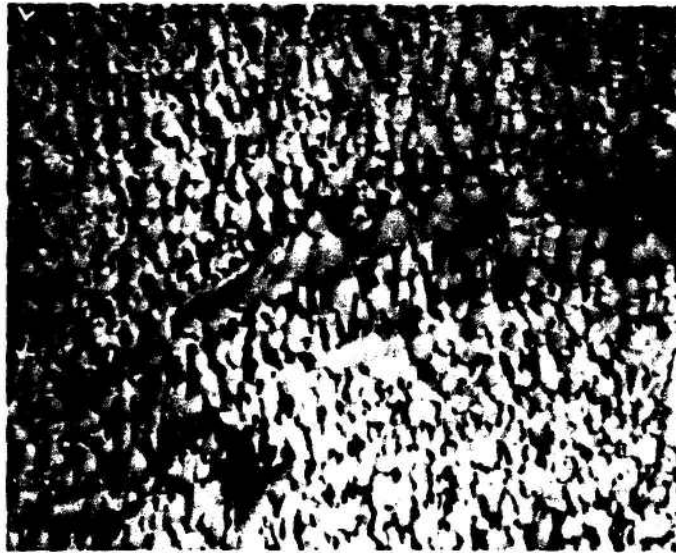


Figure 8. Surface of GaAs/GaAlAs
VR5-439/MRC 6074-1 50X

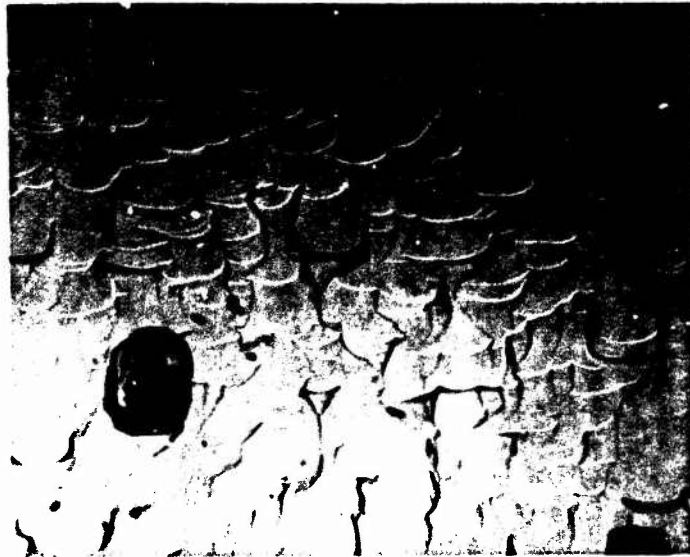
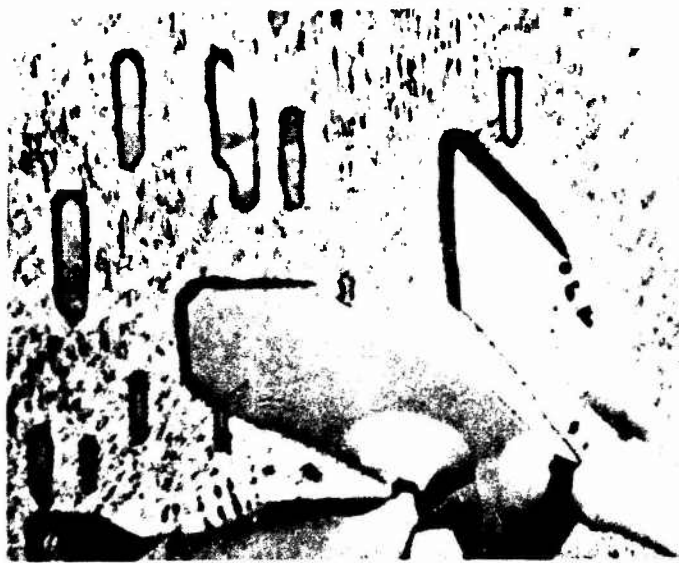
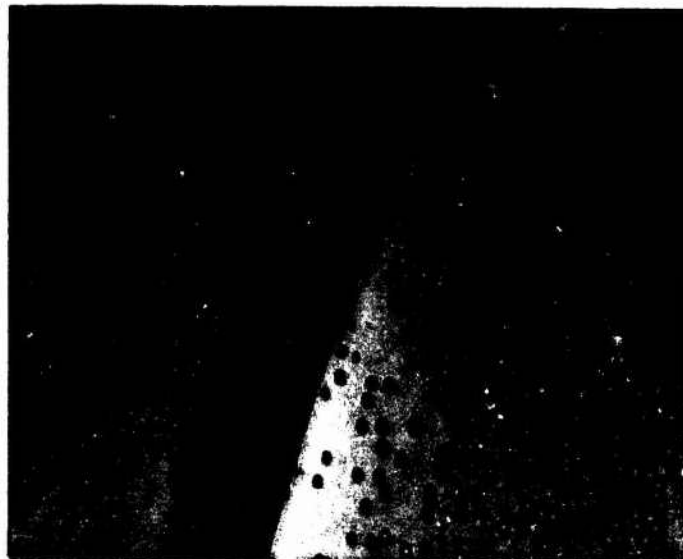


Figure 9. Surface of GaAs/GaAlAs
VR5-438/MRC 6074-1, 200X



(a)



(b)

Figure 10. Surface of GaAs/GaAlAs, VR5-440/MRC 6074-1. (a) 50X showing large plates up to $48\ \mu\text{m}$ high which nucleated immediately along apparent scratch lines and other imperfections as well as smaller plates which must have nucleated at a later stage. (b) 500X showing tiny, late nucleating poly-hedra on bare substrate beside edge of a large plate.

TABLE 11

Undoped GaAs Grown on GaAlAs

<u>Run No.</u>	<u>Deposition Temp, C</u>	<u>Net Carriers n, cm⁻³</u>	<u>Mobility, μ cm²/volt-sec</u>	<u>Film Thick, μm</u>	<u>Surface Quality</u>
433	754	1.07 x 10 ¹⁴ 2.3 x 10 ¹⁴ (C-V) 7.3 x 10 ¹³ (C _{0,5})	7500	7.8 13	Poor
434	757	7.5 x 10 ¹³ 6.0 x 10 ¹⁴ (C-V) 3.1 x 10 ¹³ (C _{0,6})	7427	6.8 4	Poor
435	756	p + n readings 2.9 x 10 ¹⁴ (C-V) 5.5 x 10 ¹³ (C ₀)		12.7 9.5	Poor
436	755	4.9 x 10 ¹⁴	5027	5.8	Poor
437	756	1.0 x 10 ¹⁵	4601	5.8	Poor
438	756	6.5 x 10 ¹² (V. un- stable)	2030	7.8	See Figure 1
439	770				See Figure 2
440	738	3.8 x 10 ¹⁴	7126	14.6	See Figures 3a and b
443	747	7.8 x 10 ¹¹ (V. unstable) 4.2 x 10 ¹⁴ (C-V) 5.4 x 10 ¹⁴ (C ₀)	2814	5.8 5.4	Poor
447	776	4.4 x 10 ¹⁵	5527	12.1	Better, but contains pits
448	784	9.1 x 10 ¹⁴	7179	13.8	Stacking faults
449	793	1.3 x 10 ¹⁵	6162	13.7	Stacking faults
450	784	6 x 10 ¹⁴	6825	15.6	Very good - few pits
451	798	1.1 x 10 ¹⁴	5893	13.8	Good, few faults and pits
452	790	1.9 x 10 ¹⁵	5980	7.8	Fairly good, Large Area

Runs 448 through 452 at twice normal flow rate
Hall and C-V measurements on GaAs substrates

systems elsewhere. Furthermore, as mentioned earlier, the attenuation results obtained in this program using $\text{GaAs}_{1-x}\text{P}_x$ structures were at least equivalent to any obtained using GaAlAs structures so there was no strong incentive to try to cope with the difficulties presented by the large area LPE growth of GaAlAs.

2.2 Growth of High Resistivity GaAs in Research Scale Reactors

To reduce r.f. power dissipation in GaAs waveguides for electrooptical modulation applications, high resistivity epitaxial layers would be required. In order to achieve layers with the desired $> 10^6$ Ω -cm resistivity it will be necessary to develop a technique for compensating the epitaxial layers.

Techniques for producing high resistivity VPE GaAs layers were explored using laboratory scale horizontal reactors in order to minimize developmental costs. The results of these experiments will be summarized here although none of the approaches achieved reproducible growth of compensated high resistivity GaAs films. Two avenues were explored, compensated deep donor (Zn-O) doping, and deep acceptor (Cr or Fe) doping.

An apparently successful initial attempt at Zn-O doping, reported in the January 1973 Semi-Annual report, now appears due to an i-layer formed during the transition from Zn-O doping, probably p-type, to Te doping of the n-type surface contact layer. The major difficulties in growing individual high resistivity layers of Zn-O doped GaAs appear to be low O concentrations in spite of water vapor concentrations in the reactant gas as high as 0.67% combined with strong dependence of Zn

concentration on deposition temperature and poor control of the Zn dopant concentration at the very low flows required. As a result, the grown layers were of low resistivity, either n- or p-type, and occasionally both were produced simultaneously.

Control of zinc doping is complicated by zinc contamination of the system which can carry over to a subsequent run and by preconditioning of the system required before low zinc doping levels can be achieved. Both effects are probably due to decomposition and/or adsorption of diethyl zinc in the line entering the reactor.

GaAs layers doped with Zn-O, but remaining n-type, have shown lowering of mobilities at both 300K and 77K and from 25% to 50% freeze out of carriers between 300K and 77K. However, the data show poor correlation with zinc and oxygen doping concentration.

Doping with Cr to produce high resistivity VPE layers did not prove successful. It may be concluded that Cr is either not transported or not incorporated in sufficient concentration to affect the electrical properties. In addition, impurities in the Cr source can interfere with the desired electrical properties.

With the chromium source located in a small boat in the hottest zone of the furnace upstream of the substrates, one sample of Cr metal (Ventron) yielded conductive p-type layers, another (Atomergics) yielded compensated n-type layers. CrCl_2 produced high resistivity layers, but of poor surface quality due to etching by the HCl produced by reacting with H_2 . An undoped run, after removal of the Ventron Cr from the system, also produced p-type layers, presumably due to Cu

contamination. Emission spectroscopic analysis showed the Ventron Cr to contain 3-5 times more Cu than the Atomergics sample.

Both Cr metal (Atomergics) and CrCl_2 , prerduced, when used in a reactor in which the source was located in the GaCl-H_2 stream out of contact with arsenic or deposited GaAs, yielded compensated n-type layers. However, on removal of the CrCl_2 source, subsequent runs produced $\sim 5 \times 10^{13}$ p-type material. Evidently the CrCl_2 introduces an n-type impurity as well as Cu which persists as a low level contaminant in the system.

Attempts to produce high resistivity VPE GaAs by iron doping were also unsuccessful, again due to probable copper contamination. The carriers in four successive runs using the same source (Ventron iron wire) changed progressively from 6.4×10^{15} n-type to 1.5×10^{14} p-type. Better control of iron volatilization (Fe reacted with GaCl to form a Ga-Fe alloy) and a higher purity source are indicated. However, since previous reports⁽⁵⁾ of Fe doping in GaAs have indicated maximum resistivities of only $< 10^5$ ohm-cm for both VPE and bulk GaAs, these efforts were discontinued.

The apparent ease with which relatively uncompensated material of either p-type or n-type can be produced suggests a very low concentration of deep level impurities in these epitaxial layers. If a low concentration p-type background can be established, low level doping with oxygen may be the best route to high resistivity GaAs.

These difficulties encountered in the growth of very high resistivity GaAs films led us to consider the use of a reverse biased p-n junction

coincident with the heterojunction to limit the r. f. dissipation. This point will be discussed again in Section 6. 1.

3. LIQUID PHASE EPITAXIAL GROWTH OF GaAlAs

The primary objective of the Liquid Phase Epitaxy (LPE) portion of the program is to grow $\text{Ga}_{1-y}\text{Al}_y\text{As}$ layers on GaAs substrates. The VPE process is then used to grow the GaAs layer on the $\text{Ga}_{1-y}\text{Al}_y\text{As}$ LPE layer to form the waveguide for propagation at the $10.6\ \mu\text{m}$ wavelength. This structure has a much smaller lattice mismatch at the GaAs-alloy interface than that in the GaAs/ $\text{GaAs}_{1-x}\text{P}_x$ system previously described. The goal is to ascertain whether the GaAlAs system offers a significant improvement in waveguide performance at the $10.6\ \mu\text{m}$ wavelength over what can be obtained in GaAs/n⁺GaAs and in GaAs/ $\text{GaAs}_{1-x}\text{P}_x$ waveguides.

Initially, a 6 inch POCO graphite sliding boat, shown in Figure 11, was used with a Model 5313 Closed-Loop Radiant Heating System made by Research Inc., Minneapolis, Minn. In this system the boat and melt are stationary while the substrate slides under the melt. The top and bottom halves of the boat are held together with graphite pins. The boat will accommodate a $3/4 \times 1-1/4$ inch substrate. The furnace is a parabolic clamshell with twelve tungsten infrared heat lamps which provide a ten inch heated length.

The early runs produced layers with a carrier concentration in the $10^{17}\ \text{cm}^{-3}$ range, while the surface quality and layer thickness uniformity were unsatisfactory. Cooling rates in the range of 0.5 to $6.5^\circ\text{C}/\text{min}$ were investigated, the slower growth rates appearing to produce slightly improved surface quality. Starting-growth temperatures were generally near 775°C , but trial runs up to 930°C were made

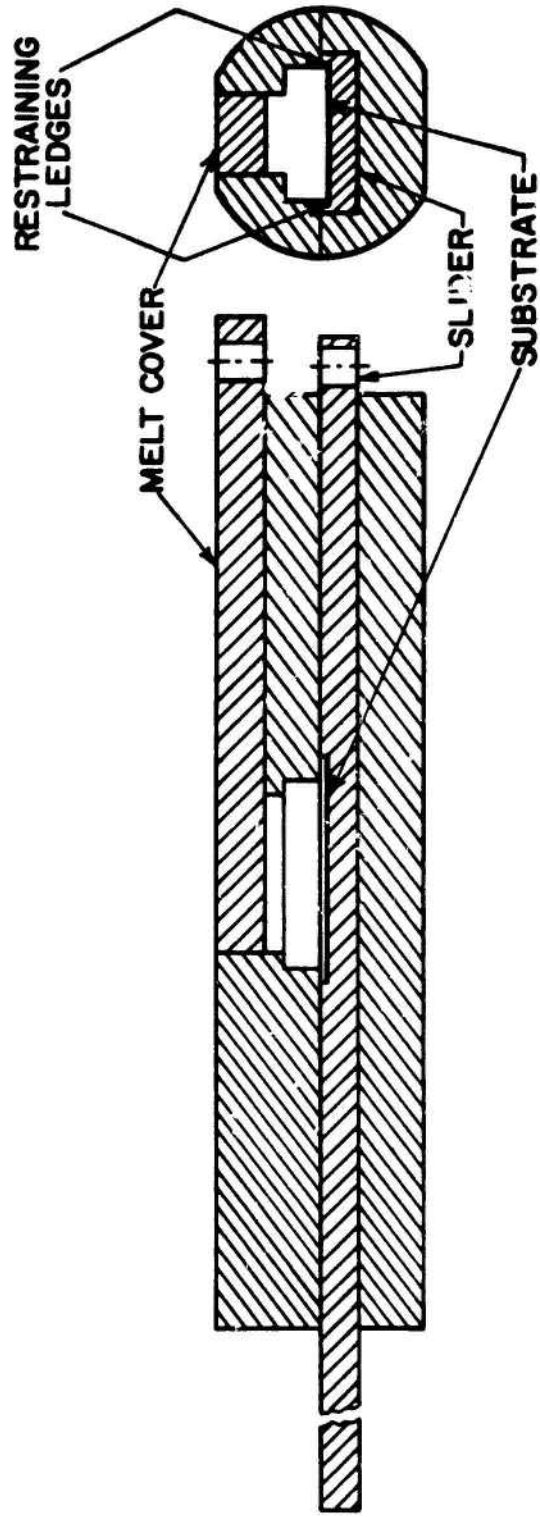


Figure 11: Research Scale LPE Graphite Boat

without significant changes in surface quality or layer thickness uniformity. Although layers with a thickness variation of only 10% were often observed over the central area of the wafer, severe edge effects were always present. It was concluded that the relatively small mass of the six inch boat plus the short temperature zone of the radiant furnace precludes the growth of large area uniform epi layers.

A large-area graphite slider-boat, 12 inch long, was then designed and constructed for $3/4 \times 2$ inch substrates. A schematic drawing of the boat is shown in Figure 12. This system utilizes a Lancer Diffusion Furnace (Lindbergh Hevi-duty) with a $4-3/4$ inch bore and a 53mm I. D. quartz reactor tube. The furnace has a 20 inch flat ($\pm 0.5C$) temperature zone and can be programmed to cool at a rate from $0.1^{\circ}C/min$ up to the no-current cooling rate of the furnace ($5^{\circ}C/min$ at $800^{\circ}C$).

The Radiant Heat Furnace shown in Figure 13 was then used to saturate a melt of Ga plus Al with AsH_3 to form GaAlAs. The gas phase saturation usually produces a product with a lower background impurity level than does the addition of undoped GaAs. The gas phase saturation also makes it possible to resaturate a used melt up to the starting growth temperature. The graphite melt saturation boat is shown in Figure 14. The 12 inch graphite sliding-boat used in the growth of large area GaAlAs epi-layers is shown in Figure 15. Most of the successful growth runs were made by eliminating the use of source material and growing the epi-layer in the source material slot. The reason for this change was the difficulty and expense of obtaining large-area low-impurity GaAs, the occasional slider sticking problems in passing over the source material slot, and the

GRAPHITE SLIDER BOAT (Schematic)

1/2 Scale

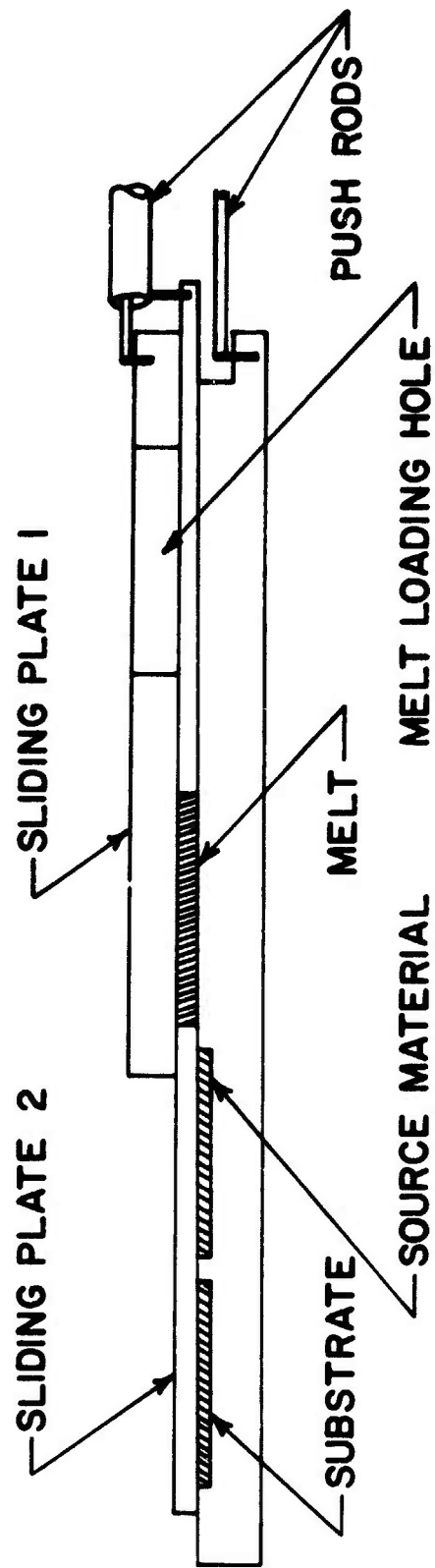


Figure 12: Schematic Diagram of Graphite Sliding-Boat System

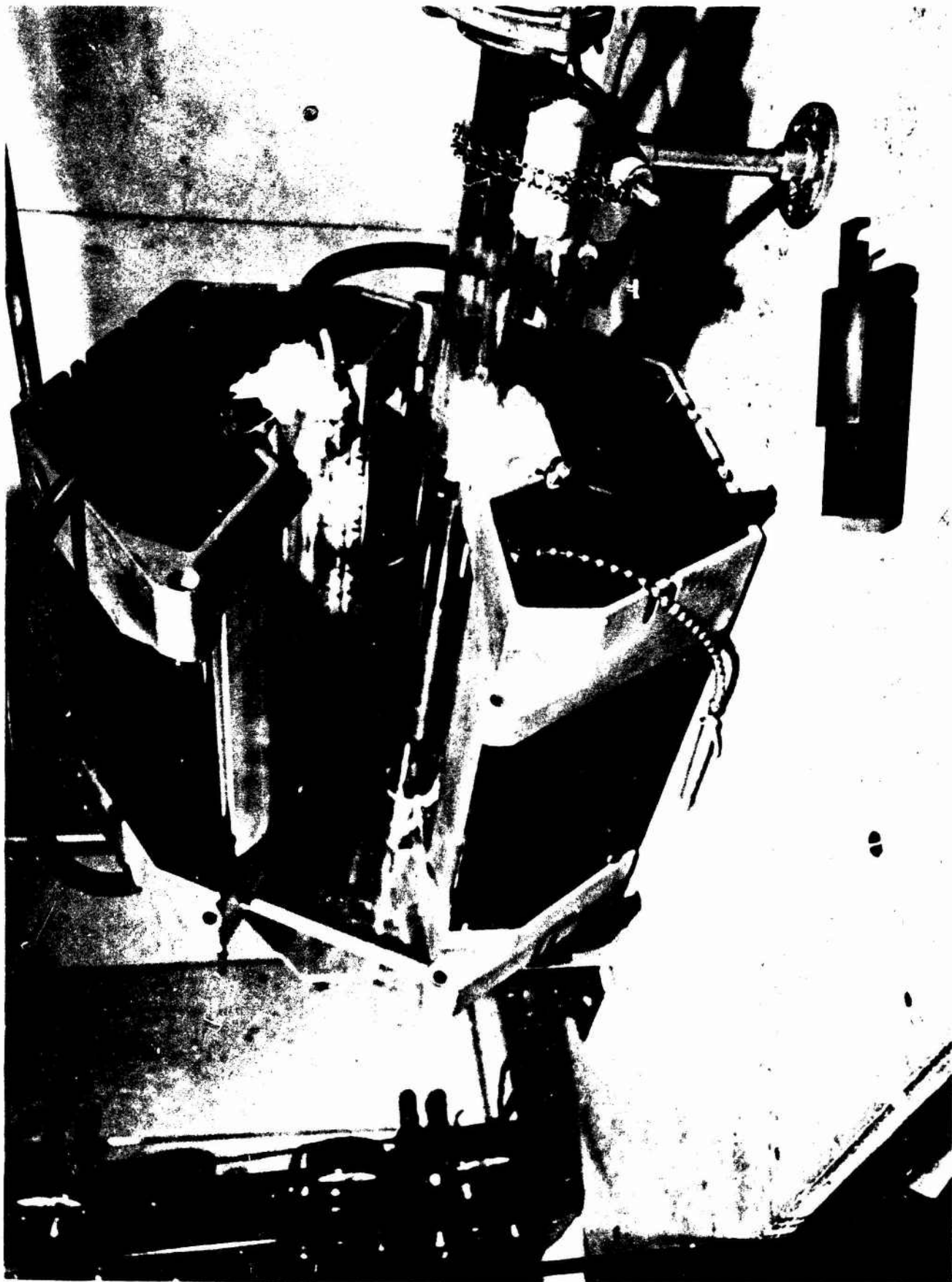


Figure 13: Radiant Heat Furnace and Melt Saturation System

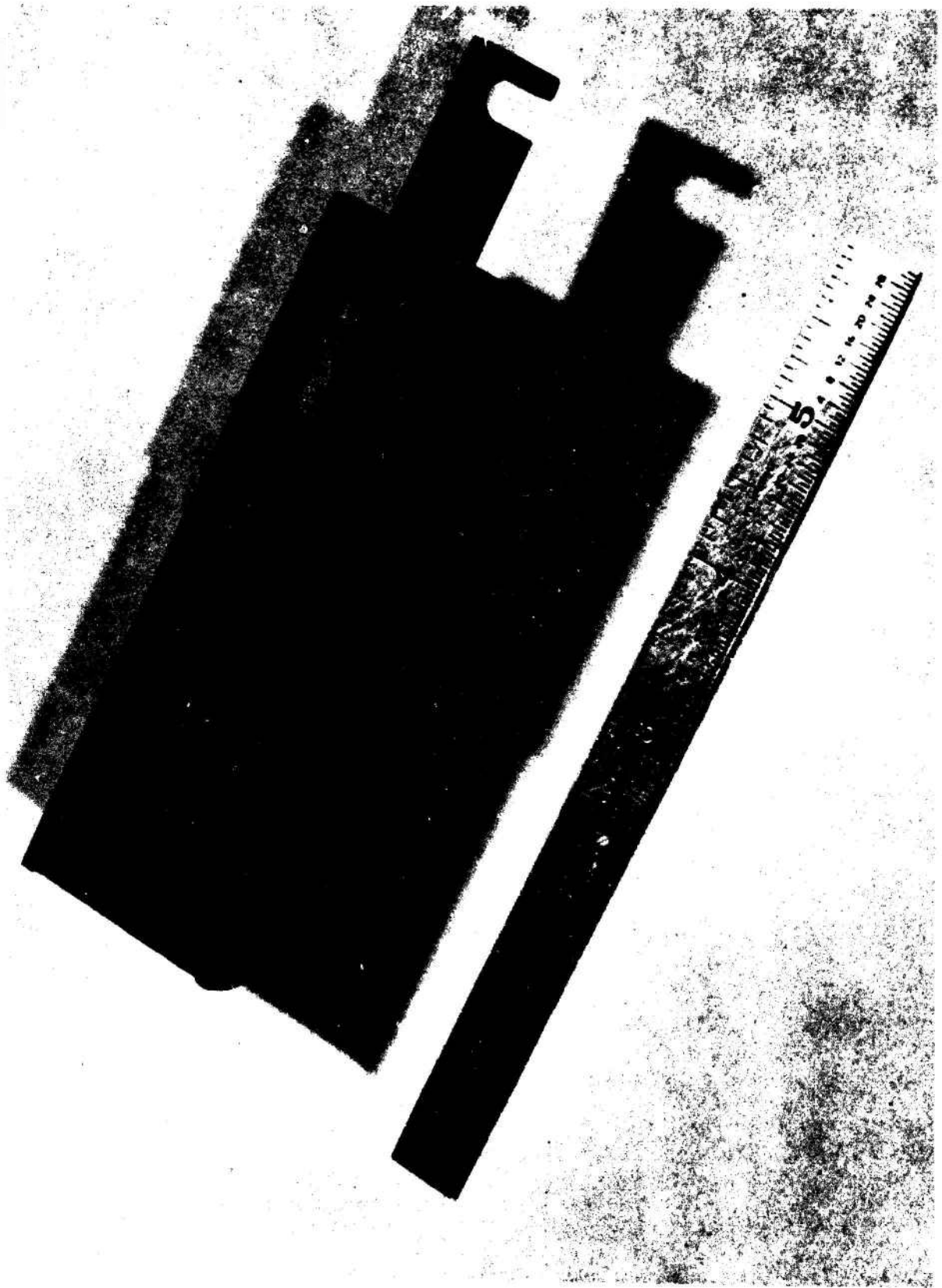


Figure 14: Gas-phase Graphite Melt Saturation Boat

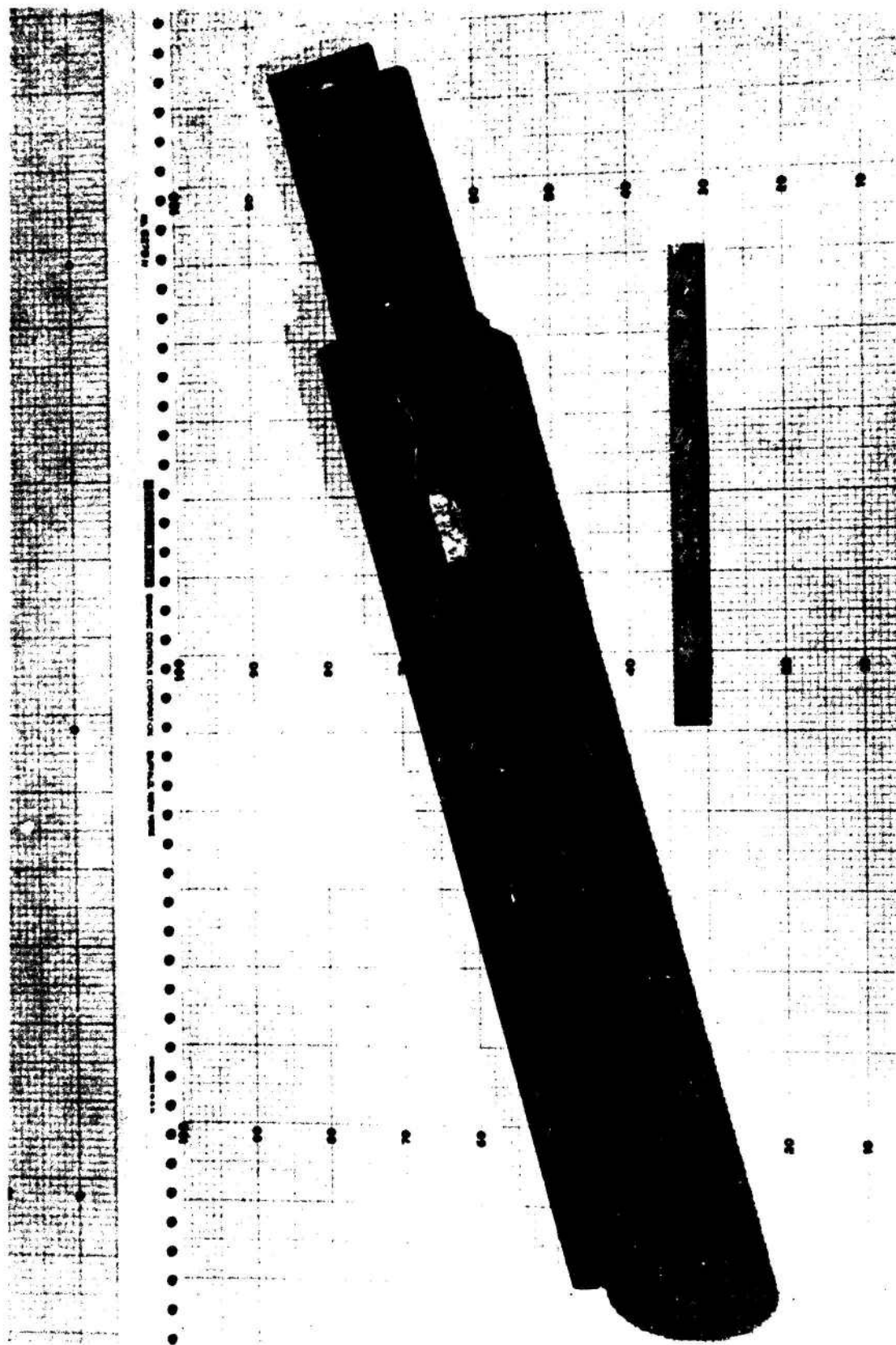


Figure 15: 12-inch Graphite Slider Boat
for Growth of Larger Area GaAlAs Layers

ease of saturating from the vapor phase in the Radiant Heat Furnace system. The loading end of the furnace and reactor tube are shown in Figure 16. The control rods provide movement of the boat and sliders while an ambient flow of purified hydrogen is passing through the reactor tube.

A series of runs was made in the 12 inch boat using substrates up to $3/4 \times 2$ inches. In Figure 16, the saturated melt containing the proper amount of Al can be seen in the right cavity and a polished substrate (GaAs) in the depression on the left side of the boat. The bottom slider moves the melt over the substrate for the growth cycle and the top slider covers the melt. After the growth cycle, both sliders are moved to the right to remove the melt from the epi-layer.

The 12 inch boat produced epi-layers with a greatly improved surface quality and layer uniformity. A schematic drawing of a typical grown layer with a surface composition of 24 mole % AlAs is shown in Figure 17. The measured layer thickness is indicated along a cleavage edge across the wafer. The layer thickness is quite uniform, $24 \mu\text{m} \pm 1 \mu$ over most of the wafer with a decreasing layer thickness only at one end where the layer first contacted the melt. The surface quality was reasonably good and, with the addition of a GaAs layer on the surface, would be adequate for preliminary waveguide evaluation.

The successful melt wipe-off action of the slider is critically dependent on the clearance between the slider and the epi-layer surface, therefore the substrate and the layer thickness must be closely controlled.

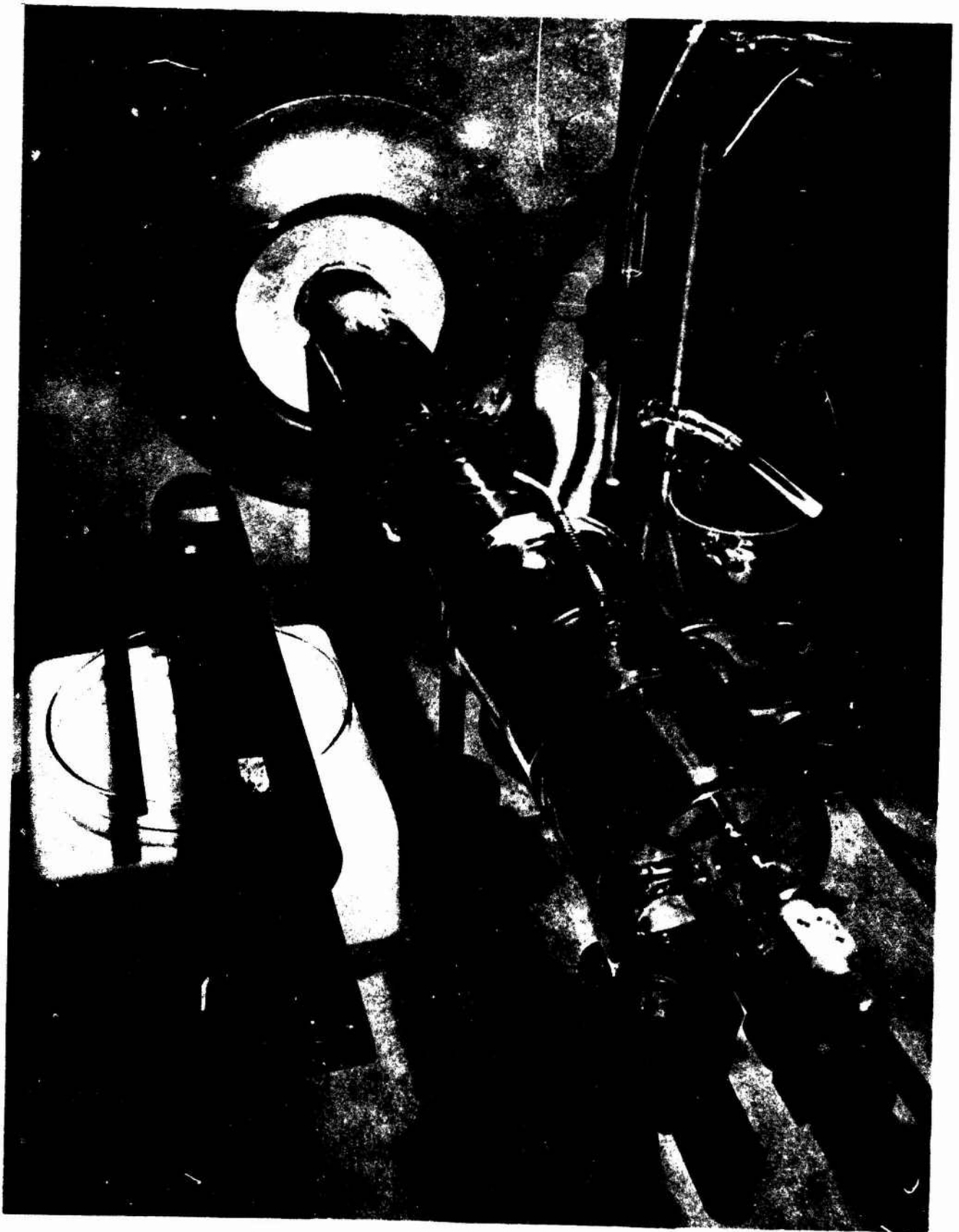
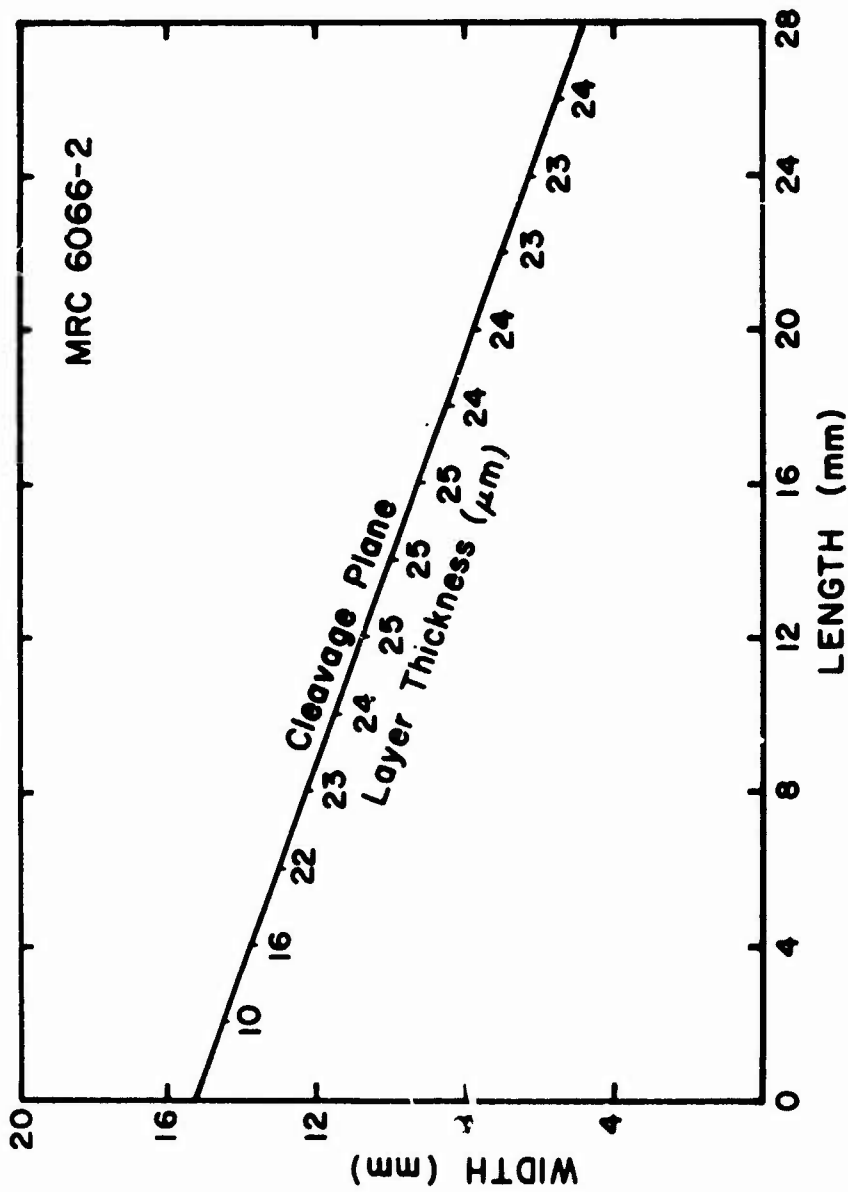


Figure 16: Loading End of LPE Growth Furnace

LPE GaAlAs

MRC 6066-2



Surface Composition: $\text{GaAl}_{.24}\text{As}_{.76}$

Epi-layer Carrier Conc: $5.0 \times 10^{16} / \text{cm}^3$

Substrate (GaAs) Carrier Conc: $6.8 \times 10^{16} / \text{cm}^3$

Figure 17

When complete melt wipe-off is obtained, the surface composition is very uniform, as measured by photoluminescence (PL). When a thin film of melt is left on the surface, a thin layer of alloy low in aluminum is deposited. This layer can be removed by a diamond polish followed by an etch polish. Since the composition gradient in the GaAlAs epi-layer is very steep, lapping slightly nonparallel to the growth surface will result in a small spread in the final surface composition. This deviation was usually kept at or below ± 1.5 mole % AlAs.

Typical LPE GaAlAs epi-layer run data obtained from the 12 inch slider boat are given in Table 12. Large area epi-layers with a surface composition in the range of 20 to 28 mole % AlAs or a PL_{300°K} wavelength of 7450 to 7000Å, respectively, were grown. A saturation or growth starting temperature near 975°C was used. The 30 to 40°C cooling cycle and a cooling rate of 0.5°C/min. resulted in epi-layers with a thickness range of 18 to 27 μm. In most of the runs a small substrate of high resistivity GaAs was included so that a Hall measurement of the epi-layer could be obtained. Most of the layers indicated a carrier concentration in the low 10^{16} cm⁻³ range with a mobility near 1500 cm²/volt-sec. at room temperature.

Some of the melt charges were reused several times by adding additional aluminum and resaturating with AsH₃. The aluminum addition required was estimated and the saturation temperature was determined by observing the first-crystal formation temperature while the melt was slowly cooled. With some experimental data and a little experience, the

TABLE 12
TYPICAL LPE GaAlAs GROWTH DATA FROM THE LARGE-AREA SLIDER BOAT SYSTEM

Run No. MRC-	Al added (g)	Saturation Temp. (°C)	Cooling Rate (°C/min)	Growth Range (°C)	Thickness (μ m)	Carrier Conc. (a/cc)	Mobility ($\frac{cm^2}{V \cdot sec}$)	PL* Wavelength (\AA)	Remarks
6065	50	975	0.5	30	27	9.4×10^{16}	1580		New 25g Ga charge
6066	28	970	0.5	35	24	5.0×10^{16}	1640	725	Resaturated melt from above
6067	50	977	0.5	35	~35	----	----	----	New 25g Ga charge, melt did not wipe clean, PL after etch polish = 7100 to 7300 \AA
6068	60	973	0.8	40	~28	2.2×10^{16}	1473	----	New 25g Ga charge, melt did not wipe clean, PL after etch polish = 6800 to 7100 \AA
6069	50	978	0.5	30	~34	5.8×10^{16}	1505	----	New 25g Ga charge, melt did not wipe clean, PL after etch polish = 6900 to 7100 \AA
6070	30	973	0.5	30	20	----	----	7330	Resaturated melt from above
6071	34	970	0.5	30	20	----	----	7040	Resaturated melt from above, p/n junction 5 μ from inter-face
6072	30	960	0.5	30	18	1.2×10^{16}	----	7140	Resaturated melt from above
6073	54	980	0.5	30	33	5.2×10^{15}	1671	7200	New 25g Ga charge
6074	30	970	0.5	35	21	1.5×10^{16}	1547	7100	Resaturated melt from above
6075	30	960	0.5	35	18	1.6×10^{16}	1074	7000	Resaturated melt from above

* (PL) = Photoluminescence at surface of epi-layer (300°K).

surface composition of the epi-layer can be kept near the desired 26 mole %
AlAs range.

4. WAVEGUIDE EVALUATION

The objectives of this portion of the program were to (a) evaluate the effects of various properties of the materials, such as alloy composition, carrier densities, and surface quality, on the propagation and attenuation of guided wave modes, (b) to measure the propagation and attenuation properties of the various modes in structures fabricated in this program, and (c) to design waveguide structures that optimize the device performance discussed in Section 5. Most of the work was conducted at the $10.6\ \mu\text{m}$ wavelength. A limited amount of data was also collected at the $1.06\ \mu\text{m}$ wavelength.

4.1 Planar Waveguide Propagation and Attenuation at $10.6\ \mu\text{m}$

A Coherent Radiation Model 42 CO_2 laser was used for the experimental measurement of waveguide attenuation. An intracavity grating was used to select the laser transition, stabilizing the wavelength of the output radiation. This is particularly important if a grating coupler is used to excite the guided wave modes. A piezo-electric feedback control was then added to stabilize the cavity length, so that constant output power from the laser was obtained. The schematic diagram of this laser stabilizer is shown in Figure 18. An intracavity mode selector was used to insure that the output radiation is in the TEM_{00} mode. Both gratings and prisms have been used to couple the CO_2 laser radiation into the waveguides, but we finally standardized on the prism coupler for excitation and the two prism method for the attenuation measurement. We chose the prism coupler because low loss Ge prisms were readily available; input coupling efficiency of 40% can easily be obtained; many data points can be obtained

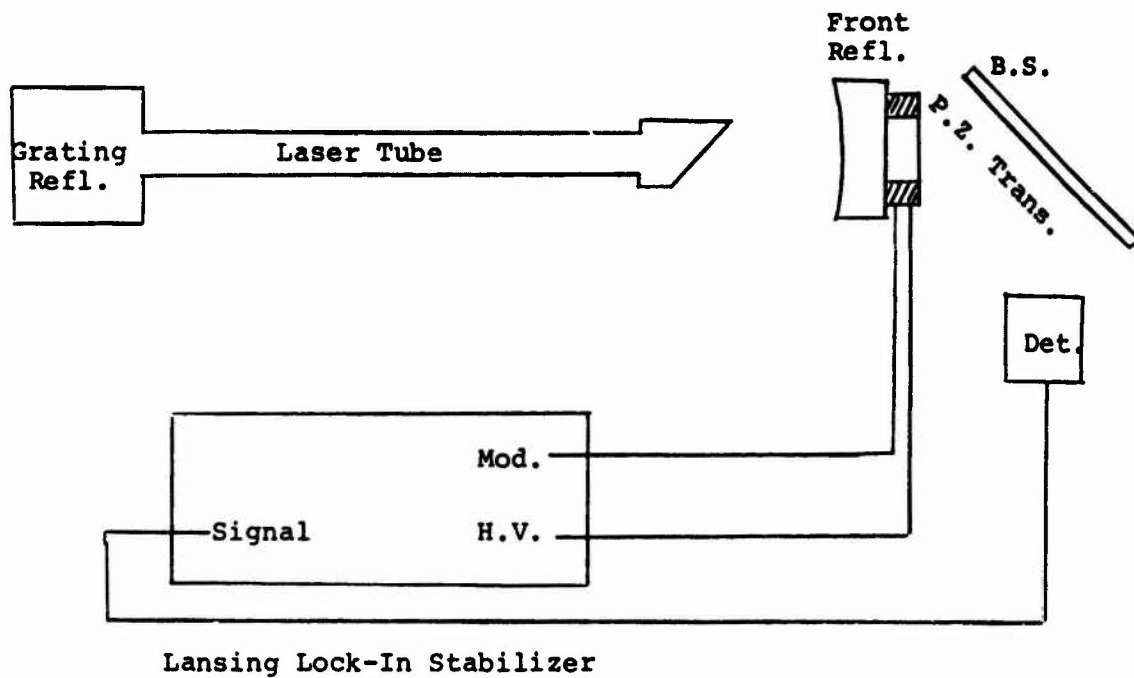


Figure 18: Schematic Diagram of the CO₂ Laser Stabilizer

by adjusting the position of the output prism coupler; and the waveguide is reusable.

In our experimental measurements, the waveguide was bonded by black wax coated on the back side of the waveguide structure to a fixture so that the prisms could be safely pressed against the waveguide. The fixture was then mounted on a 5 inch diameter Lansing gimbal-mount riding on two translational stages, providing fine control of the angular and translational position of the waveguide with respect to the laser beam. The prism couplers were epoxied to a set of mechanical harnesses that enabled us to control the pressure of the prisms against the waveguide by controlling the spring pressure. The prisms could slide back and forth, accurately and conveniently. Figures 19 and 20 show the fixtures.

As soon as the guided waves are excited by adjusting the angular orientation and translational position of the waveguide with respect to the incident laser beam, a search is conducted for the exact angles of excitation for each mode. Comparison of these angles with the calculated values of β enables us to identify the specific modes involved in each attenuation measurement. Figure 21 is a typical semi-log plot of the measured output power detected by the thermocouple detector as a function of the path length (the separation between prisms). The data shown in this figure are for the $m=0$ and $m=3$ modes of a GaAs/n+GaAs waveguide. The average slope of all the points is the attenuation rate of that mode. The scatter of the experimental points demonstrates the experimental errors of the measured attenuation rate. The experimental

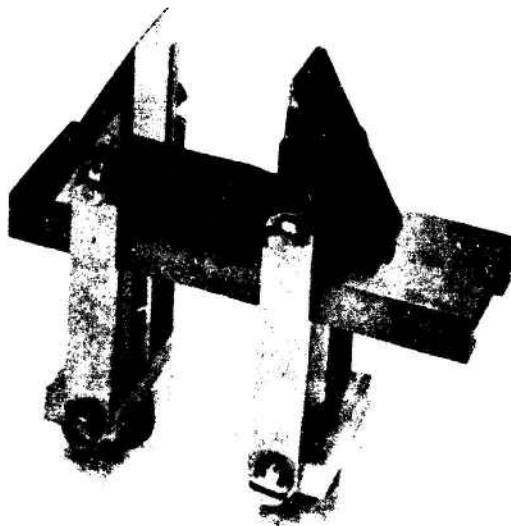
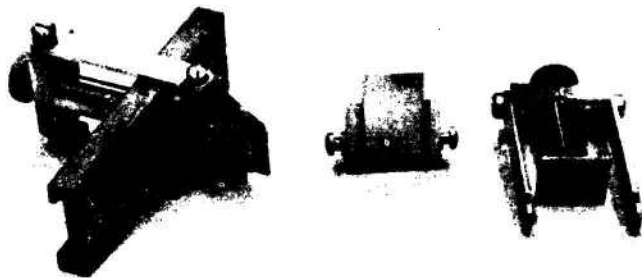


Figure 19: The Prism-Prism Coupler Assembly



Figure 20: Measurements of Attenuation Rate by the Prism-Prism Coupler

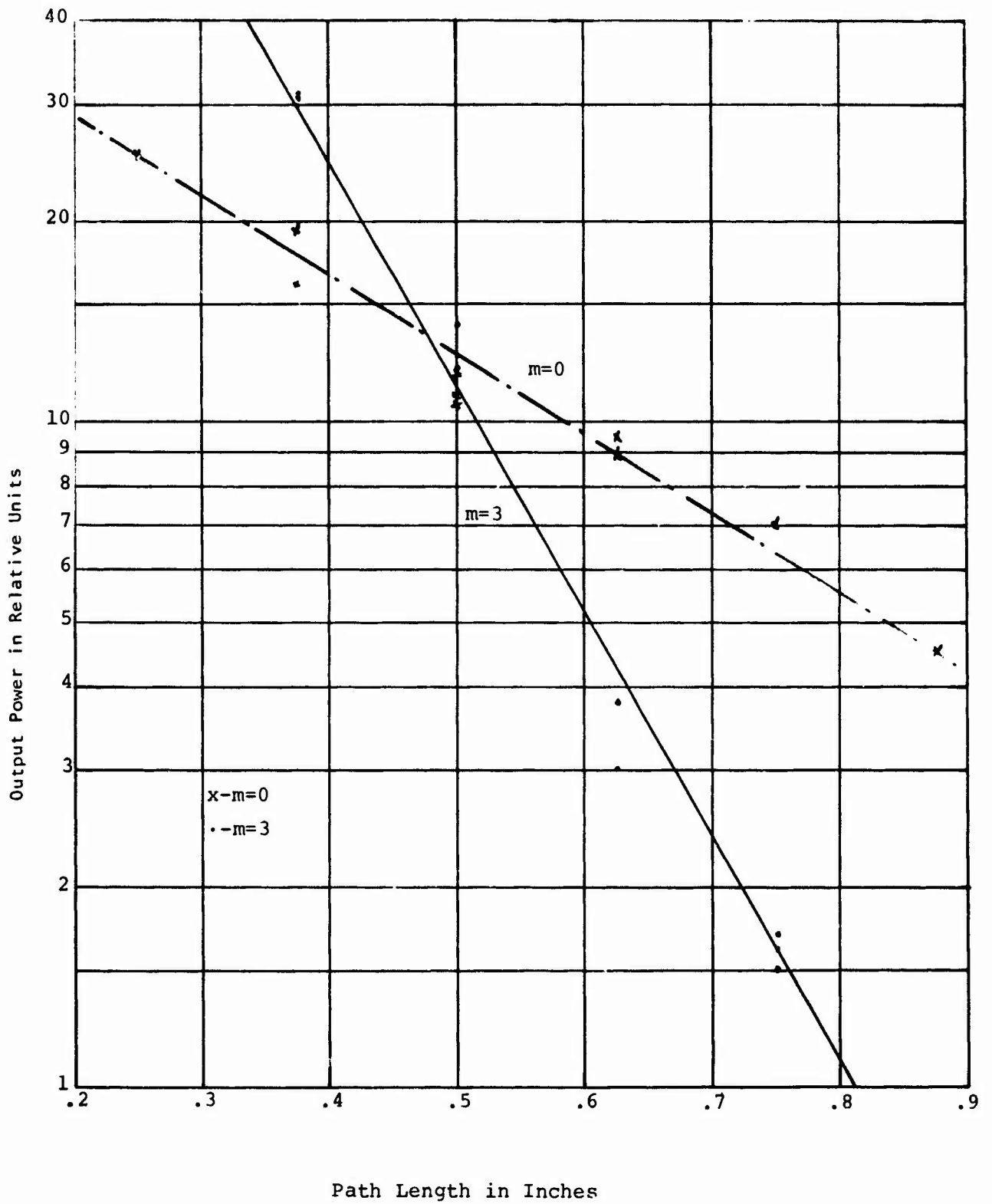


Figure 21: Relative Output Power as a Function of the Path Length

errors could be caused by irregularities (including both defects and dust particles) of the waveguide surface and by fluctuations in the detected power. By stabilizing the laser power and by using a chopper and the synchronous detection method to eliminate noise, we eliminated the power fluctuation error from most of the measurements. The estimated accuracy of our measurements in attenuation rate is within 1 db/cm.

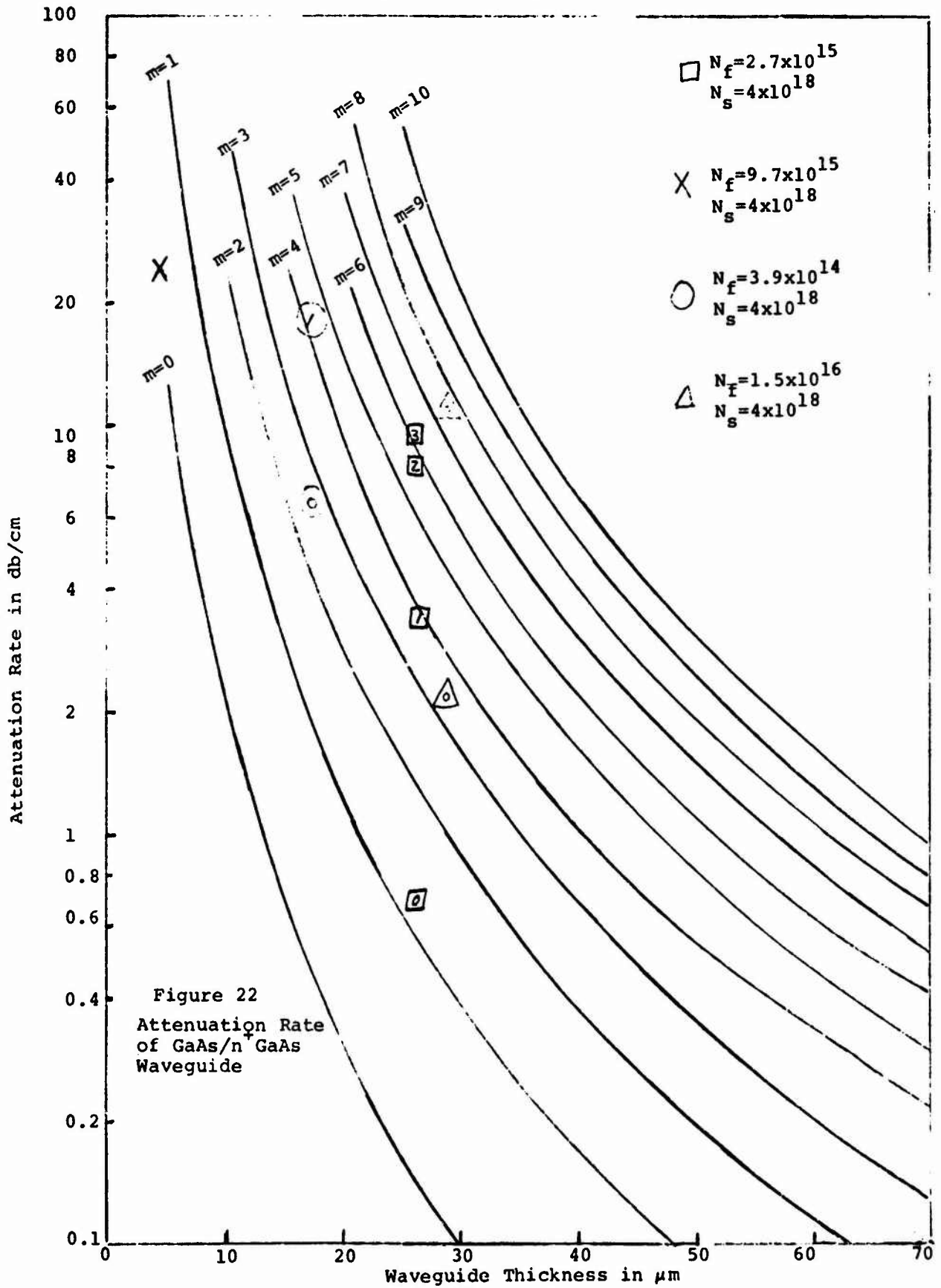
4.1.1 GaAs/n + GaAs Waveguides⁽⁸⁾

The total attenuation coefficient of a given waveguide is the sum of three parts: attenuation due to free carrier absorption in the substrate, absorption loss within the bulk of the film, and scattering loss at the air-film boundary and at the substrate-film interface. The absorption loss of bulk high resistivity GaAs has been measured calorimetrically and was found to be 0.012 cm^{-1} ⁽⁹⁾. The surface irregularities of the waveguides fabricated are less than 1/10 of the wavelength. Therefore, in the initial theoretical assessment of the attenuation rate of GaAs/n+GaAs waveguides, we have only calculated the attenuation due to free carrier absorption in the substrate. The theoretically calculated attenuation rate of the various TE modes are shown as solid curves in Figure 22 as a function of the waveguide thickness. The film is assumed to be lossless and the substrate is assumed to have a carrier concentration of $4 \times 10^{18} \text{ cm}^{-3}$. The absorption coefficient of the GaAs at $10.6 \mu\text{m}$ is related to free carrier concentration N by^(6, 7)

$$\alpha \text{ (in } \text{cm}^{-1}\text{)} = 8.10^{-17}N$$

The measured attenuation data are shown by the points marked by their mode order in the same figure. The attenuation increased rapidly either

$N_s = 4 \times 10^{18}$ $n_f = 3.27$



as the mode order is increased or as the waveguide thickness is decreased. The increase in attenuation is attributed to the lengthening of the evanescent tail in the substrate which is highly absorbing.

It has been thought that the waveguide attenuation rate may be reduced by using a substrate with a lower carrier concentration. However, in order to achieve good waveguiding in GaAs/n+GaAs, a carrier concentration on the order of 10^{17} cm^{-3} is required. We have found that a decrease in the substrate carrier concentration will increase the attenuation rate. This comes about because the evanescent tail of a guided mode is lengthened by the decrease in carrier concentration, and it penetrates more into the lossy substrate. In spite of the simultaneous decrease in the free carrier absorption, our calculation reveals a higher attenuation rate at a lower substrate free carrier concentration for GaAs films thicker than 10 microns. A better way to achieve both a larger change of the refractive index for the waveguiding effect and a lower substrate bulk loss is to go to a heterostructure, which will be discussed in the next two sections.

In order to show the attenuation characteristics of an assortment of GaAs/n+GaAs waveguides with a variety of substrate carrier concentrations, we have plotted in Figure 23 the attenuation of the TE_0 and TE_1 modes where the substrate carrier concentration varies from 8×10^{17} to $4 \times 10^{18} \text{ cm}^{-3}$ and the film carrier concentration varies from 4×10^{14} to $2 \times 10^{15} \text{ cm}^{-3}$. The dashed lines are an attempt to join all the experimental points together. They are intended to give a general assessment of the effect on attenuation rate caused by the change in film thickness without regard to the slight variation in free carrier concentration of the different substrates. Also

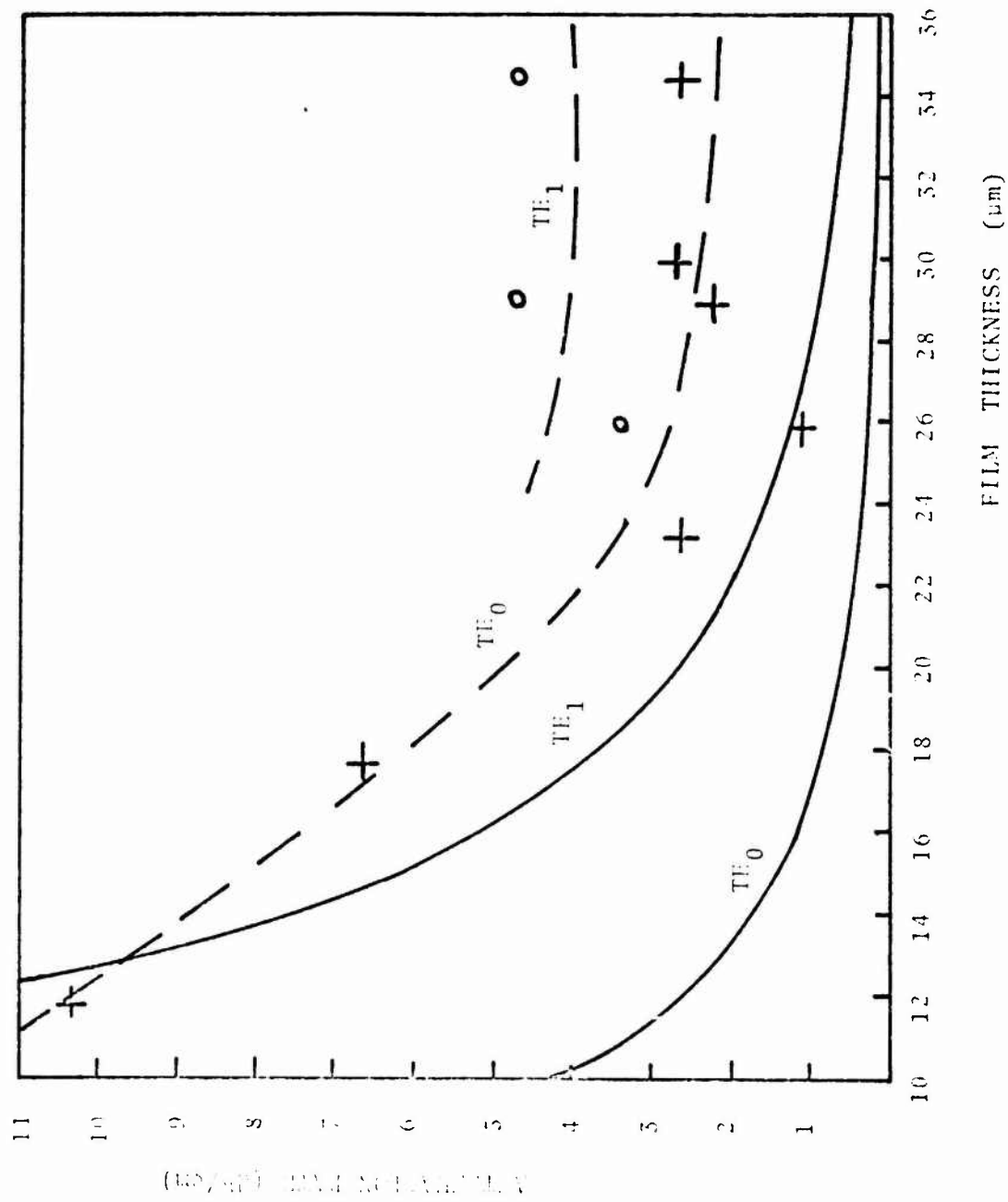


Figure 23

shown in Figure 23 are two theoretical curves (solid curves) for the loss due to the free carrier absorption of the substrate. In this theoretical calculation, the GaAs film is assumed lossless and the substrate has a carrier concentration of $2 \times 10^{18} \text{ cm}^{-3}$ which is an average of all the samples used in obtaining the experimental points. A conclusion can be drawn here that an attenuation rate less than 2 db/cm for the TE_0 mode is achievable consistently in the GaAs/n+GaAs structure provided that the film thickness is about $25 \mu\text{m}$ or thicker. The minimum attenuation rate achieved in a waveguide is 0.7 db/cm. It should also be clear from Figures 22 and 23 that the total attenuation rates of the low loss waveguides are considerably higher than the attenuation rate calculated from the free carrier absorption of the substrate. No specific mechanism has yet been identified which causes this residual $\sim 1 \text{ db/cm}$ of attenuation.

In order to assess the effect of nonuniform carrier concentration near the n+GaAs junction, we have analyzed the propagation wavenumber β for each mode with uniform refractive index in the film and linear variation of the refractive index in a given transition region. Numerical results have been obtained which indicate that as far as the calculation of β is concerned the waveguide with a graded index of refraction can be represented by an equivalent uniform film waveguide having an effective thickness w_0 . Figure 24 shows an example of the calculated results. In this figure, a contour map of the ratio of β of the TE_0 mode to the free space propagation wave number, k , is presented as a function of the film thickness w and transition region thickness d at $10.6 \mu\text{m}$ wavelength.

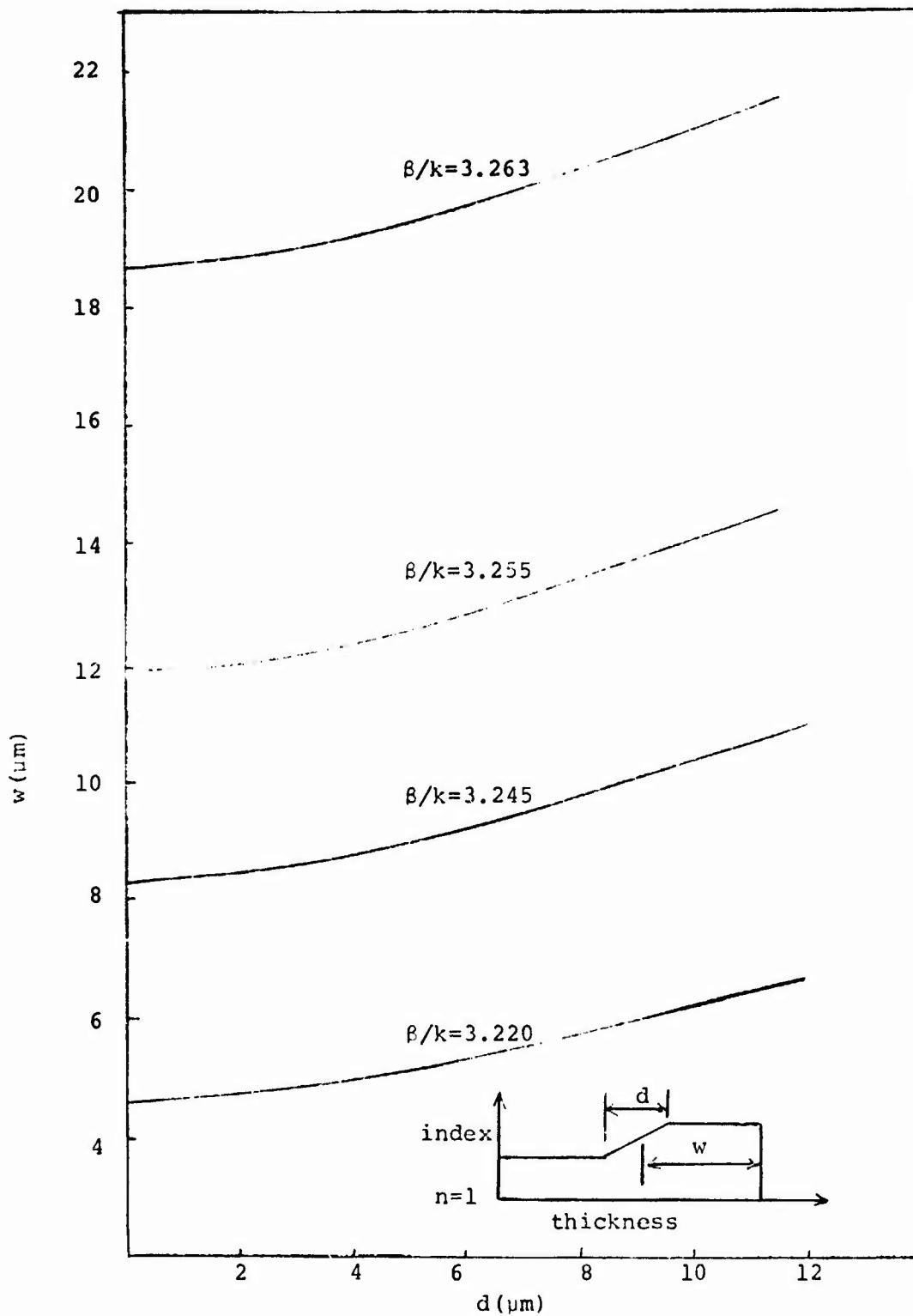


Figure 24. Contour Map of β for Graded Refractive Index Waveguide

These are GaAs/n+GaAs waveguides with $N_b = 10^{18} \text{ cm}^{-3}$ substrate carrier concentrations. An extension of the analysis has also been made to calculate the field configuration for the mode. From the field calculation, the attenuation rate of the waveguide was calculated and is presented in Figure 25. Figure 25 shows the attenuation rate curves for the TE_0 mode for the waveguides that have the w and the d values corresponding to the specific β/k values shown in Figure 24.

The calculation demonstrated that with the transition region measured to be less than 1μ thick for most of the GaAs abrupt layer waveguides, the effect of the transition region on β and on attenuation rate can be neglected. The calculated results were used as a guide for the fabrication and evaluation of waveguides. Based upon this calculated result and the carrier concentration profile shown in Figure 3, we have concluded that the effect of the graded region on waveguide propagation and attenuation is negligible at the $10.6 \mu\text{m}$ wavelength. However, the effect of the graded layer is not negligible at the $1.06 \mu\text{m}$ wavelength.

4.1.2 GaAs/GaAs_{1-x}P_x Waveguides

In principle the waveguide attenuation caused by substrate absorption can be made arbitrarily low by reducing the free carrier concentrations in GaAs_{1-x}P_x. In practice the free carrier concentration that can be achieved is shown in Section 2.1.2 to be $\sim 10^{15}$. There is also a lack of experimental data on the exact value of the refractive index of GaAs_{1-x}P_x at $10.6 \mu\text{m}$. We found that a relationship of $\Delta n = -0.4x$ fits fairly well with the incomplete existing data. A detailed discussion of the refractive

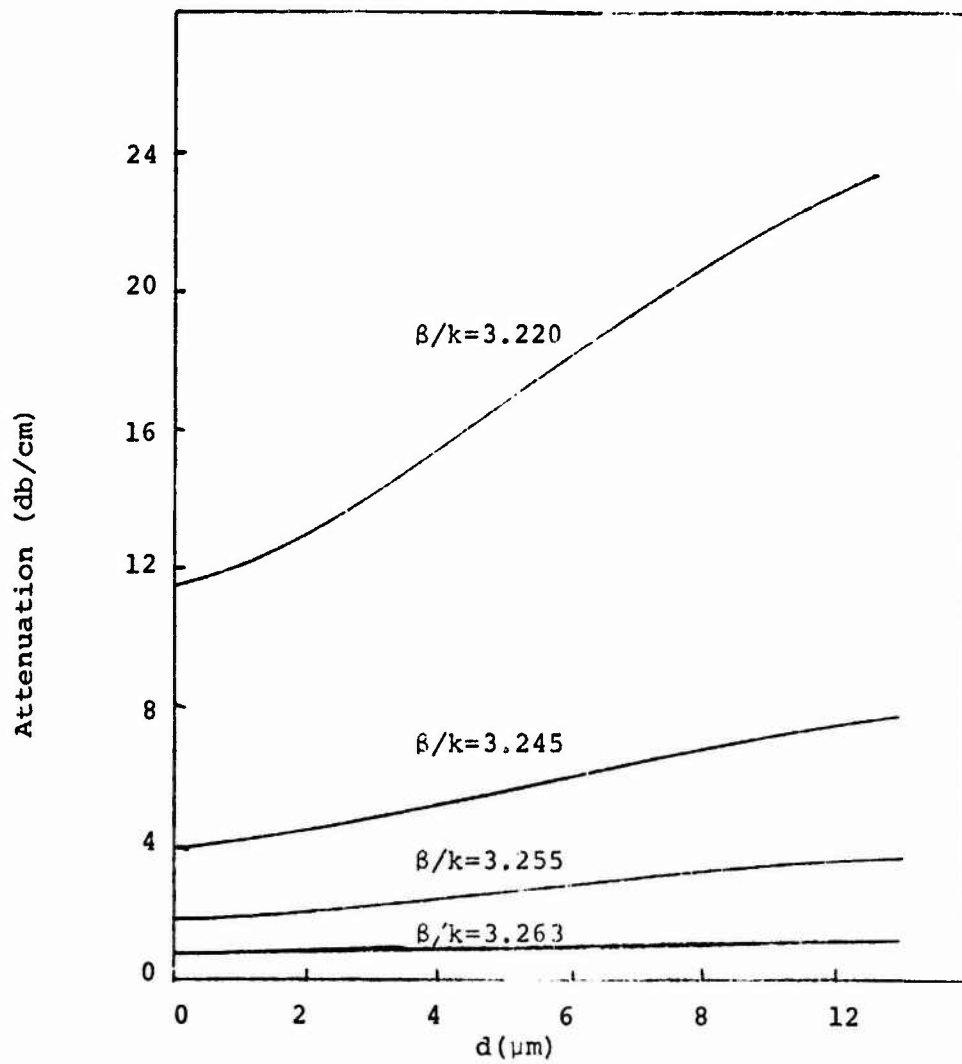


Figure 25 Attenuation Rate of Graded Index Waveguide

indices of GaAs, GaAsP, and GaAlAs is given in Appendix 3. Several GaAs/GaAs_{1-x}P_x waveguides were fabricated specifically for the evaluation of the refractive index in collaboration with Dr. James McFee of the Bell Telephone Laboratories. The index does not seem to be uniform enough within the GaAs_{1-x}P_x epitaxial film to permit us to determine the refractive index more accurately than the presently known value.

Based upon the assumption that the substrate refractive index is 3.12 and the substrate absorption is 2.5 cm⁻¹, we have calculated the attenuation of the GaAs/GaAs_{1-x}P_x waveguides. These are shown as the solid curves in Figure 26. The points are the measured attenuation rates of the TE₀ and TE₁ modes. Note that the GaAs/GaAs_{1-x}P_x waveguides have considerably less attenuation than the GaAs/n⁺GaAs waveguides at small GaAs film thicknesses. The increase in attenuation rate near the cut off film thickness of the waveguide is caused again by the free carrier absorption in the substrate which was in the range of 10¹⁶ cm⁻³ for the samples used for these measurements. Lower carrier concentrations have been achieved in GaAs_{1-x}P_x near the end of the contract period; but these samples have not yet been evaluated. There is again a residual attenuation of about 1 db/cm caused either by surface scattering or absorption of the film. We have suspected that the attenuation may be caused by the very thin layer of oxides that may develop on the surface of GaAs; but no conclusion was reached at the end of the contract. Waveguides with loss of less than 1 db/cm can be fabricated by increasing the GaAs film thickness. For films thicker than 20 μm, the attenuation for the fundamental mode is so small that it is not measurable. However, a multimode waveguide is not

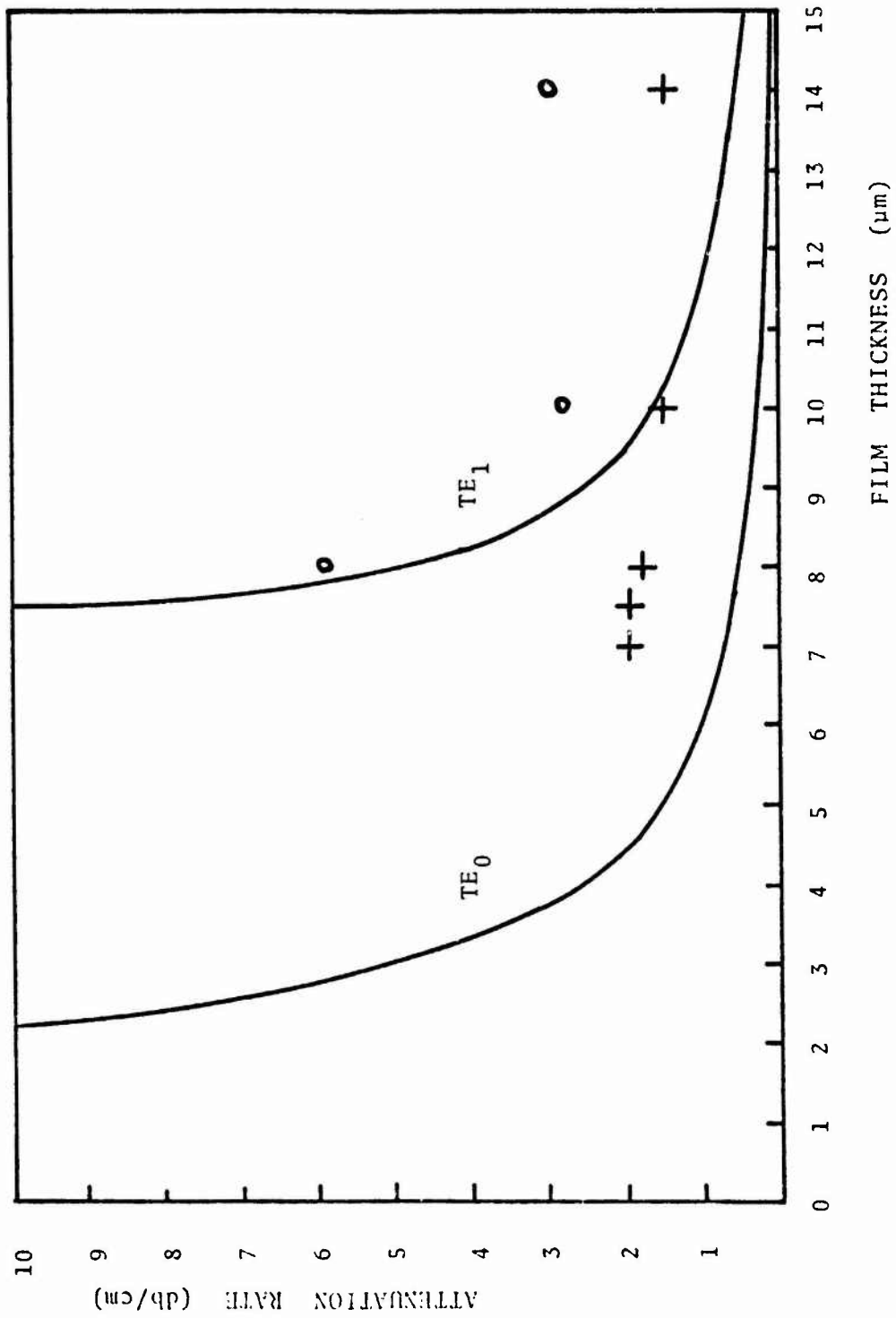


Figure 26

desirable from the device design point of view. No measurable effect on the attenuation rate could be correlated with the variations in cross hatch patterns.

We have also grown a number of GaAsP/GaAs/GaAsP waveguides. The symmetric waveguide structure is similar to Figure 4, except for an additional layer for GaAsP on top of the GaAs. Again, we have neglected the grading at the top interface. The purpose of the additional GaAsP layer is to isolate the metal layer in our device design, e.g. in electro-optic modulators. This buffer layer is thick enough so that the exponential tail of the guided mode does not reach the metal layer. The growth condition for this buffer layer is the same as for the uniform GaAsP substrate, and its thickness ranges from 4 to 12 μm . All the samples grown to date have good surface quality. Waveguide attenuation measurements were performed on a single-mode sample with a 5 μm GaAs light guide and a 5 μm GaAsP buffer layer. A loss of 6 db/cm was obtained. We have expected the loss of the GaAsP/GaAs/GaAsP waveguide to be twice that of the GaAs/GaAsP waveguide.

4.1.3 GaAs/Ga_{1-y}Al_yAs Waveguides

In principle, the GaAs/Ga_{1-y}Al_yAs waveguide should have the same characteristics as the GaAs/GaAs_{1-x}P_x waveguide as long as they have the same index of refraction and the same free carrier absorption for the substrate. In practice the control of film thickness uniformity, of free carrier concentrations, and of surface quality for large samples are different in the VPE process and the LPE process. We have chosen to

grow the GaAlAs substrate layer by the LPE process, followed by VPE growth of the waveguiding layer so that the free carrier absorption loss of the film can be eliminated. The attenuation rate measured was 3 db/cm for the TE₀ mode and 5 db/cm for the TE₁ mode in our best sample with a film thickness about 8 μm. The sample was much smaller than our usual sample size produced in the VPE process; and the measurement was performed over a distance of separation about 5mm between the two prisms. A GaAs/AlGaAs waveguide structure with both GaAs and AlGaAs grown on a GaAs substrate by liquid phase epitaxy has been reported recently by McFee, et al⁽¹⁰⁾. This Ga_{1-y}Al_yAs typically has an alloy composition with y in the range of 0.2 - 0.3. The GaAs film and the AlGaAs substrate have thicknesses from 10 to 20 μm and the carrier concentrations in both layers are approximately in the 10¹⁶ cm⁻³ range. Waveguide samples are typically one to two centimeters in size, and the attenuation measurements were performed over a distance up to about 5mm. For the TE₀ mode, a loss of about 2 db/cm was measured, but much higher loss was obtained for the TE₁ and TE₂ modes.

Judging from the initial results obtained by us and by Bell Telephone Laboratories⁽¹¹⁾, we believe that the attenuation rate for the GaAs/AlGaAs waveguide structure can be reduced to below 2 db/cm by improving the perfection of the film surface quality and by reducing the carrier concentrations. The carrier concentration of the GaAs film that can be obtained by liquid phase epitaxy was reported by McFee, et al. to be approximately 10¹⁶ cm⁻³, while that by our vapor phase epitaxy could be controlled in the

10^{14} cm^{-3} range. However our technique is subject to the inherent difficulty of combining vapor phase epitaxy with liquid phase epitaxy.

4.2 Two Dimensional Waveguides at $10.6 \mu\text{m}$

Investigation of electrooptical modulation predicts that a large reduction of r.f. power per modulation bandwidth and higher r.f. power per modulation bandwidth and higher r.f. impedance may be obtained by using a two dimensional waveguide modulator to reduce the capacitance. However, it is well known that the scattering loss from the rough side walls may significantly increase the attenuation rate. We have successfully chemically etched two dimensional waveguides that have very low loss.

For the sample VR5-422 the measured attenuation rate for the TE_0 mode is 4.1 db/cm while the attenuation rate for the TE_1 mode is 5 db/cm. These measurements are for a one dimensional guide before etching. Subsequently, the sample was first spin coated with liquid SiO_2 $0.15 \mu\text{m}$ thick, and then spin coated with AZ 1350 photoresist, about $0.5 \mu\text{m}$ thick. AZ 1350 was exposed in the usual manner through a suitable photomask (made by the conventional photolithography technique) to make an SiO_2 mask to protect the white areas in Figure 27 during chemical etching. Following that the GaAs (dark area in Figure 27) was etched about $25 \mu\text{m}$ deep by $\text{H}_2\text{SO}_4:\text{H}_2\text{O}_2:\text{H}_2\text{O}$ (3:1:1) at 45°C for about five minutes; the SiO_2 mask was then removed by HF.

The resultant product schematically shown in Figure 27 consists of a two-dimensional waveguide surrounded by deep etched grooves to isolate the waveguide from the surrounding mesa of GaAs. The two-dimensional

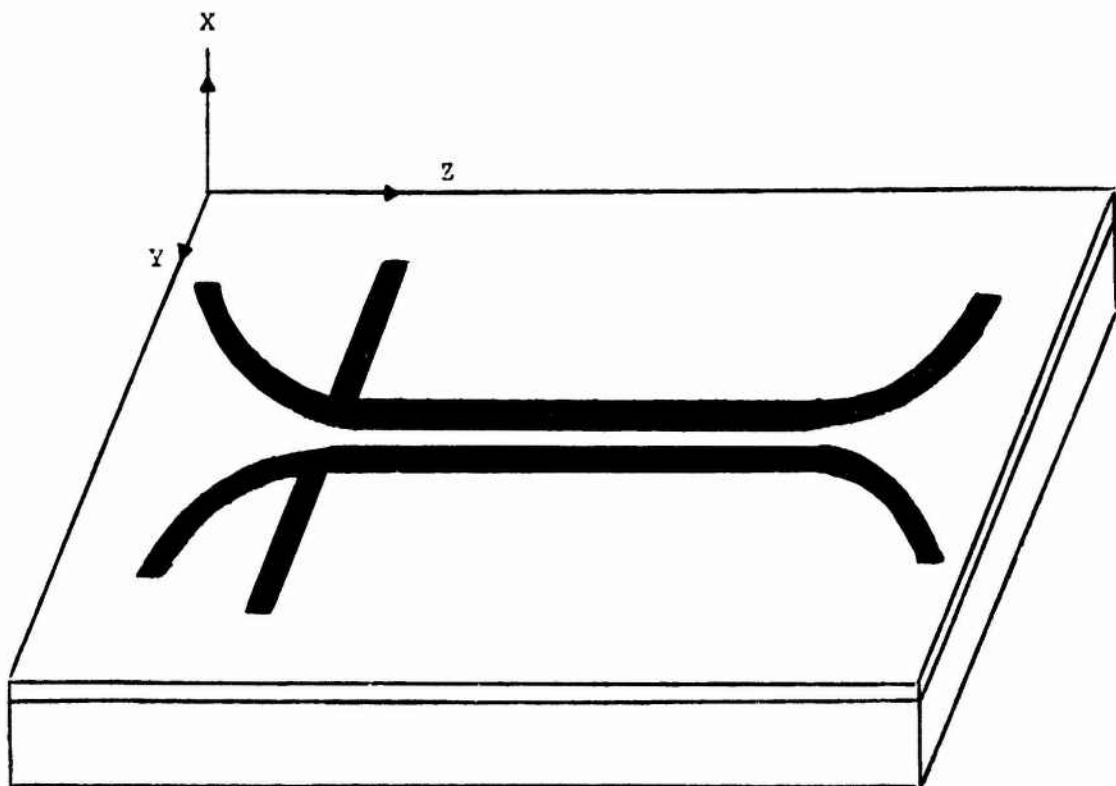


Figure 27. Schematic Diagram of an Etched Two Dimensional Waveguide.

waveguide has tapered transitions at both ends so that one dimensional waveguide modes can be excited by the prism coupler and then make a smooth transition from the one dimensional waveguide modes to the two-dimensional waveguide modes. The surrounding mesa of GaAs is necessary to support the pressure of the prism coupler. The vertical deep groove cutting across the mesa shown in Figure 27 is necessary to prevent radiation leaking from the input prism coupler to the output prism coupler through the surrounding mesa of GaAs. Figure 28 shows a 500X magnification of a section of the etched waveguide where each large scale division corresponds to $2.2\mu\text{m}$ in distance. Figure 29 shows the profile of the waveguide as monitored by Dektak. The surface irregularities caused by chemical etching are clearly much less than $1\mu\text{m}$.

We have been able to excite several E_{1q}^y and E_{2q}^y modes by setting the vertical angle of the incident CO_2 beam with the input prism for $m = 0$ and $m = 1$ modes of the one dimensional waveguide. Modes having various values of q , the transverse mode order along the width of the two dimensional waveguide, were excited by adjusting the horizontal angle between the input prism and the axis of two-dimensional guide. When attenuation rates of the two-dimensional guide were evaluated by sliding the output prism coupler, we obtained 3.8 db/cm for E_{1q}^y modes and 4.9 db/cm for E_{2q}^y modes for small values of q .

This result demonstrated that no measurable increase in attenuation occurred for the two-dimensional waveguide modes E_{1q}^y and E_{2q}^y (with small q values) as compared to the TE_0 and TE_1 one-dimensional waveguide

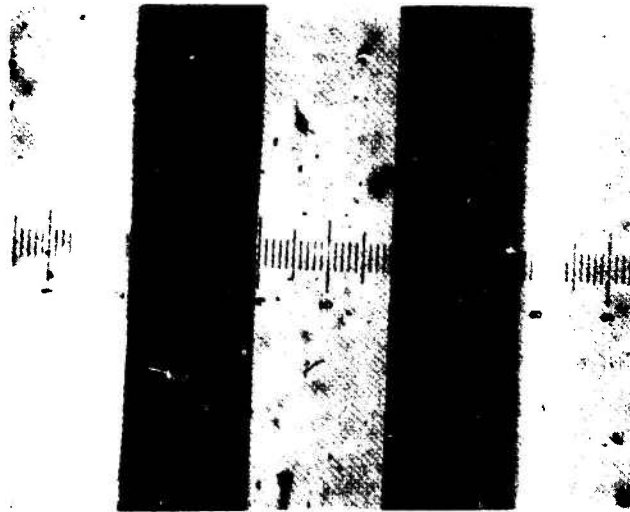


Figure 28. Photograph (500x) of a Part of the 50μ Wide Two Dimensional Waveguide Fabricated on VR5-422.



Figure 29. Dektak Trace Showing Profile of the 50μ Wide Two Dimensional Waveguide. Horizontal Magnification 100, Vertical Full Scale 50μ .

modes. The slight decrease in attenuation was probably caused by the fact that we chose a better section of the sample to make the two-dimensional waveguide. Similar results were obtained in Sample No. VR5-424 where a 50 μm wide two-dimensional waveguide was fabricated. However, when a 25 μm wide two-dimensional waveguide was fabricated on Sample No. VR5-421 an increase of attenuation of 1 db/cm occurred for the E_{1q}^Y modes and an increase of attenuation of 6 db/cm occurred for the E_{2q}^Y modes.

4.3 Planar Waveguide Propagation and Attenuation at 1.06 μm

The GaAs/GaAs_{1-x}P_x waveguide for 1.06 μm wavelength application is fabricated in the same manner as those for the 10.6 μm wavelength, except that the film is thinner. However the measurement technique is modified because the Ge prism is not transparent at the 1.06 μm wavelength. We have succeeded in exciting the guided waves by both a GaAs prism coupler and a grating coupler. The details of these couplers will be discussed in Section 5.2. For attenuation measurements, the grating coupler method has the disadvantage that the distance between input and output coupler is fixed, so that a number of samples are needed to obtain the necessary data. The prism coupler method has the disadvantage that the coupling efficiency is less than 0.1% because the index of the prism is almost the same as β_g/k . In addition the energy contained in the evanescent tail is a very small fraction of the total energy carried in the guided wave mode whenever $n_s \approx n_f$; the evanescent tail is too short for strong coupling between the prism and the waveguide through the air gap. Both of these factors contributed to the low prism coupling efficiency.

The efficiency is so low that the attenuation measurement by the two prism method is no longer reliable. A compromise was finally used for the attenuation measurements. The two prism method was used first to identify the modes and to evaluate the mode conversion effects between different modes. The output prism coupler was then dismantled and the radiation emerging from the cleaved surface at the end of the waveguide detected. Since the reflection loss at the end of the waveguide is of the order of 30%, the radiated power can be measured accurately. The input prism coupler can then be moved to measure the change in detected power due to transition in propagation distance in the waveguide. Surprisingly the input coupling efficiency is fairly constant, causing only a small amount of scatter in the measured data points in the semi-log plot of the detected power versus propagation distance as shown in Figure 30. For the single TE mode and the double TE mode waveguide the measured attenuation rate of the TE₀ mode is about 1 db/cm. These waveguides have a film thickness of 1 to 2 μm and 35% GaP in the substrate. For waveguides that have several propagation modes, strong mode conversion between different modes was observed. No matter what mode is excited at the input coupler, the output coupler shows m-lines of equal intensity after a few mm of propagation distance. This strong mode conversion effect is attributed to the surface scattering by the cross hatch pattern. In section 2.1.3, Figure 7 (a) showed the surface profile pattern of this cross hatch pattern as monitored by DEKTAK. Notice that the average periodicity of the cross hatch pattern satisfies approximately the phase matching condition between different modes. This suggests that the cross hatch pattern will cause strong mode conversion, but its periodicity is too large to cause any significant increase in waveguide attenuation. The cross hatch

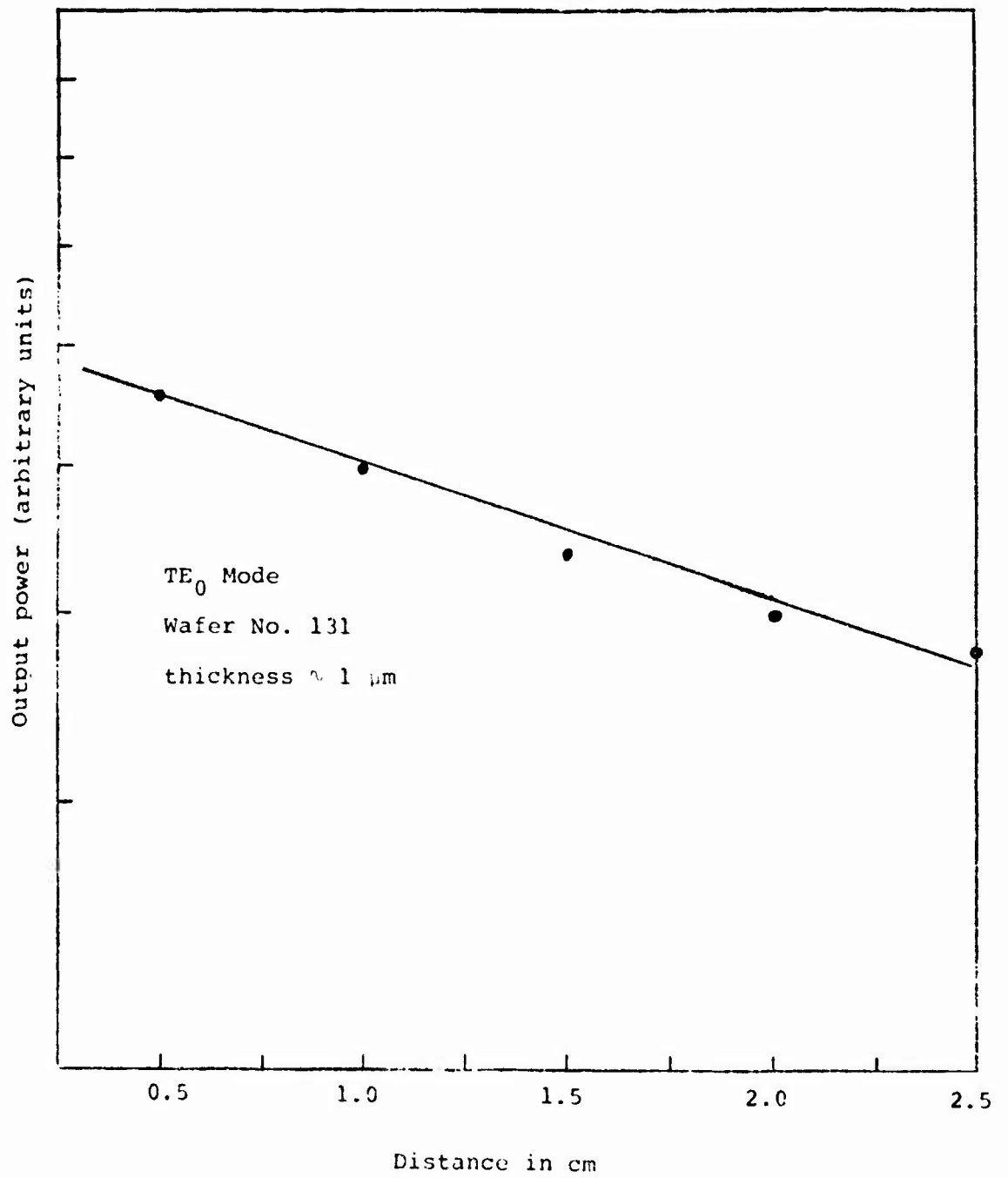


Fig. 30: Determination of Waveguide Attenuation at 1.06 μm Wavelength

pattern was reduced in GaAs/GaAs_{0.79}P_{0.21} and in GaAs_{0.8}P_{0.2}/GaAs_{0.6}P_{0.4} waveguides as shown in Figure 7(b) and (c). The measured attenuation rate of the sample that has a less pronounced cross hatch pattern is $\sim 1-2$ db/cm. Because of the limitation in time no thick waveguides could be fabricated before the end of the contract period to examine the detailed mode conversion properties of the cross hatch pattern. Free carrier absorption is not the dominant loss mechanism for waveguide attenuation at $1.06 \mu\text{m}$. No data have been collected to evaluate that effect.

5. DEVICE EVALUATION

The objectives of the device evaluation portion of this program are (a) to utilize the fabricated waveguide structures to demonstrate integrated optical devices, (b) to provide theoretical guidance so that waveguide structures could be modified to optimize the device performance, and (c) to develop techniques and devices for making effective evaluations. Therefore the major objective of the device evaluation at $10.6\ \mu\text{m}$ wavelength is to investigate electrooptical modulation. The major objectives of the very limited amount of work on device evaluation in the near infrared are to develop effective input and output couplers and to initiate the investigation of fiber to film coupling.

5.1 Electrooptical Modulation at $10.6\ \mu\text{m}$ Wavelength

The investigation of electrooptical modulation began with a theoretical calculation of the uniform thin film (i.e. planar) waveguide modulator. From this calculation we determined the best waveguide structure, the necessary length of the modulator, and the r.f. power requirement for such a modulator. It led us to the fabrication of large area waveguides, emphasis on the GaAs/GaAs_{1-x}P_x waveguide, and a search for high resistivity film as discussed in Section 2. In order to confirm the calculated results before the experimental realization of good GaAs/GaAs_{1-x}P_x waveguides, an experimental modulator was fabricated on a GaAs/n⁺GaAs waveguide. This experimental modulator performed poorly but its result confirmed the theoretical prediction. Subsequently a theoretical investigation was undertaken to analyze the two dimensional waveguide modulator. The results of this evaluation showed that the r.f. power

requirement can be reduced and the r.f. impedance can be raised without significantly reducing the modulation efficiency for a given applied voltage and modulator length. This result prompted us to develop the two dimensional waveguide discussed in Section 4.2. Experimental fabrication of a two dimensional waveguide modulator on a GaAs/GaAs_{1-x}P_x waveguide was initiated during the final contract period, but no experimental result is available yet.

Most of the theoretical analysis was carried out under NSF Grant GK 31854. The experimental investigation of two dimensional waveguide is currently being continued beyond the contract period of this program under the sponsorship of Washington University and the NSF grant.

5.1.1 Theoretical Calculation

The voltage, V, and the power, P, required for bulk GaAs or CdTe electrooptical phase modulators are:^(11, 12)

$$V = (2\Delta\phi/k_0 n^3 r_{41}) (d/\ell) \quad (1)$$

$$P/\Delta f = \frac{\epsilon_r}{72} \left(\frac{\lambda_0}{n^3 r_{41}} \right)^2 \frac{Wd}{\ell} \quad (2)$$

where $\Delta\phi$ = phase shift required

k_0 = propagation wavenumber in free space = $2\pi/\lambda_0$

n = refractive index

r_{41} = electrooptical coefficient

d = thickness of the modulator across which the voltage is applied

ℓ = length of the modulator

W = width of the modulator

ϵ_r = relative dielectric constant at the r.f. frequency

Δf = r.f. bandwidth desired

λ_0 = free space wavelength

A similar expression can be given for polarization modulators. Because of the long wavelength and because of the diffraction limitations on both the (d/ℓ) and the (W/ℓ) ratio, electrooptical modulators are known to perform very poorly in the far infrared. A substantial improvement in performance can be achieved through the use of thin-film waveguide modulators since the (d/ℓ) ratio is not subject to the diffraction limitation in waveguides (13-16). Since the substrate of all our waveguide structures has a higher free carrier concentration than the film, it is most advantageous to apply the modulation voltage across the structure at UHF and VHF frequencies. Very little voltage drop will occur across the substrate. Most of the voltage will appear across the thin film, thereby obtaining a very small (d/ℓ) ratio. It is necessary, however, to avoid depositing the electrodes directly on the film because they will cause high attenuation. Therefore, the analysis presented here will be concerned with guided wave modulators that have a buffer film, with $n_f > n_s$ and n_b . Moreover, our analysis will assume that the GaAs epitaxial film can be compensated during the epitaxial growth process to obtain a very high resistivity so that r. f. heating effects can be neglected. In practice, this is difficult to achieve; alternatively, the high resistivity layer in the film may be achieved by p-diffusion and by reverse biasing the resulting p-n junction. A detailed (and complicated) analysis based on the alternative structure is given in reference 17. Since the results obtained for the alternative structure with the p-n junction are very similar to those presented here, they will not be given in this report.

5.1.1.1 Phase Modulation in Uniform Thin-Film Waveguides

The guided wave modes of the waveguide structure are well known.

The electric field for a TE_m mode with no transverse variation and

$j\omega t$ variation is

$$\underline{E}_m(x, z, t) = E_m(x) e^{-j\beta_m \cdot \underline{\zeta}} e^{j\omega_0 t} \underline{i}_\xi \quad (3)$$

$$E_m(x) = (B_m + C_m) \sin(h_m d_f + \phi_m) e^{-p_m(x - d_f - d_b)} \quad \text{for } x > d_f + d_b$$

$$E_m(x) = \{B_m \exp[q_m(d_f + d_b - x)] + C_m \exp[-q_m(d_f + d_b - x)]\} \sin(h_m d_f + \phi_m) \\ \text{for } d_f < x \leq d_f + d_b$$

$$E_m(x) = A_m \sin(h_m x + \phi_m) \quad \text{for } 0 < x < d_f \\ = A_m \sin \phi_m e^{\ell_m x} \quad \text{for } x < 0$$

where $\underline{\beta}_m = \beta_m \underline{i}_z$, $\underline{\zeta} = \zeta \cos \theta \underline{i}_z + \zeta \sin \theta \underline{i}_y$

$$n_b \text{ or } n_s < \beta_m/k_0 < n_f \\ -p_m^2 + \beta_m^2 = n_0^2 k_0^2, \quad -q_m^2 + \beta_m^2 = n_b^2 k_0^2, \quad h_m^2 + \beta_m^2 = n_f^2 k_0^2, \quad -\ell_m^2 + \beta_m^2 = n_s^2 k_0^2 \quad (4)$$

β_m , h_m , q_m , and p_m are m th roots of the equation

$$\tan(h_m d_f) = - \frac{h_m}{q_m \ell_m} \frac{q_m + \ell_m \tanh(q_m d_b + \theta_m)}{1 - \frac{h_m}{q_m \ell_m} \tanh(q_m d_b + \theta_m)} \quad (5)$$

$$\tanh \theta_m = \frac{q_m}{p_m}$$

E_m is normalized so that

$$\frac{1}{2} \operatorname{Re} \int_{-\infty}^{+\infty} \{ [\underline{E}_m \times \underline{H}_m^*] \cdot \underline{i}_z \} dx = \frac{\beta_m}{2\omega\mu_0} \int_{-\infty}^{+\infty} E_m E_m^* dx = \delta_{mn} \quad (6)$$

where μ_0 is the free space permeability.

The effect of an applied voltage across the high resistivity GaAs layer is to produce a change of refractive index $\Delta n^2(x,t) = \Delta n_p^2(x) \cos \omega_m t$ where

$$\Delta n_p^2 = -n_f^4 r_{41} V/d_f \quad (7)$$

From perturbation analysis (17, 18) the change in the propagation constant β_m caused by this Δn^2 is found to be

$$\Delta \beta_m = \frac{k_0^2}{2\beta_m} \left[\frac{\beta_m}{2\omega\mu} \int_0^{d_f} F_m \Delta n_p^2 E_m^* dx \right] \cos \omega_m t \quad (8)$$

where the quantity in the bracket is commonly known as the overlap integral. Thus the resultant phase modulation for the TE_m mode is

$$\Delta \phi = \ell \Delta \beta_m = C_{mm} V \ell \cos \omega_m t \quad (9)$$

where

$$C_{mm} = \frac{k_0^2 n_f^4 r_{41}}{2\beta_m d_f} \left[\frac{\beta_m}{2\omega\mu_0} \int_0^{d_f} E_m E_m^* dx \right]$$

For π -phase modulation the required voltage is

$$V_\pi = \pi / C_{mm} \ell \quad (10)$$

Since the r.f. capacitance of the modulating electrode is $\epsilon_r W \ell \epsilon_0 / d_f$, the required r.f. power per unit bandwidth for π -phase shift is

$$\left(\frac{P}{\Delta f} \right)_{\text{phase}} = \frac{\epsilon_r}{72} \left(\frac{\lambda_0}{n_f^3 r_{41}} \right)^2 \left(\frac{\beta_m}{n_f k_0} \right)^2 \left(\frac{W d_f}{\ell} \right) \left/ \left[\frac{\beta_m}{2\omega\mu_0} \int_0^{d_f} E_m E_m^* dx \right]^2 \right. \quad (11)$$

Figure 31 shows the calculated values of $C_{mm} V \ell / 2\pi$ and $\Delta \phi$ for the TE_0 mode as a function of d_f for $n_s = n_b = 3.16$ and for $n_s = n_b = 3.22$ at $V \ell = 3$ M-V. Figure 32 shows the corresponding calculated values of $P/\Delta f$ for $W/\ell = 0.05$. Note that there is an optimum value

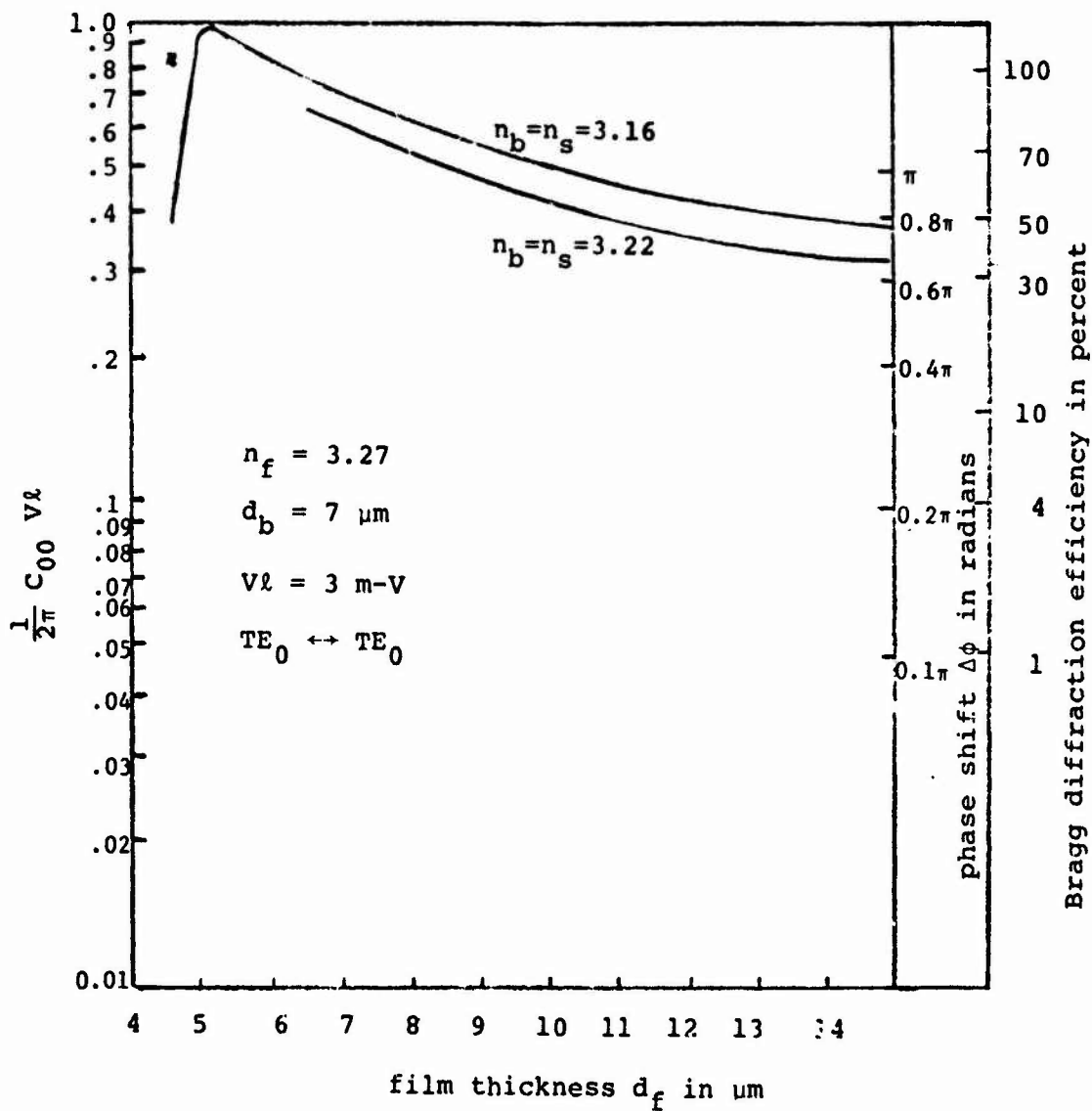


Fig. 31: Modulation Efficiency of Uniform Thin Film Guided Wave Modulators

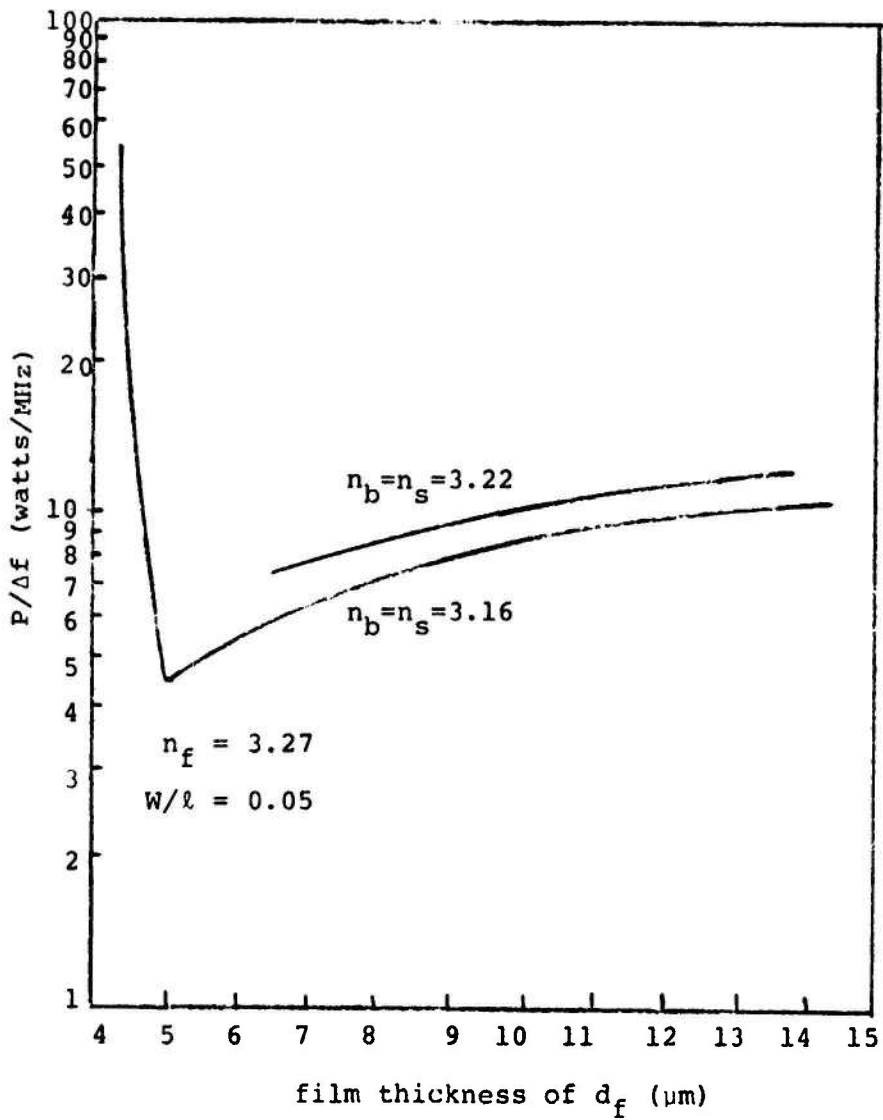


Fig. 32: The Power per unit Bandwidth Required for Uniform Thin Film Waveguide Modulators

of d_f that will minimize the required voltage for a given phase shift $\Delta\phi$. The physical reason for the existence of the optimum film thickness can be given as follows. For large d_f values, a decrease in film thickness will yield a larger $\Delta\phi$ because the r.f. electric field strength is larger for a given applied voltage V . But when the film thickness is close to the cut-off thickness of the TE_m mode, any further decrease of d_f will rapidly reduce the fraction of the optical power carried in the high resistivity thin film. This fraction is expressed as the overlap integral given in the bracket of the formula for C_{mm} . Since the Δn exists only in the high resistivity film, there will be a net reduction in $\Delta\phi$ if the film thickness is less than the optimum value. Curves for other $V\ell$ values can be obtained very simply by multiplying the curves in Figure 30 by the ratio of the $V\ell$ values. V will be limited eventually by the breakdown field strength of GaAs, typically about 100 Volts for a high resistivity layer a few microns thick. Thus modulators several centimeters in length are necessary to obtain large amounts of phase modulation. On the other hand, the power per unit bandwidth depends linearly on the W/ℓ ratio. This ratio is still restricted by the diffraction limited beam divergence in the horizontal plane.

It has been shown in the bulk modulator and is true here as well that the minimum W/ℓ ratio is (11)

$$\frac{W^2}{\ell} = (S^2) \frac{8}{\beta_m}$$

where S is a safety factor. Thus the lowest $P/\Delta f$ that one can expect to get for $\ell = 5$ cm, $d_f = 5$ μ m, $W = 1$ mm, and $n_s = 3.16$ is 1.5 watts per megahertz.

5.1.1.2 Amplitude Modulation in Uniform Thin Film Waveguides

In thin-film waveguides, it is difficult to excite both the TE and the TM modes efficiently at the same time so as to obtain polarization modulation. Bragg diffraction, beam steering, or mode conversion are used to achieve amplitude modulation. Of these, the mode conversion process is inefficient because of the low coupling efficiency that can be achieved with the small overlap integral value⁽¹²⁾. Therefore, only the analysis for amplitude modulation based upon Bragg diffraction^(12, 19, 20) and beam steering⁽¹⁵⁾ is presented here.

The periodic variation of Δn needed for Bragg diffraction can be obtained by depositing on the buffer film an electrode that has fingers of width, a , and periodicity, L , along the z direction. If L is larger than $d_b + d_f$, the electrode will create a rectangular periodic variation of Δn^2 in the y direction which can be represented by a Fourier Series

$$\Delta n^2 = - (n_f^4 r_{41} V/d_f) \cos \omega_m t \sum_{p=-\infty}^{+\infty} \frac{\sin(p\pi a/L)}{p\pi} e^{-j2\pi p y/L} \quad (12)$$

For an incident TE_m mode propagating in the \underline{z} direction and a diffracted TE_n mode propagating in the \underline{z}' direction the Bragg condition is

$$\underline{\beta}_m = \underline{\beta}_n \pm p\underline{K} \quad (13)$$

where $\underline{K} = \frac{2\pi}{L} \underline{i}_y$. Since the largest Fourier coefficient is that for $p = \pm 1$, we shall only present here the calculated results for first order diffraction. Moreover, since β_m and β_n are much larger than $2\pi/L$, we shall assume that $\sin \psi \cong 0$ and $\cos \psi \cong 1$ where ψ is the angle between the \underline{z} and \underline{z}' directions.

The analytical method most appropriate for the determination of the amplitude of the incident and diffracted beam is clearly the coupled mode analysis where Δn^2 is treated as a perturbation to the waveguide. The wave equation including the effects of the electrooptical perturbation is

$$\nabla \times \nabla \times \underline{E} - k_0^2 n^2(x) \underline{E} = -k_0^2 \Delta n^2 \underline{E} [u(x-0) - u(x-d_f)] \quad (14)$$

Standard methods are used to transform this equation into a coupled mode equation where \underline{E} is the summation of the modes propagating in the ζ and ζ' directions and Δn^2 provides the coupling between them. The scattered beam in the ζ' direction will be shifted in frequency from the ω_0 of the incident beam to a frequency $\omega_0 \pm \omega_M$. The reverse scattering of this beam into the ζ direction by the time varying Δn^2 will yield frequency components at ω_0 and $\omega_0 \pm 2\omega_M$. Consequently, there will be frequency components of $\omega_0 + \ell\omega_M$ in the ζ direction, $\ell = 0, \pm 2, \pm 4, \dots$. Similarly, there will be frequency component of $\omega_0 \pm s\omega_M$ in the ζ' direction where $s = \pm 1, \pm 3, \pm 5, \dots$. Thus, we expect the solution of Equation (13) to be of the form

$$\begin{aligned} \underline{E} = & \sum_{\ell} E_m(x) V_{\ell}(z) \exp[j(\omega_0 + \ell\omega_M)t - j\beta_m \zeta] \underline{i}_{\xi} \\ & + \sum_{\ell} E_n(x) U_{\ell}(z) \exp[j(\omega_0 + \ell\omega_M)t - j\beta_n \zeta'] \underline{i}_{\xi}, \end{aligned} \quad (15)$$

where other nonphase-matched terms and the terms involving $\sin\psi$ have been neglected; and where $V_{\ell} = 0$ for odd ℓ and $U_{\ell} = 0$ for even ℓ . Substituting Equation (15) into Equation (14), assuming that $E_m(x)$ and $E_n(x)$ are equal for all values of ℓ that have practical interest, equating terms that have the same temporal and spatial

variation, and finally taking advantage of the orthogonality of the modes, we have

$$\frac{\partial U_\ell}{\partial z} = \frac{1}{2} j C_\ell V (V_{\ell-1} + V_{\ell+1}) \quad (16)$$

$$\frac{\partial V_\ell}{\partial z} = \frac{1}{2} j C_\ell V (U_{\ell-1} + U_{\ell+1})$$

where

$$C_\ell = \frac{k_0^2}{2\beta_m} \left[\frac{\beta_m}{2\omega_0 \mu} \int_0^{d_f} E_m E_n^* dx \right] (n_f^4 r_{41} / d_f) [\sin(\pi a / L) / \pi]$$

The solution of Equation (15) is:

$$\begin{aligned} V_\ell &= j^\ell V_0 J_\ell (C_\ell z) && \text{for even } \ell \\ U_\ell &= j^\ell V_0 J_\ell (C_\ell z) && \text{for odd } \ell \end{aligned} \quad (17)$$

where J_ℓ is the ℓ th order Bessel function; the length of the electrode is z ; and V_0 is the amplitude of the incident wave at $z = 0$. For $\omega_M \ll \omega_0$, Equation (15) can be simplified; and we obtain

$$\begin{aligned} E_R &= \sum_\ell E_m(x) V_\ell(y, z) \exp[j(\omega_0 + \ell\omega_M)t - j\beta_m z] \\ &\approx \sum E_m(x) e^{j(\omega_0 t - \beta_m z)} \cos[C_\ell z \cos\omega_M t] \end{aligned} \quad (18a)$$

Similarly

$$\begin{aligned} E_S &= \sum_\ell E_n(x) U_\ell(y, z) \exp[j(\omega_0 + \ell\omega_M)t - j\beta_n z] \\ &\approx \sum E_n(x) e^{j(\omega_0 t - \beta_n z)} \sin[C_\ell z \cos\omega_M t] \end{aligned} \quad (18b)$$

C_ℓ is small unless $m = n$. Hence, we shall only present here the numerical results for Bragg modulation where $m = n$ and $L = 2a$. In that case,

$$C_\ell = C_{mm} / \pi \quad (19)$$

In other words, the numerical calculation of the C_{mm} coefficients for the phase modulator in Figure 31 is directly applicable to amplitude modulation. The Bragg modulation efficiency is clearly $\sin^2(C_{mm} Vz/\pi)$. Hence, the C_{mm} curves given in Figure 31 are also used to present the Bragg modulation efficiency, where the scale on the right-hand margin is nonlinear and is made to fit the functional relationship of $\sin^2(\frac{1}{\pi} C_{mm} V)$. A comparable figure of merit to V_{π} is V_{100} , the voltage needed to obtain 100% amplitude modulation. Clearly,

$$V_{100} = \pi^2 / (2C_{mm}) = V_{\pi} (\pi/2) \quad (20)$$

Since $a/L = \frac{1}{2}$, the r.f. capacitance of the electrode is only half as large as the capacitance for the phase modulator. Thus the power per unit bandwidth for 100% amplitude modulation is:

$$(P/\Delta f)_{amp} = (P/\Delta f)_{phase} \left(\frac{\pi^2}{8}\right) \quad (21)$$

Hence, the $(P/\Delta f)_{phase}$ Bragg curves shown in Figure 31 are applicable to amplitude modulation as well.

Cheo has reported that if a guided wave is propagated along the edge of an electrode (i.e., with part of the beam under the electrode and part of the beam outside the electrode), the phase shift caused by the electrooptical effect on half of the beam will interfere with the other half of the unperturbed beam⁽¹⁵⁾. The shift in the angular direction of the beam, $\Delta\psi$, is related to the phase shift of the phase modulator by

$$\Delta\psi = \Delta\phi / k_0 W \quad (22)$$

The amount of $\Delta\phi$ needed to resolve the shifted beam completely from the original beam is $\Delta\phi = \pi$. Hence the results presented for V_{π} and $P/\Delta f$ in phase modulation are also applicable to the case of beam steering.

5.1.1.3 Electrooptical Modulation in Two-dimensional Waveguides

It is clear from Equations (1) and (9) that the modulator has achieved its best performance in terms of modulation voltages, when a waveguide with optimum d_f is used. Even then the large r.f. capacitance causes the uniform thin-film waveguide modulation to have low impedance and a large $P/\Delta f$ requirement. From Equation (11) it is clear that the reduction of $P/\Delta f$ is constrained by limitation of the (W/l) ratio. If two-dimensional (or channel) waveguides are used in place of the uniform thin-film waveguide, the very small W/l ratio that becomes possible can now be used to reduce the capacitance and the $P/\Delta f$ ratio. The minimum value of W will eventually be limited by the maximum optical power that must be transmitted in the modulator. The maximum value of l will eventually be limited both by the length of the available epitaxial waveguides (about 3 inches) and by the transit time limitation imposed by the maximum modulation frequency. For example, for microwave modulation of CO_2 laser radiation, traveling wave interaction is necessary.

High-performance etched two-dimensional GaAs waveguide has already been discussed in Section 4.2. The modes of the two-dimensional waveguides are also well known. Roughly speaking, the lowest E_{pq}^y and E_{pq}^x modes well above cutoff can be represented as TE_m or TM_m ($m = p - 1$) modes of the uniform thin-film waveguide totally internally reflected back and forth between the two side walls^(18, 21). Figure 33 is an illustration of this representation in which each mode is represented by a $\underline{\beta}$ vector of the TE_m or TM_m mode at a specific direction of propagation

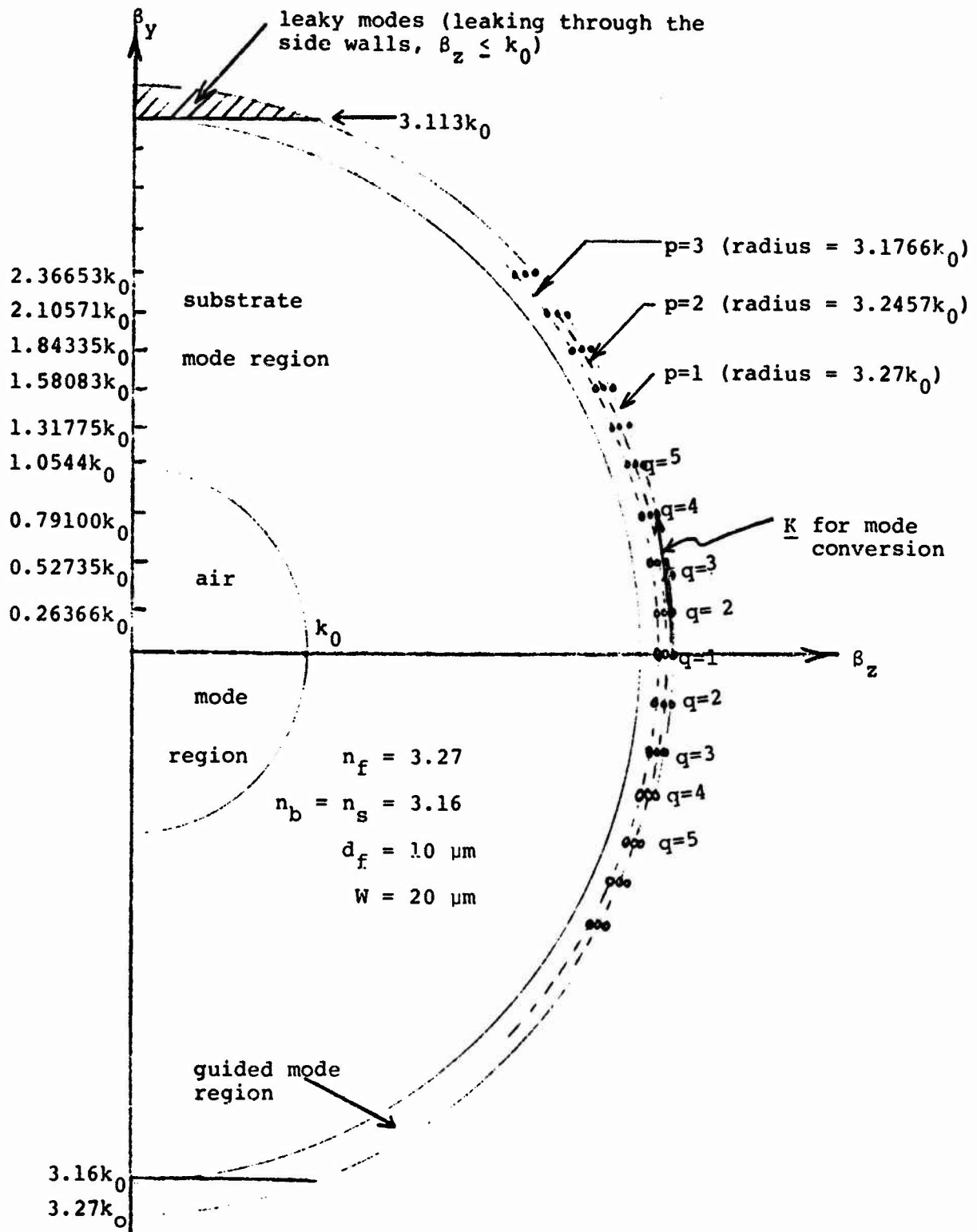


Fig 33: The Equivalent β_y and β_z Representing Propagating Modes in Two-Dimension Waveguides

in the horizontal plane that gives a phase shift of $2q\pi$ per round trip horizontal reflection. Because of the complexity of the mathematics, readers are referred to reference (21) for general analytical expressions of modes in two-dimensional waveguides and to reference (17) for the analytical expression of the specific modes of the GaAs waveguide. Using E_{pq}^y modes as examples, we shall simply write in this report.

$$\begin{aligned}
 E_x &= E_{xx}(x)E_{xy}(y)e^{-j\beta_z z} & H_x &= H_{xx}(x)H_{xy}(y)e^{-j\beta_z z} \\
 E_y &= E_{yx}(x)E_{yy}(y)e^{-j\beta_z z} & H_y &= 0 \\
 E_z &= E_{zx}(x)E_{zy}(y)e^{-j\beta_z z} & H_z &= H_{zx}(x)H_{zy}(y)e^{-j\beta_z z}
 \end{aligned} \tag{23}$$

where, inside the waveguide $\beta_y^2 + \beta_z^2 = \beta_{p-1}^2$, $\beta_x^2 = n_f^2 k_0^2 - \beta_{p-1}^2$

Phase modulation is conceptually simple. A change in the refractive index caused by an applied voltage across the thickness of the waveguide will produce a change in phase,

$$\Delta\phi = \ell\Delta\beta_z \tag{24}$$

$\Delta\beta_z$ can again be calculated by perturbation analysis to be

$$\Delta\beta_z = C_{pq,pq} V \cos\omega_M t \tag{25}$$

$$\begin{aligned}
 C_{pq,pq} &= \left\{ \left(k_0^2 n_f^4 r_{41} / \beta_z d_f \right) / \left[1 + \frac{n_f^2 k_0^2 (n_f^2 k_0^2 - \beta_z^2)}{\beta_y^2 \beta_z^2 + n_f^2 k_0^2 \beta_x^2} \right] \right\} \times \\
 &\left[\frac{\omega_0 \epsilon_0 n_f^2 \beta_z (n_f^2 k_0^2 - \beta_z^2)}{2(\beta_y^2 \beta_z^2 + n_f^2 k_0^2 \beta_x^2)} \int_0^{d_f} E_{yx}(\beta_x x) E_{yx}^*(\beta_x x) dx \int_{-W/2}^{+W/2} E_{yy}(\beta_y y) E_{yy}^*(\beta_y y) dy \right]
 \end{aligned}$$

From this expression of $\Delta\beta_z$, we obtain, similar to Equation (11), the power per unit bandwidth for π -phase modulation as

$$\begin{aligned} \frac{(P/\Delta f)}{\text{phase}} &= \frac{\epsilon_r}{288} \left(\frac{\lambda_0}{n_f r_{41}} \right)^2 \left(\frac{\beta_z}{n_f k_0} \right)^2 \left(\frac{W d_f}{\ell} \right) \left[1 + \frac{n_f^2 k_0^2 (n_f^2 k_0^2 - \beta_z^2)}{\beta_y^2 \beta_z^2 + n_f^2 k_0^2 \beta_x^2} \right]^2 / \\ &\left[\frac{\omega_0 \epsilon_0 n_f^2 \beta_z (n_f^2 k_0^2 - \beta_z^2)}{2(\beta_y^2 \beta_z^2 + n_f^2 k_0^2 \beta_x^2)} \int_0^{d_f} |E_{YX}(\beta_x x)|^2 dx \int_{-W/2}^{+W/2} |E_{YY}(\beta_y y)|^2 dy \right] \end{aligned} \quad (26)$$

The results expressed in both Equations (25) and (26) reduce directly the results given in Equations (8) and (11) in the limit large W , $W n_f / \lambda_0 \gg 1$, so that $\beta_y \cong 0$ and $\beta_z \cong \beta_m$. Figure 34 shows the curves of the calculated $\frac{1}{2\pi} C_{pq,pq} V\ell$ value and $\Delta\phi$ versus the thickness d_f for $W = 20 \mu\text{m}$ and $50 \mu\text{m}$ and for $n_s = n_f = 3.16$ and 3.22 at $V\ell = 3 \text{ m-V}$. Figure 35 shows the corresponding curves of $P/\Delta f$ for $W/\ell = 0.002$. Curves for other $V\ell$ products and for other W/ℓ ratios can be obtained directly from these two figures by multiplying the $C_{pq,pq}$ coefficient or the $P/\Delta f$ by the ratio of $V\ell/3$ or by the ratio of $(W/\ell)/0.002$. Note that the C coefficients are only slightly smaller than those for the dimensional waveguide and are relatively independent of W and q values because the selected W values are already fairly large compared to λ_0/n_f . Large W values are chosen because experiments performed with a high power CO_2 laser showed that intrinsic GaAs windows cooled at the edges could tolerate a power density of 40 KW/cm^2 without any sign of thermal runaway (22). This implies an estimated transmitted laser power of 40 mW for $20\text{-}\mu\text{m}$ wide guide and 100 mW for $50\text{-}\mu\text{m}$ wide guide. The estimate is probably very conservative because much better heat sinking could be provided for waveguides than for laser windows.

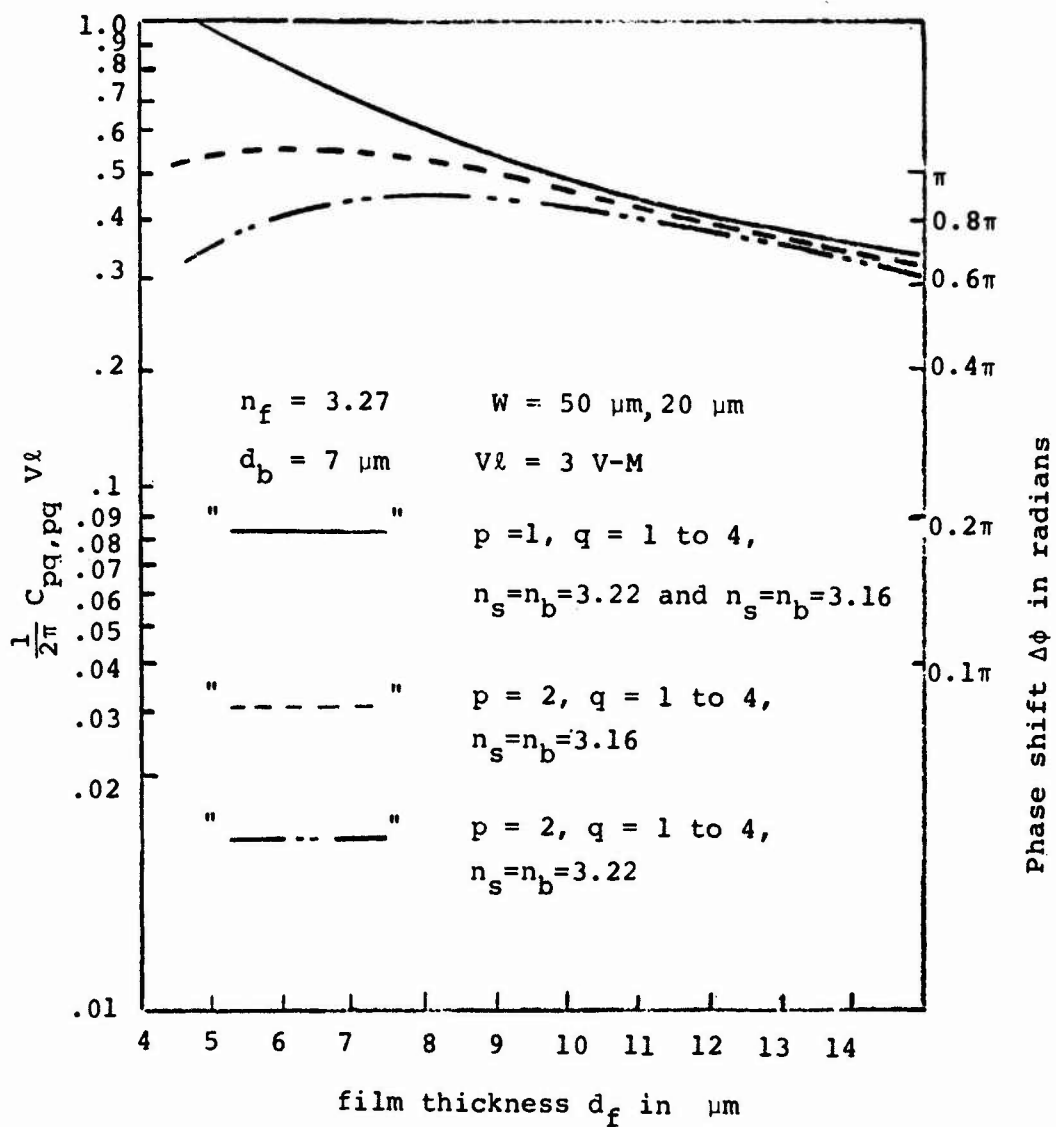


Fig. 34: Efficiency of Two-Dimensional Waveguide Phase Modulator

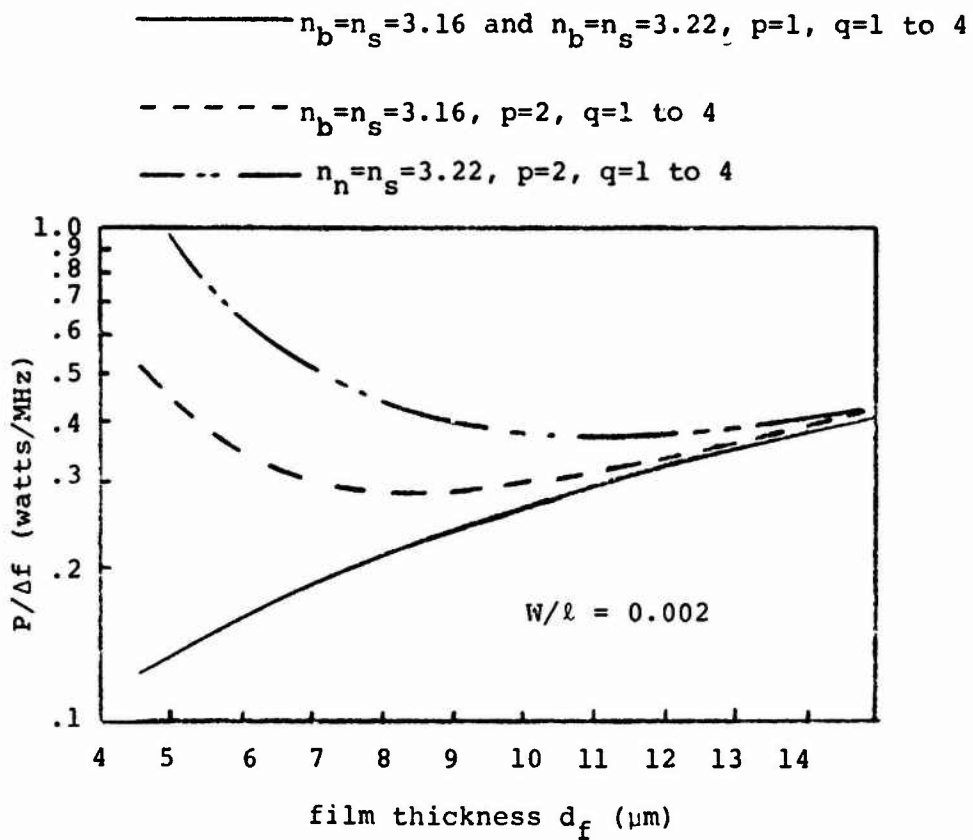


Fig. 35: The Power Per Unit Bandwidth Required
 for Two-Dimensional Waveguide Phase
 Modulators.

Large W values also give a low attenuation rate, which is important for modulators several centimeters long. Figures 34 and 35 demonstrate that $P/\Delta f$ in the range of one hundred milliwatts per megahertz is realistic for two-dimensional waveguide modulators.

For amplitude modulation, it is necessary to convert the laser power in the incident E_{pq}^Y and E_{pq}^X mode to another $E_{p'q'}^Y$ or $E_{p'q'}^X$ mode. E_{pq}^Y and $E_{p'q'}^Y$ modes will couple out of the thin-film waveguide in different directions; thus mode conversion is equivalent to amplitude modulation. Mode conversion can be accomplished by a periodic change of refractive index that will have a \underline{K} vector phase matching the two equivalent $\underline{\beta}$ vectors for the two modes as shown in Figure 33. For example, the \underline{K} vector of the periodic electrode needed to convert E_{12}^Y to E_{14}^Y and E_{21}^Y to E_{23}^Y modes as illustrated in Figure 33. An illustration of a periodic electrode that will give the necessary \underline{K} vectors is shown in Figure 36. For such an electrode, the Δn^2 created by the electrooptical effect may be given in the first order approximation as

$$\Delta n^2 = -(4n_f^4 r_{41} V/d_f) \cos \omega_M t \frac{\sin(\pi a_y/L_y)}{\pi} \frac{\sin(\pi a_z/L_z)}{\pi} \times [\cos(2\pi y/L_y) + \theta_y] \cos[(2\pi z/L_z) + \theta_z] \quad (27)$$

$$-W/2 \leq y \leq +W/2$$

$$0 \leq z \leq \ell$$

$$\frac{2\pi}{L_y} = |(\beta_y)_{pq} - (\beta_y)_{p'q'}|, \quad \frac{2\pi}{L_z} = |(\beta_z)_{pq} - (\beta_z)_{p'q'}|$$

where L_y and L_z are the period in the y and z directions, respectively; a_y and a_z are the width of the electrode stripes in the y and z

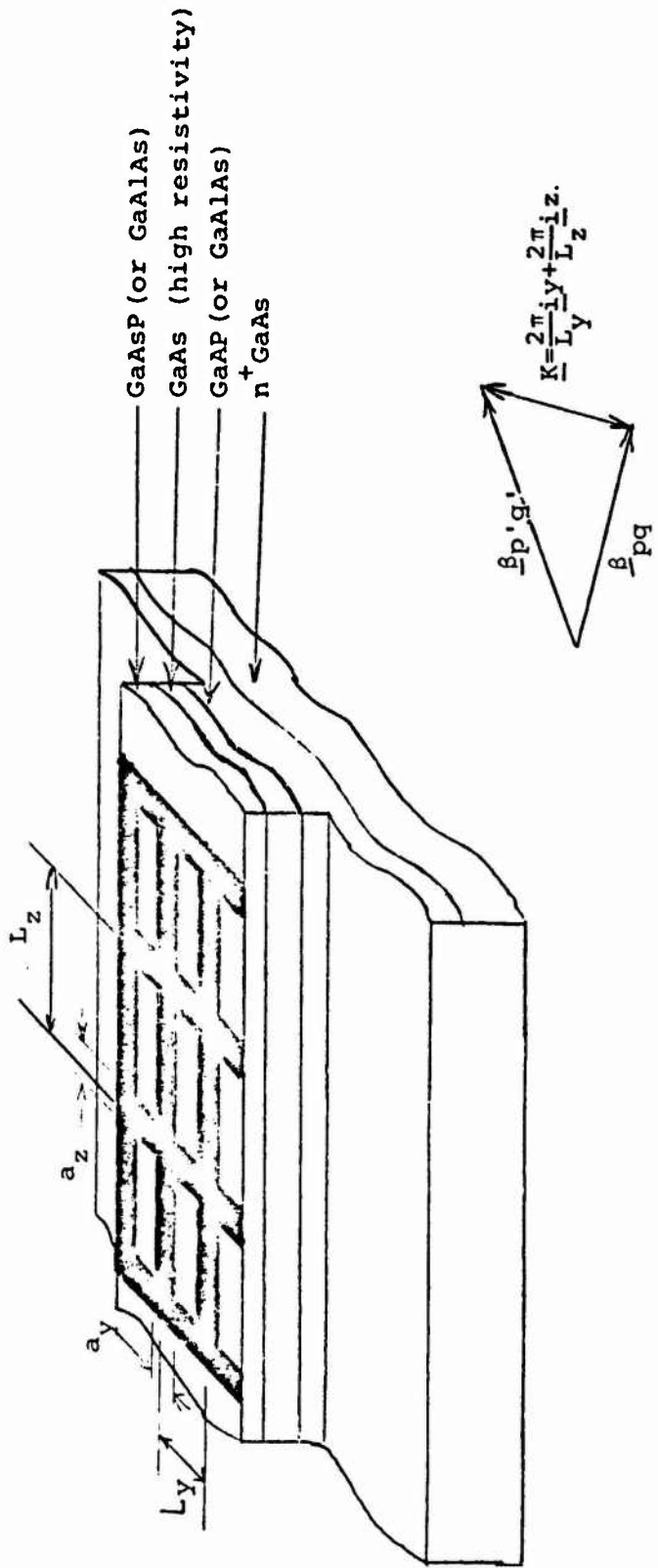


Figure 36: Illustration of Amplitude Modulation in Two Dimensional Waveguides

directions; and θ_y and θ_z are determined by the relative position of the electrode finger with respect to the waveguide axis (e.g., $\theta_y = 0$ for electrode pattern symmetric with respect to $y = 0$ axis).

The analysis of the E_{pq}^y and $E_{p'q'}^y$ modes that are coupled and phase matched by the Δn^2 can be handled in the same manner as the analysis for Equation (14). Hence only the results and not the details of that analysis will be given here. Note that there will be an additional overlap integral in the y coordinate. E_{pq}^y is either an even or an odd function of y depending on whether $q-1$ is an even or an odd integer. Hence the overlap integral in y is maximized for $\Delta q = q' - q$ even with $\theta_y = 0$, and it is maximized for $\Delta q = q' - q$ odd with $\theta_y = \pi/2$. The overlap integral in x is very small unless $p = p'$. Therefore, electrode patterns, such as those shown in Figure 36 must be either symmetric ($\theta_y = 0$) or antisymmetric ($\theta_y = \pi/2$) with respect to the waveguide axis. For the most efficient cases where $p = p'$ and for $\omega_M \ll \omega_0$, the amplitudes of the incident mode, R , and converted mode, S , are

$$R = \cos \left[\frac{1}{\pi} C_{pq,pq} \sqrt{L} \cos \omega_M t \right] \quad (28)$$

$$S = \sin \left[\frac{1}{\pi} C_{pq,pq} \sqrt{L} \cos \omega_M t \right]$$

$$C_{pq,pq} = \left\{ (2k_0^2 n_f^4 r_{41} / \pi \beta_z d_f) / \left[1 + \frac{n_f^2 k_0^2 (n_f^2 k_0^2 - \beta_z^2)}{\beta_y^2 \beta_z^2 + n_f^2 k_0^2 \beta_x^2} \right] \right\}$$

$$\cdot \left[\frac{\omega_0 \epsilon_0 n_f^2 \beta_z (n_f^2 k_0^2 - \beta_z^2)}{2(\beta_y^2 \beta_z^2 + n_f^2 k_0^2 \beta_x^2)} \int_{-W/2}^{+W/2} E_{yy}(\beta_y y) \cos \left(\frac{2\pi y}{L_y} + \theta_y \right) E_{yy}'(\beta'_y y) dy \right. \\ \left. \int_0^{d_f} E_{yx}^2(\beta_x x) dx \right]$$

where $\theta_y = 0$ for Δq even and $\theta_y = \pi/2$ for Δq odd. For 100% mode conversion, the power per unit bandwidth is

$$P/\Delta f = \frac{\pi^4/32}{72} \epsilon_r \left(\frac{Wd_f}{\ell}\right) \left(\frac{\lambda_0}{n_f^3 r_{41}}\right)^2 \left(\frac{\beta_z}{n_f k_0}\right)^2 \left[1 + \frac{n_f^2 k_0^2 (n_f^2 k_0^2 - \beta_z^2)}{\beta_y^2 \beta_z^2 + n_f^2 k_0^2 \beta_x^2}\right]^2 /$$

$$\left[\frac{\omega_0 \epsilon_0 n_f^2 \beta_z (n_f^2 k_0^2 - \beta_z^2)}{(\beta_y^2 \beta_z^2 + n_f^2 k_0^2 \beta_x^2)} \int_{-W/2}^{+W/2} E_{YY}(\beta_y y) \cos\left(\frac{2\pi y}{L_y} + \theta_y\right) E_{YY}'(\beta_y' y) dy \int_0^{d_f} E_{YX}^2(\beta_x x) dx \right]^2 \quad (29)$$

The calculated value of $\frac{1}{2\pi} C_{pq,p'g'}$, $V\ell$ and mode conversion efficiency are shown again in Figure 37 as a function of the waveguide thickness for $V\ell = 3$ m-V. Notice that there is very little difference in their value whether W is 20 μm or 50 μm ; their values are also relatively independent of the mode order q' and p' as long as $p = p' = 1$. There is a significant reduction in their values when $p = p' = 2$ and when $n_f - n_s$ becomes smaller. The values of the coupling coefficients and efficiency are also very close to the corresponding values obtained for the uniform thin-film waveguides. Because the mode conversion efficiency is approximately independent of the width W and of the mode order q' , $P/\Delta f$ is presented in Figure 38 only with p' and with n_s as parameters. $P/\Delta f$ will vary linearly with respect to the W/ℓ ratio as long as $W > 20$ μm and $q' \leq 4$. The results presented in both Figure 37 and Figure 38 demonstrate that the use of two-dimensional waveguide (i.e., channel waveguide) reduces significantly the r.f. power required to drive the modulator without much reduction of modulation efficiency for a given $V\ell$ product, thickness d_f , and index difference $n_f - n_s$.

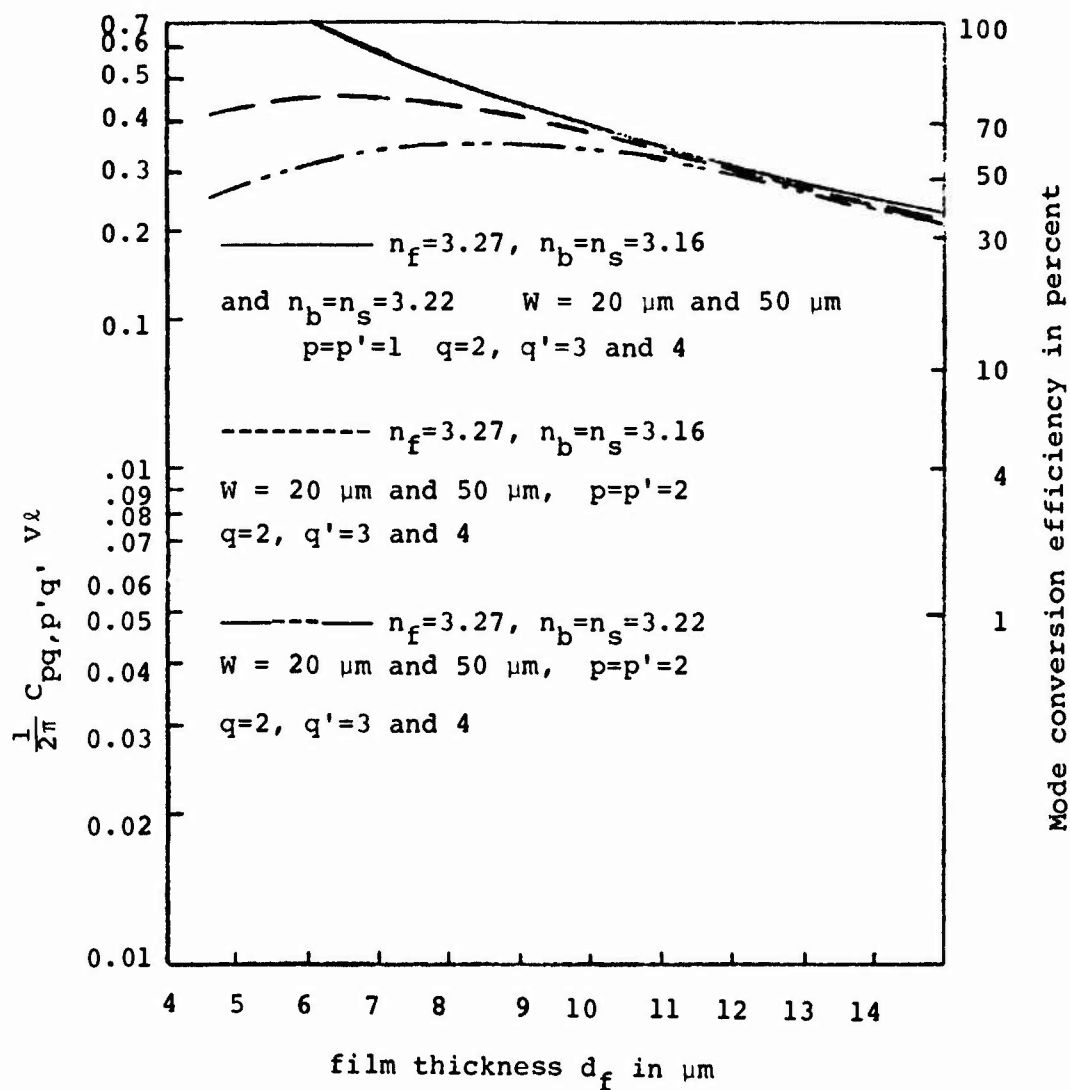


Fig. 37: Amplitude Modulation Efficiency of Two-Dimensional Thin Film Guided Wave Modulators

———— $n_b = n_s = 3.16$ and $n_b = n_s = 3.22, p' = p = 1,$

- - - - $n_b = n_s = 3.16, p' = p = 2,$

- · - · $n_b = n_s = 3.22, p' = p = 2,$

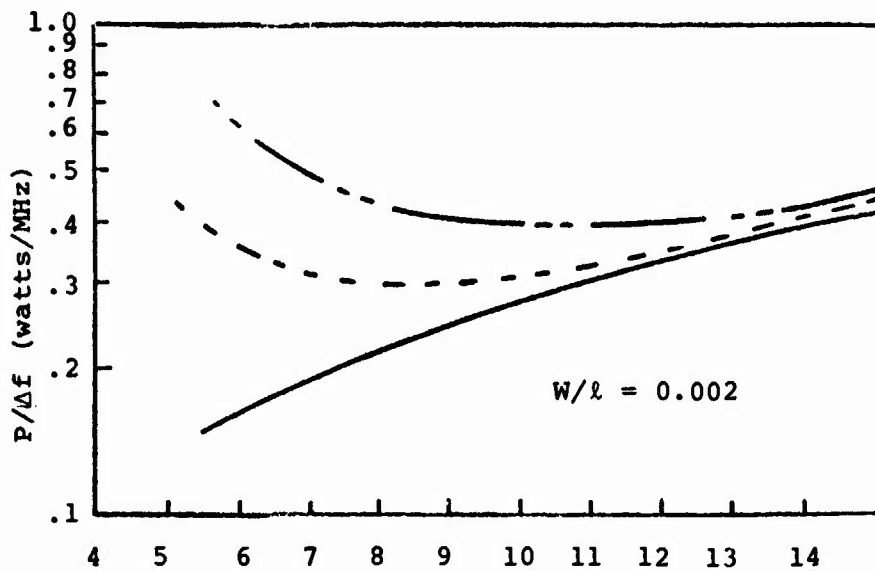


Fig. 38: The Power Per Unit Bandwidth Required for Two-Dimensional Waveguide Amplitude Modulators

The preceding results show that one could achieve 100% amplitude modulation or π -phase modulation in two-dimensional waveguides with $V\ell$ product of 3 m-V or more and at $d_f = 5$ or $6 \mu\text{m}$. The required $P/\Delta f$ is about 100 mW/MHz for W/ℓ less than 0.002. However, the power-carrying capacity of such modulators may be quite limited. Modulation at the same efficiency may be achieved in uniform thin-film waveguides at the same $V\ell$ product and the same thickness. An order of magnitude or more r.f. drive power is required; however, the uniform thin-film waveguide modulator can carry more CO_2 laser power. Although the formulas that have been derived for modulation efficiency and $P/\Delta f$ appear quite different for the uniform thin-film waveguide modulator and for the two-dimensional waveguide modulator, numerical results demonstrate that the simpler formula derived for the uniform thin-film waveguide modulator is a good approximation for the two-dimensional waveguide modulator with $W > 20 \mu\text{m}$.

A very important factor that must be considered in the fabrication of a waveguide modulator is its insertion loss. Our results demonstrate very clearly that it is necessary to use a long waveguide ($\ell > 3 \text{ cm}$) with a film thickness not too far from the cutoff thickness of the guided-wave mode ($d_f = 5$ to $7 \mu\text{m}$) in order to get efficient electrooptical modulation at $10.6 \mu\text{m}$. This means that the waveguide attenuation must be less than 1 dB/cm in order to get a total insertion loss less than 6 dB. The only material system that has been demonstrated today that may satisfy such an attenuation requirement is the GaAs/GaAsP waveguide grown by the vapor phase epitaxy technique.

5.1.2 Experimental Demonstration

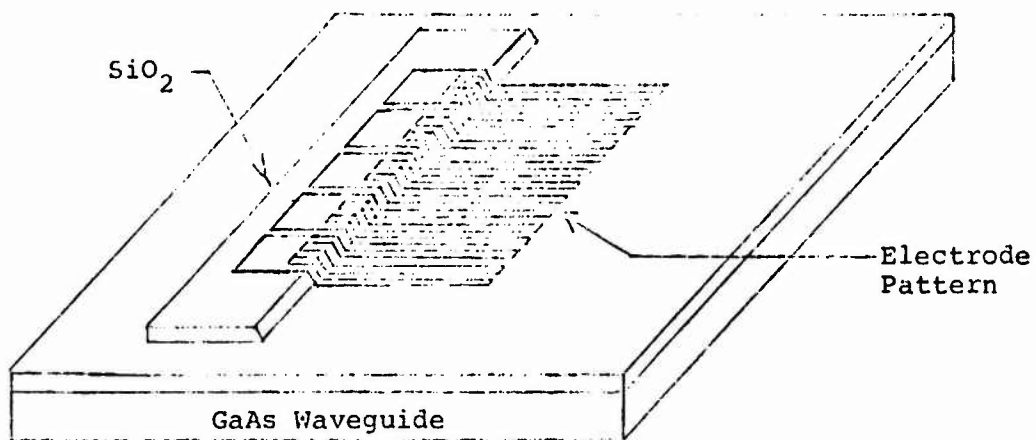
Initially, a mask consisting of grating fingers, 1 cm long, $31.8\ \mu\text{m}$ in periodicity, and $10.2\ \mu\text{m}$ wide was fabricated by the usual photolithography technique. This mask was used to fabricate an aluminum electrode pattern on a GaAs epitaxial waveguide by the photo-lift-off method (3). Because of the lack of high enough resistivity epitaxial film at the present time, it was decided that the best technique to obtain electrooptical deflection is to make the grating electrode into a Schottky barrier. If a d.c. reverse biased voltage is applied to the electrode, it would allow us to create the electrooptical effect without excessive modulation power dissipation in the waveguide. The total needed area of the Schottky barrier electrode is approximately $1/3\ \text{cm}^2$. With such a large area there is a high probability that some defects in the film or in the fabrication process will create localized high electric field regions. Because of these defects we were only able to get a reverse bias breakdown voltage of less than 15V in the first modulator fabricated, while small Schottky test barriers made on the same film showed a reverse bias breakdown voltage larger than 100V. With only 10V applied to the electrode, no modulation effects were observed in the first modulator.

To eliminate the difficulty caused by defects under a large Schottky barrier electrode, we redesigned the mask into groups of three individual grating fingers as shown in Figure 39 (a).

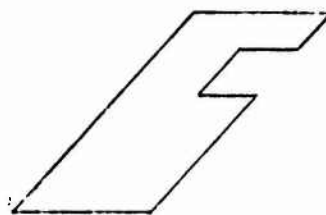
An SiO_2 layer was first deposited on a new piece of waveguide ($13.7\ \mu\text{m}$ thick GaAs on $n^+\text{GaAs}$ substrate). A set of aluminum grating



(a) The Electrode Mask



(b) The Electrode with SiO_2 Insulation



(c) The Interconnecting Electrode Mask

Figure 39 Illustration of the Fabrication Processes for Bragg's Modulation Electrode

electrodes shown in Figure 39 (b) was then made on top of the SiO_2 pattern and the GaAs by the lift-off method using the mask shown in Figure 39 (a). Each group of grating fingers was then tested electrically for its reverse breakdown individually. Less than 10% of the grating finger groups were found to have a low reverse breakdown voltage. These bad grating finger groups were marked, and an interconnecting mask as shown in Figure 39 (c) was made, designed specially to connect only the good grating finger groups to the applied modulation voltage. This mask was then used to fabricate an interconnecting electrode to connect just the good grating fingers. In this manner we avoided the defects that caused the low reverse breakdown voltage. The grating periodicity and the phase matching conditions will not be affected seriously by the omission of the bad grating fingers as long as the percentage of bad ones is small. The SiO_2 layer insures that no defect under the connecting electrode will cause a low reverse breakdown voltage. Figure 40 illustrates the completed electrooptical modulator. Figure 41 shows the microscopic photograph of the grating pattern, the SiO_2 pattern, and the interconnection electrode. A reverse bias voltage of over 70 volts was obtained in this modulator.

Subsequently, a guided wave was excited and detected by the prism input and output coupler. When the input prism is oriented in the direction that will launch an incident guided wave satisfying the Bragg's condition with the known periodicity and grating orientation of the electrode and when a reverse bias voltage is applied to the grating electrode, both a change in the propagation of the incident guided wave and a deflected guided wave

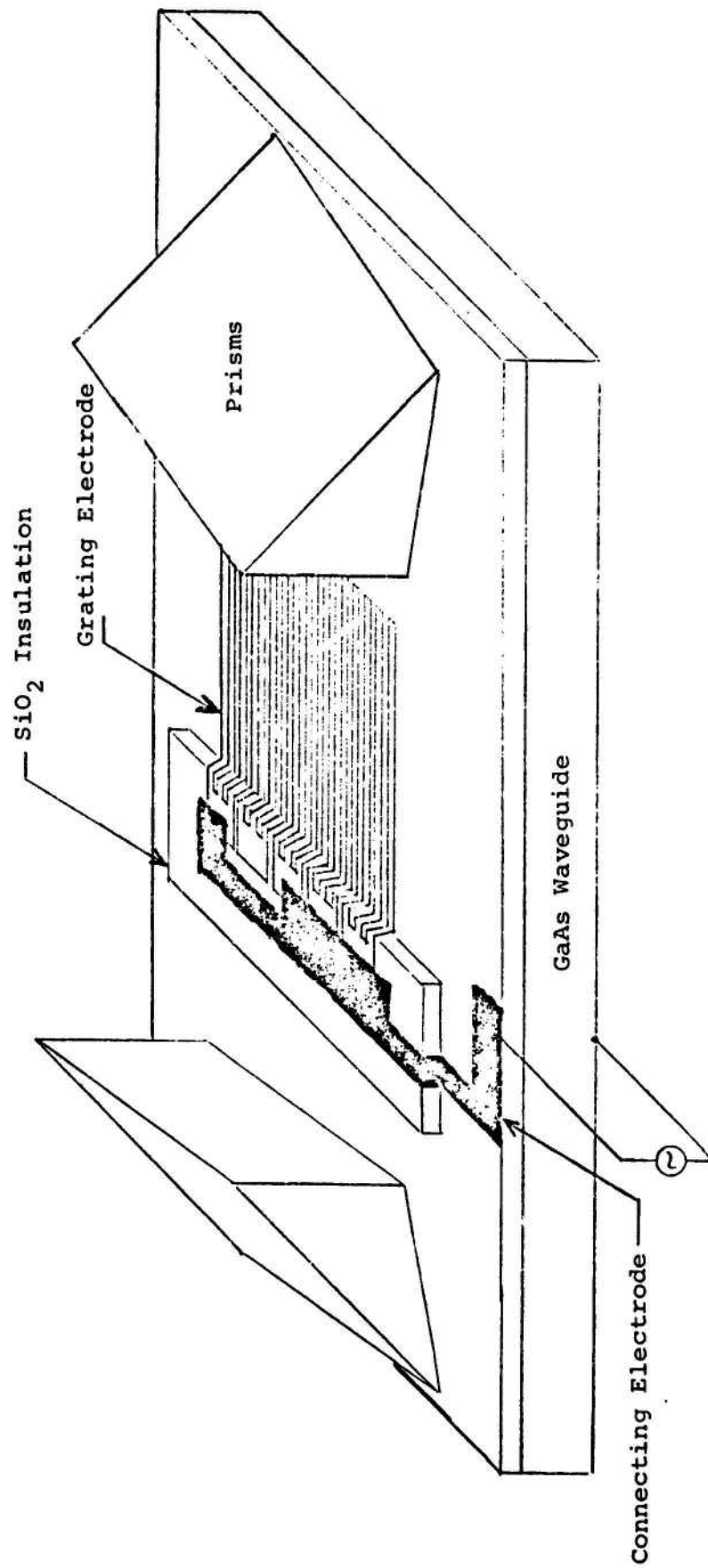


Figure 40. Illustration of Bragg's E-0 Modulator



Figure 41: Microscope Picture of the Grating Electrodes

along the expected Bragg's direction of deflection was observed. In order to increase the sensitivity of the detection scheme, the reverse bias voltage was chopped in synchronism with a reference voltage; phase sensitive detection was employed so that even a small change in incident power or a small deflected power could be measured. According to the results given in Figure 31, we should have less than 1% efficiency in deflection for 60V of applied voltage and 1 cm of interaction length for the waveguide employed (13.7 μm film in an n+GaAs substrate). Experimentally we measured the deflection efficiency to be somewhere between 0.1% and 1%. Theoretically a thin waveguide (say 5 μm thick) together with grating fingers of 5 cm long should yield a deflection efficiency of more than 50% at 60V of applied modulation voltage.

In short, we have successfully demonstrated the Bragg's electro-optical modulation. The efficiency is low because we used an existing structure that is not optimized for this application.

5.2 Grating and Prism Couplers

Prism couplers are used in most of the laboratory experiments because they are very convenient to use. However, this is not true when the waveguide has both very high film refractive index and a very small difference in the refractive indices of the film and the substrate. In that case: (a) The evanescent tail on the air side is very short (the length of the evanescent tail is $\lambda_0/2\pi n_f$). (b) Most of the energy of the guided wave mode will be contained in the film and in the substrate. Unless the air gap between the prism and the waveguide surface is less than the length of the evanescent tail, the coupling efficiency will be

very low. For GaAs waveguides at $1\ \mu\text{m}$, this means that the gap distance must be less or equal to $\sim 500\text{\AA}$. Such a gap distance is very difficult to achieve. Consequently, the best efficiency that we have been able to achieve is much less than 1%. Furthermore, there is no other known material transparent at $1\ \mu\text{m}$ that has a refractive index higher than GaAs. A GaAs prism is only barely usable because the β_g/k of the guided wave will be just slightly less than the refractive index of the prism.

These difficulties can be partially circumvented by means of the grating coupler, because the grating coupler can be placed right on the waveguide surface. However, the coupling of the laser radiation to the guided wave mode through the grating is still quite weak unless the index of the grating is high. In other words, the ratio of the energy contained in the evanescent tail is so small compared to the energy contained in the film and in the substrate that a grating of low refractive index will not be very effective. We have fabricated photoresist gratings on GaAs / $\text{GaAs}_{1-x}\text{P}_x$ waveguides by exposing photoresist with two interfering Argon laser beams. The periodicity of the grating is 3500\AA . The depth of the grating is about 1500\AA . When a 5mm Nd:YAG laser beam is used to excite the guided wave, a coupling efficiency of 0.1% is obtained. In principle, the maximum excitation efficiency should always be 81%, independent of the coupling strength. In practice, both the waveguide non-uniformity and the size of the laser beam will limit the maximum interaction length to just a few mm. A very weak coupling strength will result in a low coupling efficiency. This argument suggests that an etched grating should be used

to increase the coupling efficiency. An experimental confirmation of this prediction was obtained when we chemically etched the GaAs waveguide from the photoresist grating. Chemical etching was chosen instead of sputter etching so that a deeper grating can be obtained. The measured coupling efficiency, without any elaborate effort to maximize it by refocusing the laser beam is 4%.

A grating coupler at $3.5 \mu\text{m}$ periodicity has also been fabricated under this contract for the $10.6 \mu\text{m}$ wavelength. In that case, the grating mask was purchased from commercial mask suppliers. We have successfully excited guided wave modes in GaAs/n+GaAs waveguides by the grating coupler fabricated in this manner. However, the prism coupler is more efficient and more convenient to use in the laboratory. Therefore, the experimental work on grating couplers for the $10.6 \mu\text{m}$ wavelength was discontinued after 1973.

5.3 Fiber to Thin Film Coupling

A large part of the potential technical and economic benefit of fiber optics communications remains currently unrealized because of the present lack of readily fabricated, efficient fiber-film couplers that would make available to fiber optics the system functions that can be performed in GaAs thin-film waveguides. We have already proposed to AFCL/ARPA and to the Office of Naval Research a comprehensive program on fiber to film couplings. In order to make some immediate advances in this important area, we have chosen to investigate a simple, but fundamental, aspect of the fiber to thin-film coupling problem, namely the coupling of a tapered thin-film waveguide with low substrate index to a single mode ribbon fiber.

Consider first the coupling of a waveguide that has a low substrate refractive index n_s , to a glass ribbon fiber that has a mode with effective index $n_e = \beta_e/k$, where $n_e > n_s$. If the film of the waveguide is tapered and if the ribbon fiber is placed next to the film as shown in Figure 42 (a) the propagation wave number β_g and β_e of the film and the fiber will change continuously from section AA to CC. Somewhere in the tapered region the β_g of the guided wave mode is matched to the β_e of the fiber mode as shown in Figure 42 (b). As in the situation investigated by Wilson and Teh, at University College, London, one expects that the energy will be transferred completely from the guided mode to the fiber mode or vice versa at BB, provided that tapering is gentle enough and that the air gap is smaller than the range of the evanescent fields. (23)

From another point of view, both the field configuration and the phase velocity of the guided wave mode change continuously in the tapered region. For very gentle tapering, the modes at any given cross section, such as BB, can be approximated by modes of uniform waveguides of the same dimensions and indices; these are commonly called the local modes in the adiabatic approximation. We expect that one of the local modes at the AA section in the waveguide will transform smoothly into only one of the local modes of the ribbon fiber at the CC section (24). Since the local modes are orthogonal to each other at each cross section, all the energy will be transferred from one mode at section AA to one mode at section CC.

Experimentally, ribbon waveguide with cladding on one side is simulated by sputter deposited thin-film glass waveguide. To yield a tapered thin-film waveguide, a shield is used in the sputter deposition

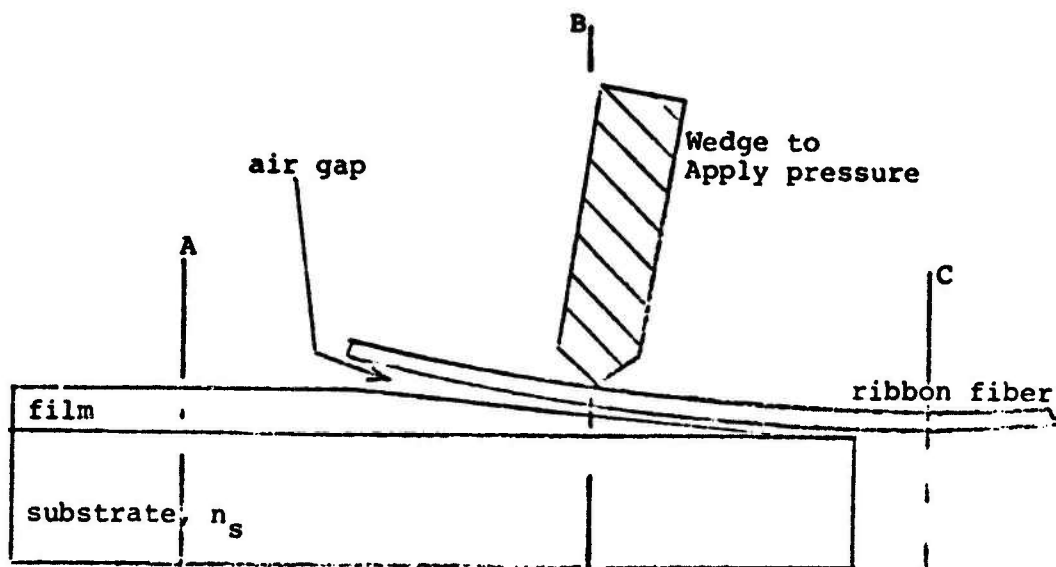


Fig. 42 (a) , The Tapered Thin-Film Directional Coupler

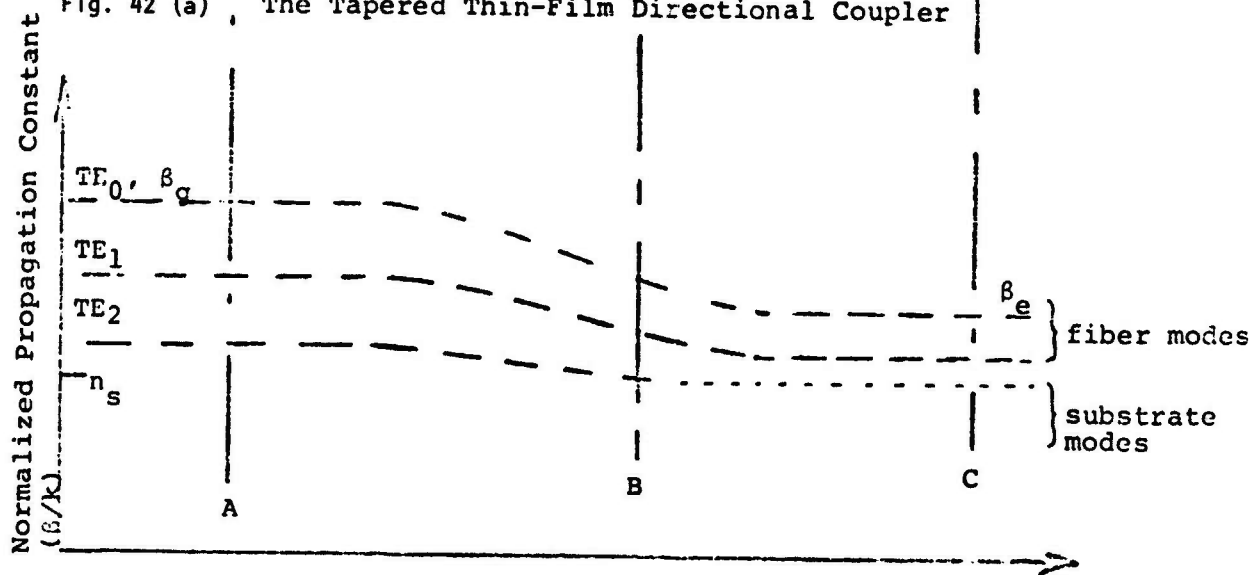


Figure 42:(b) The Normalized Propagation Constant (β/k) in the Tapered Thin-Film Directional Coupler

process so that the thickness of a thin-film glass waveguide is gradually reduced to zero. By adjusting the distance between the shield and the substrate, tapers of different slopes can be obtained. Figure 43 (a) shows the sketch of the experimental setup. Figure 43 (b) shows the β/k diagram of the various modes involved. Index matching oil with $n = 1.50$ is used to increase the coupling between the two waveguides. A coupling efficiency (from TE_0 mode of guide No. 1 to TE_0 mode of guide No. 2) of 85% has been obtained consistently for several similar structures. A maximum efficiency of 100% was obtained in one instance. A continuation of this experiment is currently being carried out beyond the contract period of this program, temporarily under partial support from NSF and Washington University. A theoretical analysis of this coupler has already been made by Milton and Burns of the Naval Research Laboratory (25, 26).

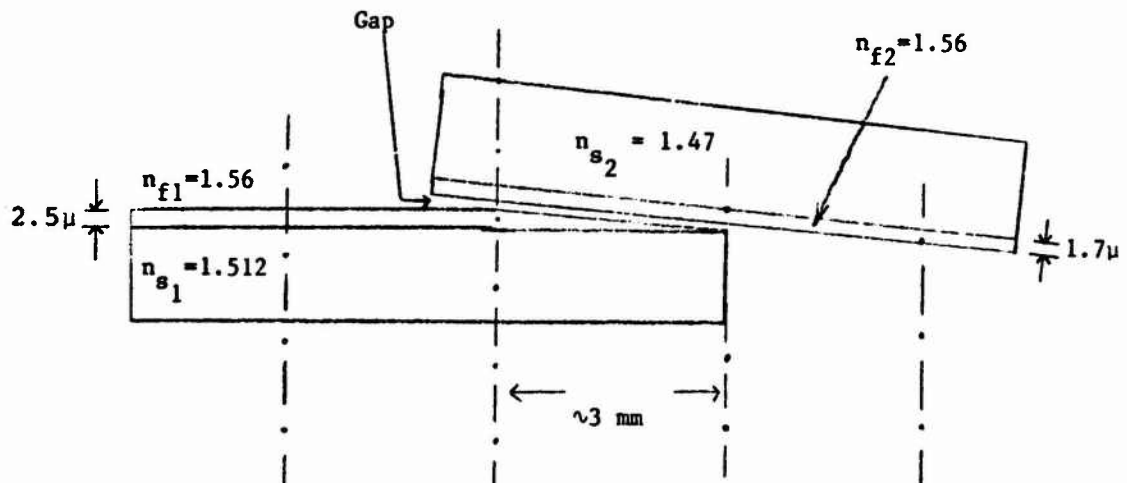


Fig. 42(a)

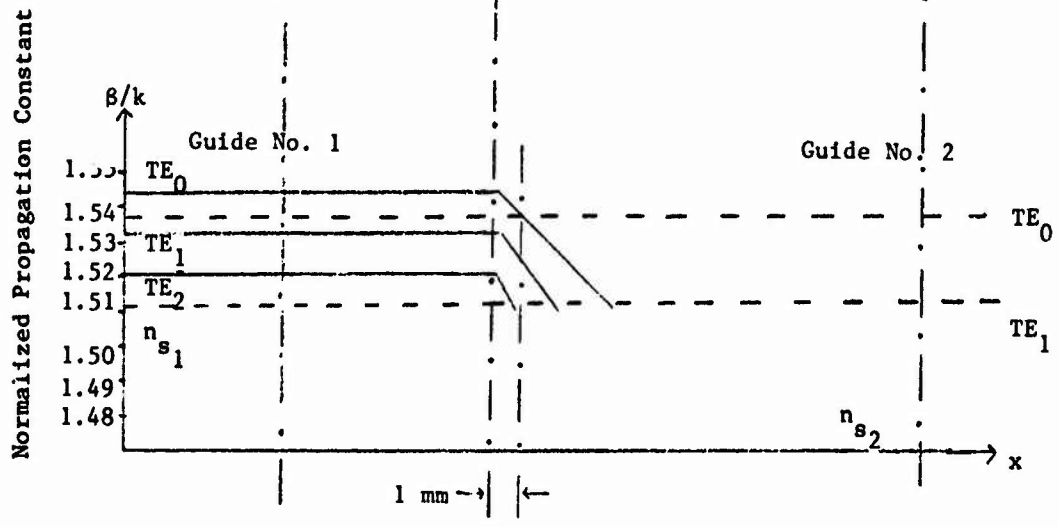


Fig. 43 Illustration of the Tapered Velocity Coupling Experiment Between Two Glass Waveguides

6. CONCLUSION

High-performance, low-loss, and large-area GaAs/n+GaAs, GaAs/GaAs_{1-x}P_x and GaAs/Ga_{1-y}Al_yAs waveguides have been successfully fabricated under this contract by VPE and LPE methods for 10.6 μm applications. Techniques for controlling the film uniformity, for reducing the free carrier concentration, and for obtaining flat epitaxial wafers of GaAs_{1-x}P_x have been developed. Waveguide attenuation rates in the range of 1 to 2 db/cm have been obtained in single- and double-mode GaAs/GaAs_{1-x}P_x waveguides and in thick multimode GaAs/n+GaAs waveguides. Analysis of the electrooptical waveguide modulator shows that single-mode waveguides several cm long and with film thickness not too far from cut-off, will give the best modulation efficiency. However, in order to raise the r.f. impedance and to reduce the drive power, two-dimensional waveguide modulators should be used. Low-loss two-dimensional waveguides have been successfully fabricated under this contract. Demonstration of one-dimensional waveguide modulation has also been carried out, because of time limitations, experimental evaluation of the two-dimensional waveguide modulator was not completed. Theoretical results indicate that P/Δf of the order of 100 mW/MHz and total insertion loss of the order of 6 db can realistically be expected from two-dimensional waveguide modulators. The performance of such modulators would be orders of magnitude better than that obtainable from bulk modulators. Therefore, we recommend highly that the development of two-dimensional modulator be undertaken whenever, in the future, the funding permits.

A VPE technique has also been successfully used to fabricate thin GaAs/GaAs_{1-x}P_x waveguides for 1.06 μm applications. In spite of the visible cross-hatch pattern, the measured attenuation rate is 1 db/cm for single- or double-mode waveguides. Because of the expiration of the contract period, the waveguide characteristics have not been fully evaluated. For example, the degree to which the cross hatch may cause mode conversion in multimode waveguide has not been measured. The strain produced by the lattice mismatch between GaAs (or GaAs_{1-z}P_z) may also cause a broadening of the absorption band of the epitaxial layer, thereby increasing the attenuation rate at the 0.9 μm wavelength. The degree to which the cross-hatch pattern can be reduced by changing the alloy composition is not known. Since large-area GaAs (or GaAsP or GaAlAs) waveguides are also very important in realizing monolithic integrated optical circuits in the near infrared, continuation of the investigation of the GaAsP waveguide for near infrared applications would be highly desirable.

7. REFERENCES

- (1) R. A. Ruehrwein, "Manufacturing Methods for Epitaxially Growing GaAs-GaP Single Crystall Alloys", Tech. Rept., AFML-TR-68-319, Oct., 1968.
- (2) M. G. Craford and W. O. Groves, "Vapor Phase Materials for LED Applications", Proc. IEEE, 61, pp. 852-880 (1973).
- (3) K. L. Lawley, et al., "Manufacturing Methods for GaAs", Final Technical Report, AFML-TR-71-55, March, 1971.
- (4) J. W. Burd, "A Multi-Wafer Growth System for the Epitaxial Deposition of GaAs and GaAs_{1-x}P_x", Transaction of the Metallurgical Society of AIME, Vol. 245, pp. 571-576, March, 1969.
- (5) P. L. Hoyt and R. W. Haisty, "The Preparation of Epitaxial Semi-Insulating Gallium Arsenide by Iron Doping", J. Electrochem. Soc. 113, 296-297, (1966).
- (6) W. G. Spitzer and J. M. Whelan, "Infrared Absorption and Electron Effective Mass in n-type Gallium Arsenide", Phys. Rev., Vol. 114, pp. 59-63, April 1, 1959.
- (7) M. G. Mil'vidskii, V. B. Osvenskii, E. P. Rashevskaya and T. G. Yugova, "Investigation of the Infrared Absorption Spectrum of n-Type Gallium Arsenide", Soviet Physics - Solid State, 7, pp. 2784-2786, May, 1966.
- (8) P. K. Cheo, J. M. Berak, W. Oshinsky, and J. L. Swindal, "Optical Waveguide Structures for CO₂ Laser", Appl. Opt. Vol. 12, pp. 500-508, March, 1973.
- (9) R. Weil, "Interference of 10.6 μm Coherent Radiation in a 5-cm Long Gallium Arsenide Parallelepiped", J. Appl. Phys., Vol. 40, pp. 2856-2859, June, 1969.
- (10) J. M. McFee, M.A. Pollack, W. W. Rigrod, and R. A. Logan, "Heterostructure GaAs-AlGaAs Planar Waveguide for 10.6 μm ", Digest of Technical Papers, IEEE-OSA Topical Meeting on Integrated Optics, New Orleans, pp. MA 7-1 to MA 7-4, January 21 - 24, 1974.
- (11) F. S. Chen, "Modulators for Optical Communications", Proc. IEEE, Vol. 58, pp. 1440-1456, 1970.
- (12) W. S. C. Chang, M. W. Muller, and F. J. Rosenbaum, "Integrated Optics", Laser Applications, Vol. II, Academic Press, N. Y., pp. 227-343, 1974, editor M. Ross.
- (13) J. F. Lotspeich, "Single-Crystall Electro-optic Thin Film Waveguide Modulators for Infra-red Systems", Appl. Opt. Vol. 13, pp. 2529-2538, 1974.
- (14) P. K. Cheo, "Electrooptical Properties of Reverse Biased GaAs Epitaxial Thin Film Waveguides at 10.6 μm ", Appl. Phys. Lett., Vol. 23, pp. 439-441, 1973.

- (15) P. K. Cheo, "Pulse Amplitude Modulation of a CO₂ Laser in an Electrooptic Thin Film Waveguide", Appl. Phys. Lett., Vol. 22, pp. 241-244, 1973.
- (16) P. K. Cheo and M. Gilden, "Microwave Modulation of CO₂ Lasers in GaAs Optical Waveguides", Appl. Phys. Lett., Vol. 25, pp. 272-274, 1974.
- (17) T. Ko, "An Investigation of Electrooptical Modulation Methods in GaAs Epitaxial Waveguides at 10.6 um Wavelength", D. Sc. dissertation, Department of Electrical Engineering, Washington University, St. Louis, Missouri, USA, June, 1974, also
 Technical Report 1974-2, Laboratory for Applied Electronic Sciences, Washington University April, 1974.
- (18) D. Marcuse, "Theory of Dielectric Optical Waveguides", Academic Press, N.Y., 1974.
- (19) J. H. Hammer, D. J. Channin, and M. T. Duffy, "Fast Electrooptical Waveguide Deflector Modulator", Appl. Phys. Lett., Vol. 23, pp. 176-177, 1973.
- (20) J. N. Polky and J. H. Harris, "Intedigital Electrooptic Thin Film Modulator ", Appl. Phys. Lett., Vol. 21, pp. 307-309, 1972.
- (21) E. A. J. Marcatili, "Dielectric Rectangular Waveguide and Directional Coupler for Integrated Optics", Bell Syst. Tech. J. Vol, 48, pp. 2071-2102, 1969.
- (22) F. Horrigan, C. Kein, R. Rudko, D. Wilson, "Windows for High Power Lasers", Microwaves, Vol. 8, p. 66, 1969.
- (23) M. G. F. Wilson, G. A. Tech. "Tapered Optical Directional Coupler", IEEE Trans. MTT special issue on Integrated Optics, Vol. MTT-23, p. 85, 1975.
- (24) P. K. Tien, R. J. Martin, G. Smolinsky, "Formation of Light-Guiding Interconnections in an Integrated Optical Circuit by Composite Tapered-Film Coupling", Applied Optics, Vol. 12, p. 1909, 1973.
- (25) W. K. Burns and A. F. Milton, "Mode Conversion in Planar Dielectric Separating Waveguides", Naval Research Labortory, to be published.
- (26) A. F. Milton and W. K. Burns "The Design of Tapered Velocity Couplers", Naval Research Laboratory, to be published.

APPENDIX 1 List of Waveguide Samples Submitted for Evaluation

GaAs n/n⁺ Structures

<u>Sample Number</u>	<u>Film Thickness (μm)</u>	<u>Film Carrier Conc. (10¹⁴cm⁻³)</u>	<u>Substrate Carrier Conc. (10¹⁸cm⁻³)</u>	<u>Remarks</u>
5-205 (1)	29	150	1.1	
(2)	29	150	1.1	
(3)	29	150	4	m = 0, 3 5.6 db/cm 13.3
(4)	29	150	0.6	
5-231 (1)	26	27	4	m = 0, 1, 2, 3 1.2 db/cm 3.4, 8.2, 20
(2)	26	27	0.2	erratic output coupling 2-D waveguide exp.
(3)	26	27	0.6	" " "
(4)	26	27	1.1	erratic measure.
1-8 (1)	34.3	6.3	4	m = 0, 1, 2, 3, 4 2.6 db/cm, 4.7, 7.4, 10.7, 18
(2)	34.3	6.3	4	2 D waveguide exp.
(3)	34.3	6.3	4	2 D waveguide exp.
1-16 (1)	29.4	12	0.2	2 D waveguide exp.
(2)	29.4	12	0.2	2 D waveguide exp.
(3)	29.4	12	0.2	2 D waveguide exp.
(4)	29.4	12	0.2	small - not used
(5)	29.4	12	0.2	2 D waveguide exp.
(6)	29.4	12	0.2	2 D waveguide exp.
1-17 (1)	23.4	6.4	4	Modulation exp.
(2)	23.4	6.4	4	n = 0 2.6 db/cm
(3)	23.4	6.4	4	K. W.
(4)	23.4	6.4	4	modulation exp.
(5)	23.4	6.4	4	modulation exp.
5-282 (1)	17.6	3.9	4	poor surface m = 0 6.6 db/cm
(2)	17.6	3.9	2	too small
(3)	17.6	3.9	2	too small
5-289 (1)	13.8	3.0	1	good 2-D waveguide 13 db/cm ≈ 35 μm wide
(2)	13.8	3.0	1	2-D waveguide exp.
(3)	13.8	3.0	0.6	K. W.
5-302 (1)	25	5.4	4	m = 0, 1 8.75 db/cm, 9.45
(2)	25	5.4	4	K. W.

GaAs n/n⁺ Structures (Cont.)

<u>Sample Number</u>	<u>Film Thickness (μm)</u>	<u>Film Carrier Conc. (10¹⁴cm⁻³)</u>	<u>Substrate Carrier Conc. (10¹⁶cm⁻³)</u>	<u>Remarks</u>
5-303 (2)	13.7	46	4	erratic coupling
5-304	18.5	5.8	4	modulation exp.
5-415	5.5	4.3	~2	2-D waveguide eval.
5-416	5.7	0.11	2	2-D waveguide eval.
5-417	6.0	13	2	2-D waveguide eval.
5-421	21.1	2.9	2	2-D waveguide eval.
5-422	25.4	3.5	2	2-D waveguide eval.
5-423	23.7	6.9	2	to AFCRL for ion implant
5-424	21.5	~5	2	2-D waveguide eval.
6-223 (2)	3.0	<2.4	~2	
6-224 (2)	4.0	~1	~2	
6-225 (2)	4.0	~1	~2	
6-227 (2)	4.0	~1	~2	

Thick GaAs/GaAsP Structures

(Thickness of alloy layer, ~40μ; graded layer ~40μ)

<u>Sample Number</u>	<u>Film Thickness (μm)</u>	<u>Alloy Comp. (% GaP)</u>	<u>Carrier Conc. (10¹⁴cm⁻³)</u>		<u>Remarks</u>
			<u>Film</u>	<u>Alloy</u>	
5-303	<13.7	38.6	46	160	m = 0 3.15 db/cm
5-340	10.1	22.8	9.3	810	m = 0, 1 1.34 db/cm, 2.75
5-347	19.5	22.8	7.6	810	poor coupling, wafer cracked from excessive bow
5-348 (1)	16.6	38.6	56	100	m = 0, 1 1.67 db/cm, 15.8
(2)	16.6	38.6	56	100	not evaluated
5-349	21.2	39.3	13	500	not evaluated
5-353	20	38.6	63	100	unable to excite guided wave
5-354 (1)	9.8	22.8	56	800	m = 0 1 db/cm
(2)	9.8	38.6	56	100	unable to reliably excite guided wave - bowed
5-355 (1)	8.8	38.6	35	100	unable to excite guided wave - bowed
(2)	8.8	22.8	35	800	poor coupling and erratic results - bowed
5-356 (1)	8.8	22.8	21	800	m = 0 1.8 db/cm
(2)	8.8	34.7	21	820	not evaluated
5-358 (1)	24.6	22.8	21	800	15 db/cm 0th mode ?
(2)	24.6	35	21	820	not evaluated

Thick GaAs/GaAsP Structures (Cont.)

Sample Number	Film Thickness (μm)	Alloy Comp. (% GaP)	Carrier Conc. (10^{14}cm^{-3})		Remarks
			Film	Alloy	
5-489	10	~35	~1	760	Rough surface
5-493	7.8	~35	~1	480	Bowed surface
6-1	9.6	~35	~1	460	Cracked while sawing
6-3	5.9	~35	~2	490	Bowed surface
6-5	7.8	~35	~1	370	<4 db/cm loss, bowed surf.
6-33	5.8	~35	0.54	260	Bow > 3 mil convex
6-35	7.8	~35	0.3	140	Bow 2.15 mil convex
6-37	6.8	~35	0.8	270	Bow 1.3 mil convex
6-39	9.8	~35	0.4	250	Bow 1.0 mil convex
6-42	4.9	~35	0.36	150	Bow 0.75 mil convex
6-44	7.8	~35	0.43	---	Bow 0.95 mil convex
6-47	13.7	~35	0.37	---	Bow 0.55 mil convex
6-54	11.7	~35	0.15	---	
6-76	9.6	~35	0.27	59	Bow convex
6-78	7.8	~35	0.27	100	Bow convex
6-92	5.9	~35	0.45	140	
6-94	9.7	34.7	9.5	63	
6-96	7.8	~35	23.3	170	
6-98	9.8	~35	0.43	130	
6-115	4	~35	0.48	94	
6-122	22	~35	1.6	87	
6-124	5.8	~35	0.64	93	
6-133	6	~35	0.42	110	Rough surface
6-135	4	~35	0.47	54	Slightly hazy
6-138	10	~35	0.11	58	
6-147	5	~35	0.67	70	
6-149	4	~35	0.56	135	
6-151	6	~35	0.46	55	
6-154A	4	~35	0.48	46	
6-154B	4	~35	0.76	210	
6-156	49	~35	0.39	230	
6-158	44	~35	0.01	160	
6-215	3	33.5	1.07	30	
6-216	3	33.5	1.10	30	
6-217	3.8	33.0	0.96	17.3	
6-223 (1)	3	33.0	0.96	10.8	
6-244 (1)	3	33.0	3.6	10.8	
6-225 (1)	4	34.0	0.85	12.7	
6-226	4	34.0	0.96	2.2	
6-227 (1)	4	33.0	5.5	3.8	
6-229	4	34.0	1.51	12.7	
6-230	4	34.0	0.89	2.2	

Thick GaAs/GaAsP Structures (Cont.)

Sample Number	Film Thickness (μm)	Alloy Comp. (% GaP)	Carrier Conc. (10^{14}cm^{-3})		Remarks
			Film	Alloy	
6-231	6	34.0	1.39	13.3	
6-233	6	34.3	10.2	2.6	
6-236	7.8	34.5	28	2.0	
6-237	8.4	34.5	28	2.0	
6-239	7.8	34.5	24	5.3	
6-240	8.8	34.5	25	5.3	

Thin GaAs/GaAsP Structures

6-57	2.0	~35	4.7	30	
6-59	1.5	"	4.0	320	
6-66	1.4	"	15.0	510	
6-80	2.0	"	2.7	130	
6-90	2.5	"	1.4	130	
6-106	2.0	"	1.5	52	
6-111	2.9	"	0.8	30	
6-126	1.5	35.4	3.4	110	
6-129	1.2	~35	4.0	92	Rough surface
6-131	1.0	"	3.9	81	TE ₀ mode ~ 1 db/cm (Fig. 30)
6-177	2.0	"	2.8	44	
6-182 (1)	2.5	"	15.1	60	Hazy surface
(2)	2.5		15.1	60	Hazy surface
6-186	1.4	34	18	51	
6-187	1.6	~35	4.9	51	
6-193 (1)	1.2	31	9.7	100	
(2)	1.2	31	9.7	100	
6-194 (1)	1.5	~35	4.7	50	
(2)	1.5	"	4.7	50	
6-196 (1)	1.0	35	4.6	118	
(2)	"	"	"	"	
6-197 (1)	1.6	33	5.8	151	
(2)	"	"	"	"	
6-199 (1)	1.0	~35	4.8	147	
(2)	"			"	
6-250	1.5	21.0	3.6	18.6	
6-253	1.5	"	---	"	Slightly hazy
6-254 (1)	2.0	27.0	---	15.0	
(2)	"	"	---	"	

Sandwiched GaAsP/GaAs/GaAsP Structures

<u>Sample Number</u>	<u>Film Thickness (μm)</u>		<u>Alloy Comp. (% GaP)</u>	<u>Carrier Conc. (10^{14}cm^{-3})</u>		<u>Remarks</u>
	<u>Top Alloy</u>	<u>GaAs</u>		<u>GaAs</u>	<u>Subst. Alloy</u>	
6-109	10	8	~ 35	~ 0.5	110	
6-118	11.5	6	"	"	27	
6-143	5	5	"	"	75	6 db/cm
6-161	3.5	4.5	"	"	250	
6-164	4.0	4.5	"	"	250	
6-168 A	6.0	4.0	"	"	300	
6-168 B	4.0	5.0	"	"	390	

GaAsP/GaAsP Structures

<u>Sample Number</u>	<u>Film Thickness (μm)</u>	<u>Composition (% GaP)</u>		<u>Carrier Conc. (10^{14}cm^{-3})</u>	
		<u>Film</u>	<u>Substrate</u>	<u>Film</u>	<u>Substrate</u>
		6-170	37	8.5	35
6-173	55	10.5	35	---	8.9
6-241	1.2	20.0	34.5	---	3.0
6-242	1.5	~23	34.3	---	1.41
6-243	1.6	23.4	34.0	---	1.09

GaAs/GaAlAs Structures

<u>Sample Number</u>	<u>Film Thickness (μm)</u>	<u>Wavelength of PL emission of alloy (\AA)</u>	<u>Carrier Conc. (10^{14}cm^{-3})</u>		<u>Remarks</u>
			<u>Film</u>	<u>Alloy</u>	
5-436	5.8	7100	4.9	150	Small samples - surface planarity measurements
5-437	5.8	6900-7100	10	580	
5-452	7.8	6800-7100	19	220	m = 0, 1 db/cm, 5

APPENDIX 2 LIST OF PUBLICATIONS

1. D. Finn, W. O. Groves, L. G. Hellwig, M. G. Craford, W. S. C. Chang, M. S. Chang, and B. L. Sopori, "Low-loss Large-area GaAs/GaAsP Heterostructure as Optical Waveguide at $10.6\mu\text{m}$," *Optics Communications*, Vol. 11, p. 201, 1974.
2. B. L. Sopori, William S. C. Chang, and R. Vann, "Low-loss Two Dimensional GaAs Epitaxial Waveguides at $10.6\mu\text{m}$ Wavelength," *IEEE Transactions on Microwave Theory and Techniques*, Vol. MTT-22, p. 754, 1974.
3. William S. C. Chang, "Integrated Optics at $10.6\mu\text{m}$ Wavelength," *IEEE Transactions on Microwave Theory and Techniques*, Vol. MTT-23, p. 31, 1975.
4. M. S. Chang, W. S. C. Chang, B. L. Sopori, H. R. Vann, M. W. Muller, M. G. Craford, D. Finn, W. O. Groves, and A. H. Herzog, "GaAs Optical Waveguide Structures at $10.6\mu\text{m}$ Wavelength;" to be published in *Applied Optics*, May, 1975.
5. William S. C. Chang and Ton Ko, "An Analysis of UHF-VHF Electrooptical Modulation at $10.6\mu\text{m}$ Wavelength in GaAs Thin Film Waveguides," Submitted for publication, 1975.

APPENDIX 3 REFRACTIVE INDICES OF GaAs, Ga_{1-x}Al_xAs and

GaAs_{1-x}P_x

A.3.1 INTRODUCTION

Our research program is concerned with GaAs optical waveguides which have been considered by many researchers to be the most promising material for use in integrated optics. The GaAs optical waveguide formed by the difference of the free carrier concentration in the film and the substrate, i.e. GaAs/n⁺GaAs, has been found to be very lossy. GaAs films grown on Al_xGa_{1-x}As and GaAs_{1-x}P_x substrates have been demonstrated to be more promising. The heterostructures as optical waveguides offer the advantages that the free carrier concentrations in both the film and the alloy substrates can be kept to a minimum to reduce the free carrier absorption and that the waveguiding effect can still be achieved easily by changing the alloy composition.

In this memorandum, a summary of the published and unpublished results on the refractive indices of GaAs, Al_xGa_{1-x}As and GaAs_{1-x}P_x is presented. A knowledge of the variation of the refractive indices is essential to our work for calculating the waveguide mode characteristics. Our research program is concentrated at two optical wavelengths, $\lambda = 1.06\mu$ and $\lambda = 10.6\mu$. Particular attention is given to results at these two wavelengths. Published results on AlAs and GaP are also included here

as an aid to better understanding. Efforts have been made to bring the information up to date. It is the author's (M.S.Chang) understanding that the refractive indices of $\text{Al}_x\text{Ga}_{1-x}\text{As}$ and $\text{GaAs}_{1-x}\text{P}_x$ at long wavelength are not available in the literature. The results quoted in this memorandum constitute new information.

A.3.2 Refractive Index of GaAs

The refractive index of n-type GaAs in the 0.7 to 1.5 eV range of photon energy has been measured by Marple^(A1) by the prism refraction method. The GaAs single crystal prism used in his measurement was supplied by the Monsanto Chemical Company and was free of intentional doping, containing 6×10^{16} donors per cm^3 . The measured numerical values can be found from Reference A2 and are listed in Appendix A.3.a. Marple has performed a least-square analysis of his data, using a first-order Sellmeier equation of the following form^(A2)

$$n^2 = A + B \frac{\lambda^2}{\lambda^2 - C^2} \quad (\text{A1})$$

where at room temperature $A=8.950$, $B=2.054$ and $C^2=0.390$ and λ is in μm . At $\lambda=1.06\mu\text{m}$, $n=3.479$ from Eq (A1) and from Appendix A.1. Recently, Zoroofchi and Butler^(A3) calculated the refractive index of n-type GaAs near its fundamental absorption edge from 1.44 to 1.54 eV, and their results compare quite well with the index

measurements done by Marple^(A1) The free-carrier contribution to the index of refraction for n-type GaAs (based on an effective mass of 0.072m) is ^(A4)

$$\Delta n_{\text{intra}}(E) = - 9.6 \times 10^{-21} N/nE^2 \quad (\text{A-2})$$

where N, n and E are the electron concentration, the index of refraction and the photon energy, respectively. At low carrier concentration, this correction term is small for the optical wavelength in the one micron region. However, the dependence on the carrier concentration becomes strong at energies near the direct energy gap^(A5) At the longer optical wavelength, the refractive index of GaAs has been measured by Oswald and Shade^(A6) The numerical data can be found in Appendix A.3.a. At $\lambda = 10.6\mu\text{m}$, there are no accurate published data. Cheo et al^(A7) used $n=3.275$ for their waveguide calculation. Unpublished measurements^(A8) indicated $n=3.272$ for $N \sim 10^{16} \text{ cm}^{-3}$ and $n=3.274$ for a very pure GaAs crystal. We have been using $n=3.27$ in our semi-annual reports. The free-carrier contribution at $\lambda = 10.6\mu\text{m}$ is significant. Chang^(A9) gives the following approximation

$$n^2 \approx 10.7 - 1.53 \times 10^{-18} N \quad (\text{A-3})$$

where N is the electron concentration.

A.3.3 REFRACTIVE INDEX OF $\text{Al}_x\text{Ga}_{1-x}\text{As}$

The refractive index of AlAs in the 0.5 to 2.2 eV range

of photon energy has been measured by Fern and Onton.^(A10) At $\lambda = 1.06\mu\text{m}$, $n_{\text{AlAs}} = 2.940$. There are no published data at long wavelength. By extrapolating Figure A1 of Fern and Onton^(A10), we take $n_{\text{AlAs}} = 2.86$ at $\lambda = 10.6\mu\text{m}$. The validity of this extrapolation is yet to be proved.

Recently, the refractive index of $\text{Al}_x\text{Ga}_{1-x}\text{As}$ between 1.2 to 1.8 eV has been measured by Casey et al.^(A11) Their results shown in Figure A1 agree reasonably well with the theoretical calculation^(A12) based on the modification of the semi-empirical single-effective-oscillator model. In Figure A2, the insert is drawn to show that n bows downward slightly from the linear variation (dashed line) between $n = 3.590$ for GaAs and to 2.971 for AlAs at 1.38 eV (0.9 μm wavelength). This result indicates that the difference in the refractive index of $\text{Al}_x\text{Ga}_{1-x}\text{As}$ from GaAs, Δn , can be approximated as a linear function of x as $\Delta n = -0.619x$ at $\lambda = 0.9\mu\text{m}$. This linear approximation enables us to find the refractive index of $\text{Al}_x\text{Ga}_{1-x}\text{As}$ for any x composition. Very recently, Afromowitz^{A13} measured the Δn for low Al concentration (i.e. 10-15%) and obtained a relationship $\Delta n = -0.83x$ at $\lambda = 8800\text{\AA}$, which is nearly twice the change measured by Buller and Kressel^(A14) on active devices. The reason for this discrepancy between the passive and active waveguides is not clearly understood yet. For $\lambda = 1.06\mu\text{m}$, we find $n_{\text{AlAs}} = 2.940$ from Reference 10 and $n_{\text{GaAs}} = 3.475$ from Appendix A.3.a, so we have

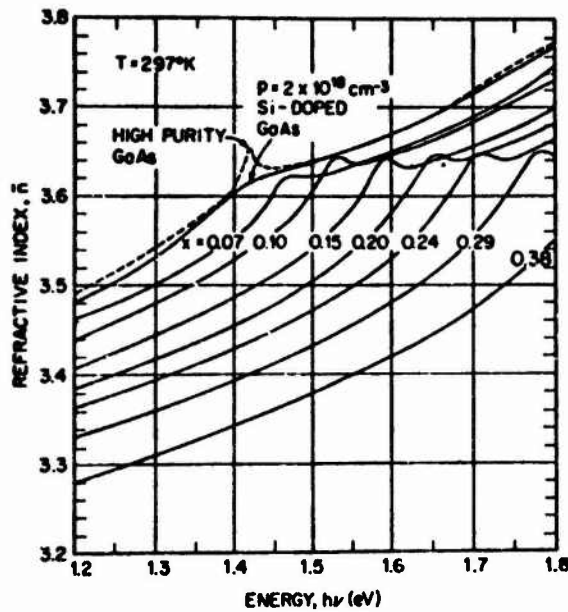


Figure A1. Refractive index as a function of photon energy for $\text{Al}_x\text{Ga}_{1-x}\text{As}$. For purposes of comparison, the refractive index (Ref. 5) of high-purity GaAs and Si-doped GaAs that is often used for active layers of GaAs- $\text{Al}_x\text{Ga}_{1-x}\text{As}$ heterostructure lasers is also given. (After Ref. 11)

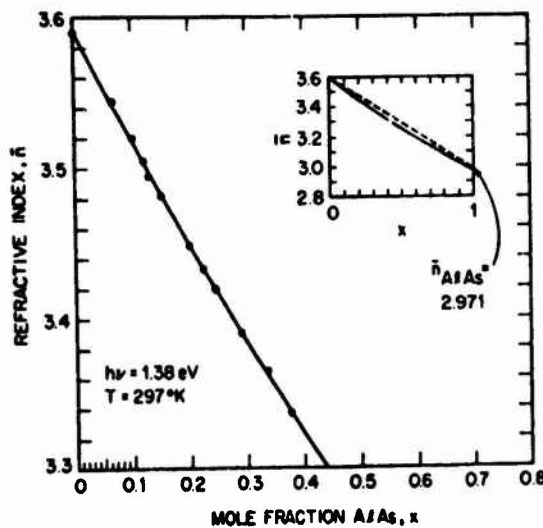


Figure A2. Refractive index of $\text{Al}_x\text{Ga}_{1-x}\text{As}$ as a function of x at the heterostructure laser emission energy of 1.38 eV. The dashed line in the inset is a linear extrapolation of the refractive index of 3.590 for GaAs (Ref. 5) to the refractive index of 2.971 for AsAs (Ref. 10). The uncertainty in the refractive index values for these measurements is ± 0.005 , while the uncertainty for the techniques used to assign x is generally taken as ± 0.02 . (After Ref. 11).

$$\Delta n = - 0.54X \quad \text{at } \lambda=1.06\mu\text{m} \quad (\text{A-4})$$

Table A.3.1 summarizes the depression Δn in the near infrared region.

There are no published results on $\text{Al}_x\text{Ga}_{1-x}\text{As}$ at long wavelength. Very recently, McFee et al^{A15} have performed a waveguiding experiment on their $\text{GaAs}/\text{Al}_x\text{Ga}_{1-x}\text{As}$ heterostructure at $\lambda=10.6\mu\text{m}$. Both the GaAs film and the $\text{Al}_x\text{Ga}_{1-x}\text{As}$ substrate are grown by liquid phase epitaxy and have a carrier concentration of 10^{16} cm^{-3} . By using the extrapolated the index of AlAs at $10.6\mu\text{m}$ from the near-IR measurements^{A10} and the unpublished data^{A8} of the GaAs index, they give the following refractive index equation for $\text{Al}_x\text{Ga}_{1-x}\text{As}$

$$n^2(x) = (2.86)^2 x + (3.27)^2 (1-x) \quad (\text{A-5})$$

This equation is very approximate because of the uncertainty of the extrapolation. The liquid phase epitaxial layer of $\text{Al}_x\text{Ga}_{1-x}\text{As}$ is found to have a graded refractive index. To interpret the results, a new waveguide theory has been developed by McFee et al^{A15}. With this, the refractive indices of the waveguide structure can be determined from the measurements of the angle of incidence of the waveguide modes. Sample 491 has been measured to have 10 TE modes which include both guided and leaky modes. The first nine modes are used in the computer calculation giving the following results: $n_{\text{GaAs}}=3.265$, $n_{\text{Al}_x\text{Ga}_{1-x}\text{As}} = 3.162$. The lower refractive index of GaAs is possibly due to the higher carrier concentration. The photoluminescence measurement of the $\text{Al}_x\text{Ga}_{1-x}\text{As}$ indicates $x=0.24$. From these numbers, we obtain a linear depression for $\text{Al}_x\text{Ga}_{1-x}\text{As}$ as

Table A.3.1 The Linear Depression of the Refractive Indices of $\text{Al}_x\text{Ga}_{1-x}\text{As}$ and $\text{GaAs}_{1-x}\text{P}_x$ as a Function of x (Ref. 1, 10, 16).

λ μm	$\text{Al}_x\text{Ga}_{1-x}\text{As}$ $n = -(\)X$	$\text{GaAs}_{1-x}\text{P}_x$ $n = -(\)X$
0.88	0.83(passive) 0.5 (active)	
0.9	0.62	0.44
1.0	0.56	0.39
1.06	0.54	0.37
1.15	0.52	0.36
1.20	0.51	0.35

Table A.3.2 Curve-fit parameters for refractive index $n^2 = n^2 = A + B \lambda^2 / (\lambda^2 - C)$ as a function of x for $\text{Ga}(\text{As}_{1-x}\text{P}_x)$. (After Ref. 21).

300°K					
$A = 4.1189 + 4.0625x - 10.3446x^2 + 2.7809x^3$					
$B = 6.6369 - 5.8747x + 10.6049x^2 - 2.9874x^3$					
$C = [1.23978 / (2.9025 + 0.5088x + 1.1201x^2)]$					
X	A	B	C	n_e	Maximum error
300°K					
0.0	4.0518	6.6961	0.1820	10.7479	0.0034
0.06	0.1956	10.4358	0.1182	10.6314	0.0030
0.125	4.2798	6.1803	0.1721	10.4601	0.0034
0.25	4.6599	5.6310	0.1622	10.2909	0.0042
0.35	4.3483	5.8149	0.1486	10.1632	0.0036
0.417	4.1354	5.8977	0.1390	10.0331	0.0030
0.625	0.3963	9.2210	0.0876	9.6203	0.0048
1.00	0.6215	8.3765	0.0749	8.9980	0.0060

$$\Delta n = - 0.43X \quad \text{at } \lambda=10.6\mu\text{m} \quad (\text{A-6})$$

Eq A-6 means that the refractive index of AlAs at 10.6 μm wavelength is about 2.84, which is very close to the extrapolated value 2.86 discussed earlier. By substituting $n_{\text{Al}_x\text{Ga}_{1-x}\text{As}} = 3.162$ into Eq A-5, we obtain a calculated value of $x=0.28$, which is reasonably close to the measured value of 0.24, considering the crude approximation of Eq(5). We prefer to use the linear approximation of Eq (6). The actual value may be slightly smaller than this linearly approximated value for a given x . Consider the GaAs film grown by our vapor phase epitaxy: the carrier concentration is in the low 10^{14} cm^{-3} range, so the index is $n_{\text{GaAs}}=3.27$. Now, we take this measured value $n_{\text{Al}_x\text{Ga}_{1-x}\text{As}}=3.16$ and we have

$$\Delta n = - 0.46X \quad \text{at } \lambda=10.6\mu\text{m} \quad (\text{A-7})$$

A.3.4 REFRACTIVE INDEX OF $\text{GaAs}_{1-x}\text{P}_x$

The refractive index of GaP in the region of 0.5 to 4.0 μm wavelengths has been measured by Bond^{A16}. The numerical values are listed in Appendix A.3b. At $\lambda=1.06\mu\text{m}$, $n_{\text{GaP}}=3.108$. Yas'kov and Pikhtin^{A17} also made measurements in the range of 1.0 to 2.5 eV photon energy, reasonably in agreement with Bond^{A16}. At $\lambda=10\mu\text{m}$, the only result is given by Folberth and Oswald^{A18} and $n_{\text{GaP}}=2.90$ from Appendix A.3c. For wavelengths between 16 to 30 μm , Kleinman and Spitzer^{A19} calculated the refractive index of GaP from their

measured reflectivity coefficients. There is a dropoff in the refractive index for $\lambda > 16\mu\text{m}$ due to the fundamental absorption peak at $27.3\mu\text{m}$. For wavelengths ranging from 30 to $100\mu\text{m}$, Abagyan et al^{A20} also showed a peak near $\lambda = 30\mu\text{m}$.

The refractive index of $\text{GaAs}_{1-x}\text{P}_x$ between 0.5 to 2.5 eV has been measured by Clark and Holonyak^{A21}. Their results are shown in Figures A3 and A4. Their measurements on pure GaP agree well with the results of Bond^{A16}. They give an expression for the refractive index of $\text{GaAs}_{1-x}\text{P}_x$ as follows:

$$n^2 = A + \frac{B\lambda^2}{(\lambda^2 - C)} \quad (\text{A-8})$$

with the curve-fit parameters A, B and C shown in Table A.3.2, and λ in μm . With the parameters given in Table A.3.2 (b), we have calculated n by Eq A-8 for $\lambda = 1.06\mu\text{m}$. The results are plotted in Figure A5. The linear variation of the refractive index of $\text{GaAs}_{1-x}\text{P}_x$ gives

$$\Delta n = -0.37X \quad \text{at } \lambda = 1.06\mu\text{m} \quad (\text{A-9})$$

The calculated points lie slightly below this linear curve. Table A.3.1 summarizes Δn in the $1.0\mu\text{m}$ region. Very recently, the refractive index of $\text{GaAs}_{0.62}\text{P}_{0.38}$ between 1.2 and 2.0 eV has been published^{A22} agreeing with the theoretical model^{A12}

There are no published data on the refractive index of $\text{GaAs}_{1-x}\text{P}_x$ at $10.6\mu\text{m}$ wavelength. The only available number for GaP is $n = 2.90$ at $10\mu\text{m}$ from Reference. If we use $n = 3.27$ for GaAs, we obtain an approximate $\Delta n = -0.37X$ for $\text{GaAs}_{1-x}\text{P}_x$ at

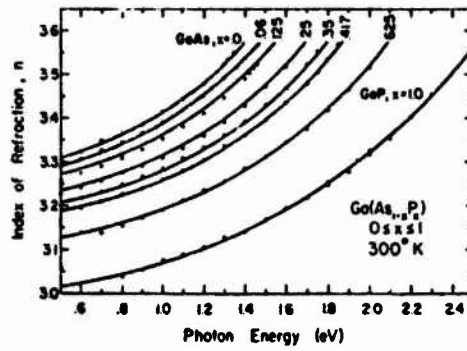
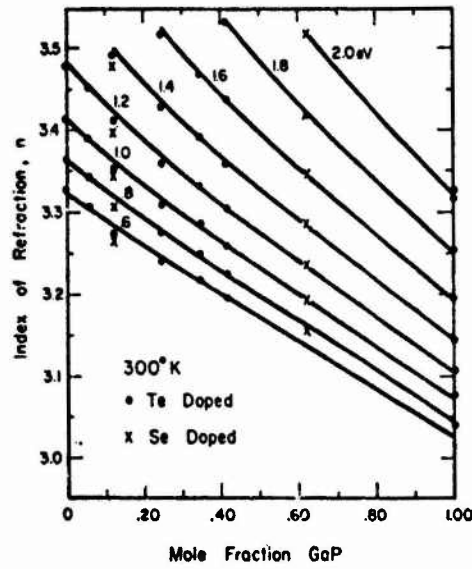
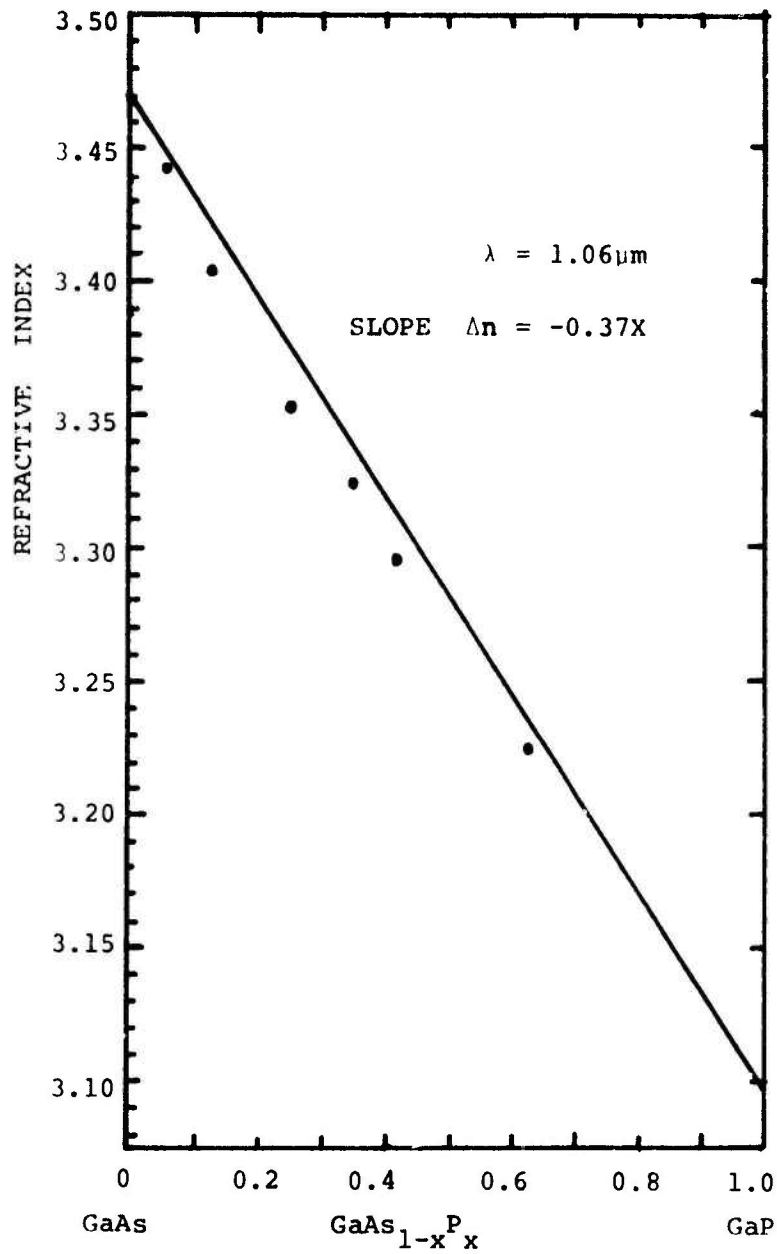


Fig. A3 Index of refraction of Ga(AsP) at 300°K as a function of photon energy $h\nu$; several values of mole fraction GaP. Solid lines are the result of curve fitting. (After Ref. 21)



(a)

Fig. A4 (a) Index of refraction of Ga(AsP) at 300°K as a function of mole fraction GaP for constant values of photon energy. (After Ref. 21)



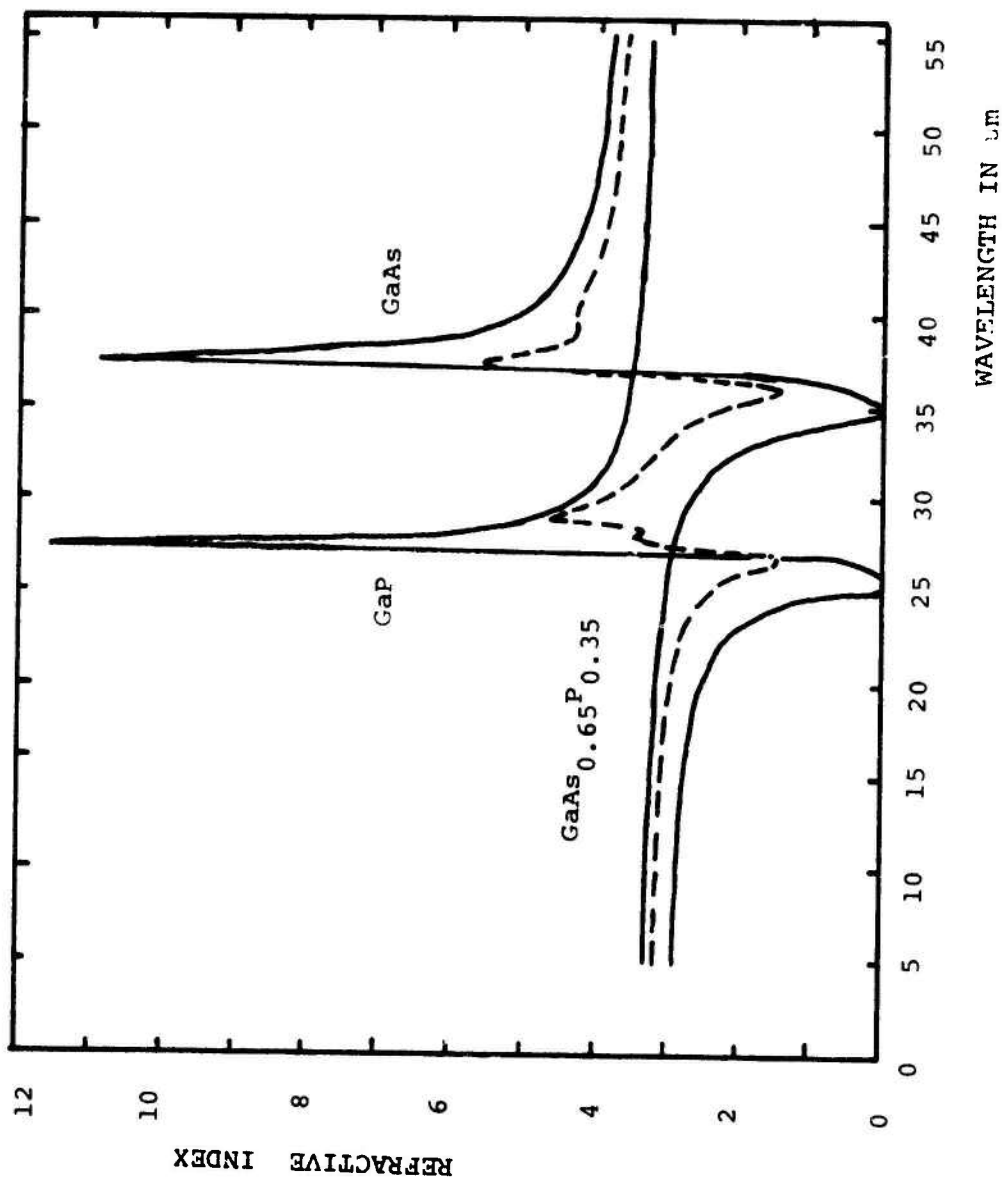
FigureA5 Index of refraction of $\text{GaAs}_{1-x}\text{P}_x$ as a function of mole fraction of GaP at $\lambda = 1.06\mu\text{m}$.

$\lambda = 10.6\mu\text{m}$. We now seek the validity of this approximation. In our contact proposal, a plot of the refractive index of $\text{GaAs}_{1-x}\text{P}_x$ as a function of x is given, in which $\epsilon_\infty = 9.04$ was used for GaP and the refractive index of GaP at $10.6\mu\text{m}$ is obtained by using $n = \sqrt{\epsilon_\infty}$. Thus, a relationship of $\Delta n = -0.28X$ was obtained. A preliminary study of the cutoff film thickness of the waveguide modes indicates the plot is wrong. An assumption of $\Delta n = -0.4X$ gives a better fit to the experimental results. Figure A6 is a plot of the minimum film thickness required to support a mode, as a function of the substrate index. The film has an index of $n_{\text{GaAs}} = 3.27$. Experimentally, for a $7\mu\text{m}$ thick waveguide, we observed only one mode, and Figure A6 indicates the n_s should be larger than 3.10. For an $8\mu\text{m}$ thick waveguide, we observed two modes, and from Figure A6 this means n_s should be smaller than 3.14. Now, we roughly know $3.10 < n_s < 3.14$. If we simply take the mean for $n_{\text{GaAs}_{1-x}\text{P}_x} = 3.12$ and $x = 0.35$ from the photoluminescence measurement and $n_{\text{GaAs}} = 3.27$, we obtain

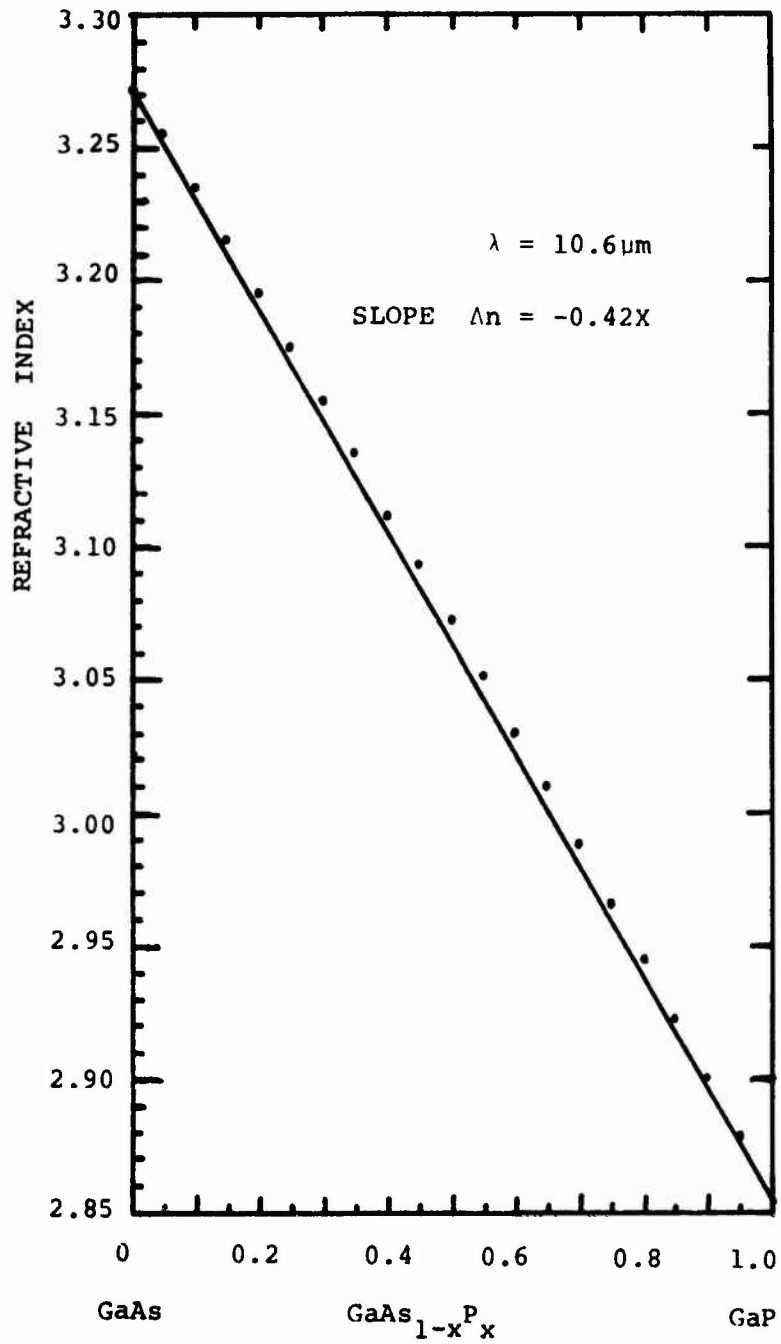
$$\Delta n = -0.44X \quad \text{at } \lambda = 10.6\mu\text{m} \quad (\text{A-10})$$

The infrared reflectivity spectrum of $\text{GaAs}_{1-x}\text{P}_x$ has been reported by Verleur and Barker^{A23}. From their data, Hill^{A24} calculated the refractive index of $\text{GaAs}_{1-x}\text{P}_x$ at various wavelengths with x as a parameter. Figure A7 shows his calculated dispersion curves of GaAs, $\text{GaAs}_{0.65}\text{P}_{0.35}$ and GaP. At $\lambda = 10.6\mu\text{m}$, the refractive index of $\text{GaAs}_{1-x}\text{P}_x$ as a function of x is shown in Figure We obtain a linear approximation for $\text{GaAs}_{1-x}\text{P}_x$ as

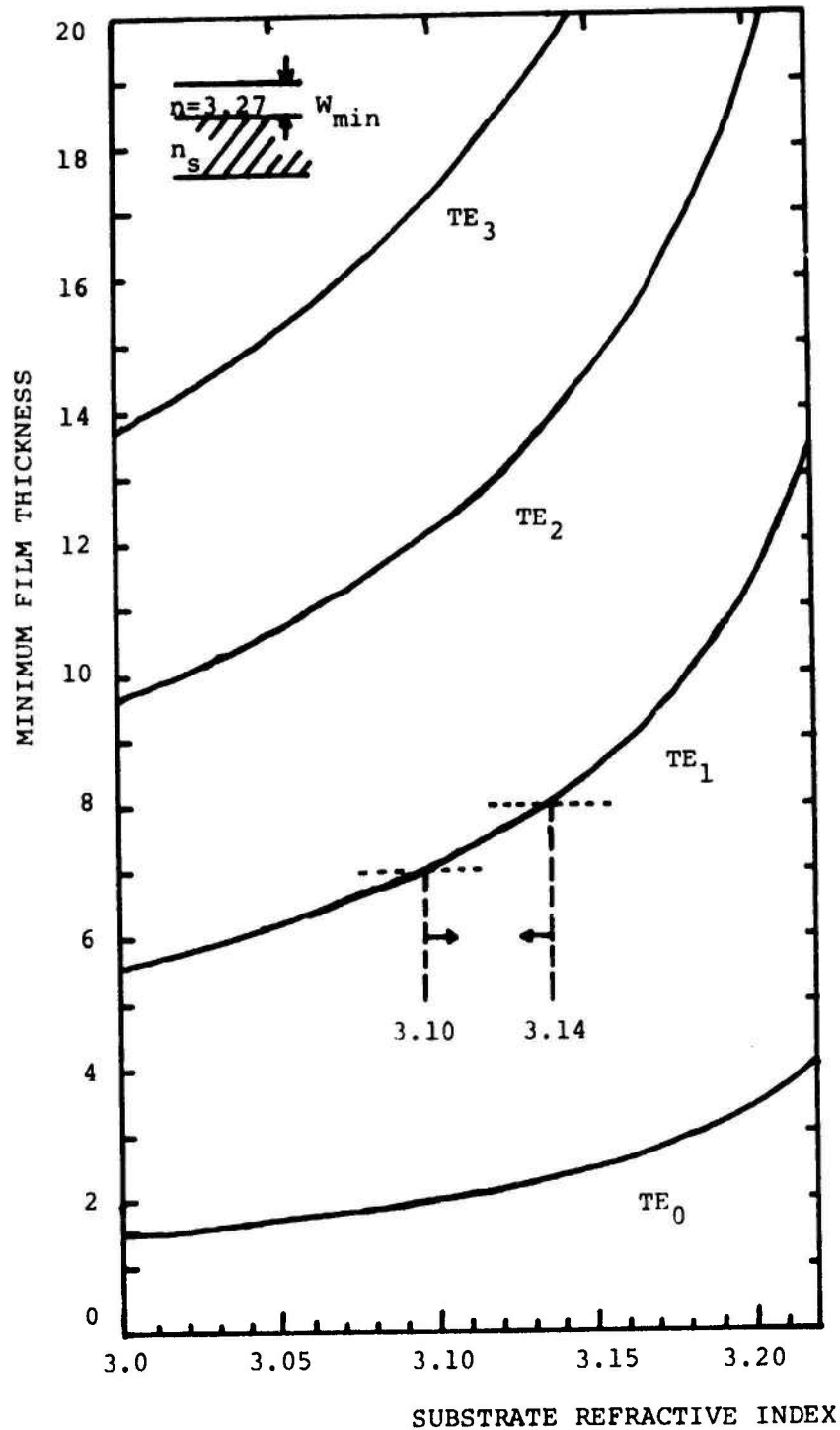
$$\Delta n = -0.42X \quad \text{at } \lambda = 10.6\mu\text{m} \quad (\text{A-11})$$



FigureA6 Minimum film thickness as a function of the substrate refractive index, $n_{\text{GaAs}} = 3.27$ and $\lambda = 10.6\mu\text{m}$.



FigureA7 Dispersion curves of GaAs, GaAs_{0.65}P_{0.35} and GaP.



FigureA8 Index of refraction of $\text{GaAs}_{1-x}\text{P}_x$ as a function of mole fraction of GaP at $\lambda = 10.6\mu\text{m}$.

We believe that Eq A-11 is reasonably accurate. An experimental measurement similar to the work done by McFee et al¹⁵ is under way.

V. CONCLUSION

The refractive index of pure GaAs is $n = 3.479$ at $\lambda = 1.06\mu\text{m}$ and $n = 3.275$ at $\lambda = 10.6\mu\text{m}$. The refractive index of $\text{Al}_x\text{Ga}_{1-x}\text{As}$ is given by $\Delta n = -0.54X$ at $\lambda = 1.06\mu\text{m}$ and $\Delta n = -0.46X$ at $\lambda = 10.6\mu\text{m}$. The refractive index of $\text{GaAs}_{1-x}\text{P}_x$ is given by $\Delta n = -0.37X$ at $\lambda = 1.06\mu\text{m}$ and $\Delta n = -0.42X$ at $\lambda = 10.6\mu\text{m}$.

REFERENCES FOR APPENDIX 3

- A1. D. T. F. Marple, "Refractive Index of GaAs", J. Appl. Phys., 35, pp. 1241-1242, April, 1964.
- A2. B. O. Seraphin and H. E. Bennett, "Optical Constants", in Semiconductors and Semimetals, Vol. 3, ed. by R. K. Willardson and A. C. Beer, Academic Press, New York, 1967, pp. 499.
- A3. J. Zoroofchi and J. K. Butler, "Refractive Index of n-type Gallium Arsenide," J. Appl. Phys., 44, pp. 3697-3699, Aug. 1973.
- A4. F. Stern, Phys. Rev., 133, A1653(1964).
- A5. D. D. Sell, H. C. Casey Jr. and K. W. Wecht, "Concentration Dependence of the Refractive Index for n- and p-type GaAs between 1.2 and 1.8 eV," J. Appl. Phys., 45, pp. 2650-2659, June, 1974.
- A6. F. Oswald and R. Schade, "Über die Bestimmung der optischen Konstanten von Halbleitern des Type $Al^{IV}B^V$ im Infraroten (in German), Z. Naturforsch, 9a, 611 (1954) quoted by H. Welker, "Optical and Electrical Properties of GaAs, InP and GaP", J. of Electronics, 1, pp. 181-185, Sept., 1955.
- A7. P. K. Cheo, J. M. Berak, W. Oshinsky and J. L. Swindal, "Optical Waveguide Structures for CO_2 Lasers," Appl. Opt., 12, pp. 500-509, March, 1973.
- A8. G.D. Boyd. (private communication, 1971. information supplied by J. H. McFee, Bell Lab. Holmdel.)
- A9. W. S. C. Chang, "Integrated Optics at 10.6 μ m Wavelength," IEEE Trans. MTT, Jan., 1975.
- A10. R. E. Fern and A. Onton, "Refractive Index of AlAs", J. Appl. Phys., 42, pp. 3499-3500, August, 1971.
- A11. H. C. Casey, Jr., D. D. Sell, and M. B. Panish, "Refractive Index of $Al_xGa_{1-x}As$ between 1.2 and 1.8 e.V", Appl. Phys. Lett., 24, pp. 63-65, 15 Jan., 1974.
- A12. M. A. Fromowitz, "Refractive Index of $Ga_{1-x}Al_xAs$," to be published in Solid State Comm.

REFERENCES (Continued)

- A13. M. A. Afromowitz (unpublished), quoted by B. W. Hakki and C. J. Hwang, "Mode Control in GaAs Large-Cavity Double-Heterostructure Lasers", J. Appl. Phys., 45, pp. 2168-2173, May, 1974.
- A14. J. K. Butler and H. Kressel, "Transverse Mode Selection in Injection Lasers with Widely Spaced Heterojunctions", J. Appl. Phys., 43, pp. 3403-3411, August, 1972.
- A15. J. H. McFee, W. W. Rigrod, M. A. Pollack and R. A. Logan, "Measurement of Parameters of Heterostructure GaAs-AlGaAs-GaAs Planar Waveguides at 10.6 μ m Wavelength," to be published.
- A16. W. L. Bond "Measurement of the Refractive Indices of Several Crystals", J. Appl. Phys., 36, pp 1674-1677, May, 1965.
- A17. D. A. Yas'kov and A. N. Pikhtin, "Optical Properties of Gallium Phosphide Grown by Floating Zone, I. Refractive Index and Reflection Coefficient", Material Research Bulletin, 4, pp. 781-788, October, 1969.
- A18. O. G. Folberth and F. Oswald, "Uber die Halbleitereigenschaften von Galliumphosphid", (in German), Z. Naturforsch, 9a, 1050 (1954) quoted by H. Welker, "Optical and Electrical Properties of GaAs, InP and GaP", J. of Electronics, 1, pp. 181-185, September, 1955.
- A19. D. A. Kleinman and W. G. Spitzer, "Infrared Lattice Absorption of GaP", Phys. Rev. 118, 110 (1960).
- A20. S. A. Abagyan, G. A. Ivanov, Yu. E. Shanurin and V. I. Amosov, "Refractive Index of GaP in the Infrared Region", Soviet Physics-Semiconductors, 5, pp. 889-890, November, 1971.
- A21. G. D. Clark, Jr., and H. Holonyak, Jr., "Optical Properties of Gallium Arsenide-Phosphide", Phys. Rev., 156, pp. 913-924, 15 April, 1967.
- A22. H. C. Casey Jr., "Refractive Index of GaAs_{0.62}P_{0.38} between 1.2 and 2.0 eV," J. Appl. Phys., 45, pp. 2766-2767, June, 1974.
- A23. H. W. Verleur and A. S. Barker, Jr., "Infrared Lattice Vibrations in GaAs_yP_{1-y} Alloys", Phys. Rev., 149, pp. 715-729, 16 Sept., 1966.
- A24. D. E. Hill, Monsanto Company (unpublished).

APPENDIX A.3.a

**REFRACTIVE INDEX n AND EXTINCTION COEFFICIENT k OF GALLIUM PHOSPHIDE
AS A FUNCTION OF WAVELENGTH λ (After Ref.2)**

λ (microns)	n	k	Reference	λ (microns)	n	k	Reference
0.049	1.028	0.168	(1-4)	0.165	1.187	1.841	(1-4)
0.050	1.000	0.201	(1-4)	0.177	1.390	2.119	(1-4)
0.052	0.991	0.231	(1-4)	0.180	1.479	2.188	(1-4)
0.054	0.999	0.290	(1-4)	0.188	1.727	2.125	(1-4)
0.056	1.023	0.290	(1-4)	0.190	1.732	2.073	(1-4)
0.059	1.026	0.278	(1-4)	0.194	1.696	2.085	(1-4)
0.063	0.972	0.243	(1-4)	0.207	1.709	2.353	(1-4)
0.065	0.901	0.286	(1-4)	0.229	2.246	3.295	(1-4)
0.069	0.839	0.362	(1-4)	0.234	2.631	3.472	(1-4)
0.073	0.797	0.474	(1-4)	0.239	3.191	3.462	(1-4)
0.077	0.801	0.588	(1-4)	0.264	4.130	2.102	(1-4)
0.083	0.825	0.691	(1-4)	0.288	3.862	1.481	(1-4)
0.089	0.854	0.796	(1-4)	0.295	3.785	1.494	(1-4)
0.095	0.896	0.905	(1-4)	0.302	3.743	1.541	(1-4)
0.103	0.951	1.023	(1-4)	0.310	3.770	1.649	(1-4)
0.113	1.025	1.138	(1-4)	0.318	3.906	1.801	(1-4)
0.124	1.143	1.303	(1-4)	0.330	4.653	1.959	(1-4)
0.135	1.250	1.230	(1-4)	0.335	5.078	1.710	(1-4)
0.139	1.195	1.234	(1-4)	0.344	5.192	—	(1-4)
0.146	1.116	1.331	(1-4)	0.354	4.848	—	(1-4)
0.157	1.075	1.439	(1-4)	0.375	4.252	—	(1-4)
0.452		3.12×10^{-2}	(5)	0.850	3.24	—	(9)
0.454		2.36×10^{-2}	(5)	0.900	3.20	—	(9)
0.456		1.87×10^{-2}	(5)	0.950	3.17	—	(9)
0.457		1.59×10^{-2}	(5)	1.00	3.17	—	(9)
0.459		1.43×10^{-2}	(5)	1.10	3.13	—	(9)
0.463		1.16×10^{-2}	(5)	1.20	3.10	—	(9)
0.464		9.49×10^{-3}	(5)	1.30	3.07	—	(9)
0.470		7.68×10^{-3}	(5)	1.40	3.07	—	(9)
0.473		6.37×10^{-3}	(5)	1.60	3.04	—	(9)
0.477		5.47×10^{-3}	(5)	1.60		4.99×10^{-4}	(5)
0.480		4.66×10^{-3}	(5)	1.80	3.03	—	(9)
0.482		4.29×10^{-3}	(5)	1.80		7.56×10^{-4}	(5)
0.488		3.41×10^{-3}	(5)	2.00	3.02	—	(9)
0.492		3.06×10^{-3}	(5)	2.00		1.03×10^{-3}	(5)
0.496		2.54×10^{-3}	(5)	2.50	2.99	—	(9)
0.500		2.47×10^{-3}	(5)	2.50		2.11×10^{-3}	(5)
0.501		2.18×10^{-3}	(5)	3.00	2.97	—	(9)
0.504		1.85×10^{-3}	(5)	3.00		2.53×10^{-3}	(5)
0.510		1.42×10^{-3}	(5)	3.50	2.95	—	(9)
0.511		1.19×10^{-3}	(5)	3.50		2.23×10^{-3}	(5)
0.519		1.04×10^{-3}	(5)	4.00	2.95	—	(9)
0.520	3.65	—	(9)	4.00		2.57×10^{-3}	(5)
0.521		8.57×10^{-4}	(5)	4.50	2.95	—	(9)
0.530		5.34×10^{-4}	(5)	4.50		3.71×10^{-3}	(5)
0.534		3.34×10^{-4}	(5)	5.00	2.94	—	(9)
0.538		2.41×10^{-4}	(5)	5.00		4.22×10^{-3}	(5)
0.544		1.18×10^{-4}	(5)	6.00	2.92	—	(9)
0.547		6.90×10^{-5}	(5)	6.00		7.26×10^{-3}	(5)
0.553		3.44×10^{-5}	(5)	7.00	2.95	—	(9)
0.555		2.19×10^{-5}	(5)	7.00		1.11×10^{-2}	(5)
0.561		1.39×10^{-5}	(5)	8.00	2.94	—	(9)
0.565		9.38×10^{-6}	(5)	8.00		1.64×10^{-2}	(5)
0.571		6.88×10^{-6}	(5)	9.00	2.91	—	(9)
0.574		5.70×10^{-6}	(5)	9.00		2.39×10^{-2}	(5)
0.579		4.96×10^{-6}	(5)	10.00	2.90	—	(9)
0.582		4.71×10^{-6}	(5)	16.00	2.750	—	(7)
0.600	3.46	—	(9)	16.65	2.714	—	(7)
0.620	3.42	—	(9)	17.23	2.679	—	(7)
0.640	3.36	—	(9)	18.00	2.643	—	(7)
0.660	3.34	—	(9)	18.87	2.600	—	(7)
0.680	3.34	—	(9)	20.00	2.529	—	(7)
0.700	3.33	—	(9)	20.87	2.500	—	(7)
0.750	3.28	—	(9)	21.72	2.386	—	(7)
0.800	3.27	—	(9)	22.51	2.207	—	(7)

λ (microns)	n	k	Reference	λ (microns)	n	k	Reference
1.02	3.498	—	(10)	7.0	3.217	—	(15)
1.04	3.488	—	(10)	8.0	3.315	—	(18)
1.06	3.479	—	(10)	8.0	3.280	—	(14)
1.10	3.463	—	(10)	8.0	3.183	—	(15)
1.15	3.446	—	(10)	9.0	3.312	—	(18)
1.20	3.433	—	(10)	9.0	3.280	—	(14)
1.40	3.394	—	(10)	9.0	3.143	—	(15)
1.50	3.381	—	(10)	10.0	3.309	—	(18)
1.70	3.362	—	(10)	10.0	3.095	—	(15)
2.0	3.314	—	(15)	11.0	3.305	—	(18)
2.0	3.325	—	(18)	11.0	3.047	—	(15)
2.0	3.410	—	(14)	12.0	3.300	—	(18)
3.0	3.324	—	(18)	12.0	2.991	—	(15)
3.0	3.350	—	(14)	13.0	3.295	—	(18)
3.0	3.303	—	(15)	13.0	2.933	—	(15)
3.0	3.313	—	(12)	14.0	3.289	—	(18)
4.0	3.323	—	(18)	14.0	2.863	—	(15)
4.0	3.300	—	(14)	15.0	3.283	—	(18)
4.0	3.289	—	(15)	15.0	2.790	—	(15)
4.0	3.302	—	(12)	16.0	2.707	—	(15)
5.0	3.322	—	(18)	17.0	2.621	—	(15)
5.0	3.290	—	(14)	18.0	2.521	—	(15)
5.0	3.269	—	(15)	19.0	2.409	—	(15)
5.0	3.298	—	(12)	20.0	2.287	—	(15)
6.0	3.320	—	(18)	20.0	3.234	—	(18)
6.0	3.280	—	(14)	21.0	2.151	—	(15)
6.0	3.246	—	(15)	22.0	2.029	—	(15)
7.0	3.318	—	(18)	23.0	3.182	—	(18)
7.0	3.250	—	(14)	25.0	3.133	—	(18)

REFERENCES

1. H. R. Philipp and H. Ehrenreich, *Phys. Rev. Letters* **8**, 92 (1962).
2. H. R. Philipp and H. Ehrenreich, *Phys. Rev.* **129**, 1550 (1963).
3. H. Ehrenreich, H. R. Philipp, and J. C. Phillips, *Phys. Rev. Letters* **8**, 59 (1962).
4. H. R. Philipp and H. Ehrenreich, Chapter 4 of this volume.
5. J. Tauc and A. Abraham, *Proc. Intern. Conf. Semicond. Phys., Prague, 1960* p. 375. Czech Acad. Sci., Prague and Academic Press, New York, 1961.
6. R. E. Morrison, *Phys. Rev.* **124**, 1314 (1961).
7. H. F. Bennett and J. O. Porteus, *J. Opt. Soc. Am.* **51**, 123 (1961).
8. J. O. Porteus, *J. Opt. Soc. Am.* **53**, 1394 (1963).
9. M. D. Sturge, *Phys. Rev.* **127**, 768 (1962).
10. D. T. F. Marple, *J. Appl. Phys.* **35**, 1241 (1964).
11. T. S. Moss and T. D. H. Hawkins, *Infrared Phys.* **1**, 111 (1961).
12. K. G. Hambleton, C. Hillsom, and B. R. Holeman, *Proc. Phys. Soc. (London)* **77**, 1147 (1961).
13. K. H. Zaininger and A. G. Revesz, *J. Phys. (France)* **25**, 208 (1964).
14. F. Oswald and R. Schade, *Z. Naturforsch.* **9a**, 611 (1954).
15. L. C. Barcus, A. Perlmutter, and J. Callaway, *Phys. Rev.* **111**, 167 (1958).
16. M. Hass and B. W. Henvis, *J. Phys. Chem. Solids* **23**, 1069 (1962).
17. G. Picus, F. Burstein, B. W. Henvis, and M. Hass, *J. Phys. Chem. Solids* **8**, 282 (1959).
18. B. Pinon and F. Cabannes, *Compt. Rend.* **255**, 2932 (1962).
19. S. J. Fray, F. A. Johnson, J. E. Quarrington, and N. Williams, *Proc. Phys. Soc. (London)* **77**, 215 (1961).
20. W. G. Spitzer and J. M. Whelan, *Phys. Rev.* **114**, 59 (1959).
21. M. V. Hobden and M. D. Sturge, *Proc. Phys. Soc. (London)* **78**, 615 (1961).
22. L. J. Vieland and I. Kudman, *J. Phys. Chem. Solids* **24**, 437 (1963).
23. R. Braunstein, J. I. Pankove, and H. Nelson, *Appl. Phys. Letters* **3**, 31 (1963).
24. W. J. Turner and W. E. Reese, *J. Appl. Phys.* **35**, 350 (1964).
25. D. E. Hill, *Phys. Rev.* **133**, A866 (1964).
26. G. Lucovsky, *Appl. Phys. Letters* **5**, 37 (1964).
27. I. Kudman and T. Seidel, *J. Appl. Phys.* **33**, 771 (1962).
28. G. Lucovsky, A. J. Varga, and R. F. Schwartz, *Solid State Commun.* **3**, 9 (1965).
29. M. Cardona, *Proc. Intern. Conf. Semicond. Phys., Prague, 1960* p. 388. Czech Acad. Sci., Prague and Academic Press, New York, 1961.

APPENDIX A.3.b

Refractive Index of GaP
(After Ref. 16)

$\lambda(\mu)$	GaP
0.4	
0.45	
0.5	3.4595 (54 μ)
0.6	3.3495
0.7	3.2442
0.8	2.1830
0.9	3.1430
1.0	2.1192
1.1	3.0981
1.2	3.0844
1.4	3.0646
1.6	3.0509
1.8	3.0439
2.0	3.0379
2.2	3.0331
2.4	3.0296
2.6	3.0271
2.8	3.0236
3.0	3.0215
3.2	3.0197
3.4	3.0181
3.6	3.0166
3.8	3.0159
4.0	3.0137

APPENDIX A.3.c

REFRACTIVE INDEX n AND EXTINCTION COEFFICIENT k OF GALLIUM ARSENIDE
AS A FUNCTION OF WAVELENGTH λ AT 300°K (After Ref.2)

λ (microns)	n	k	Reference	λ (microns)	n	k	Reference
0.049	1.049	0.156	(1-4)	0.115	0.923	0.881	(1-4)
0.051	1.033	0.203	(1-4)	0.124	0.913	0.974	(1-4)
0.054	1.037	0.228	(1-4)	0.138	0.900	1.136	(1-4)
0.056	1.043	0.243	(1-4)	0.155	0.899	1.435	(1-4)
0.058	1.051	0.250	(1-4)	0.177	1.063	1.838	(1-4)
0.059	1.058	0.245	(1-4)	0.188	1.247	2.047	(1-4)
0.062	1.025	0.212	(1-4)	0.197	1.441	1.988	(1-4)
0.065	0.981	0.234	(1-4)	0.200	1.424	1.976	(1-4)
0.069	0.936	0.267	(1-4)	0.207	1.395	2.048	(1-4)
0.073	0.889	0.324	(1-4)	0.216	1.402	2.203	(1-4)
0.078	0.850	0.411	(1-4)	0.225	1.451	2.416	(1-4)
0.083	0.836	0.503	(1-4)	0.236	1.561	2.722	(1-4)
0.089	0.840	0.602	(1-4)	0.248	1.882	3.279	(1-4)
0.096	0.864	0.709	(1-4)	0.258	2.726	3.388	(1-4)
0.103	0.895	0.791	(1-4)	0.270	3.291	2.860	(1-4)
0.282	3.486	2.527	(1-4)	0.820	—	0.632×10^{-1}	(11)
0.295	3.526	2.074	(1-4)	0.825	—	0.615×10^{-1}	(11)
0.310	3.513	1.857	(1-4)	0.830	—	0.593×10^{-1}	(11)
0.318	3.451	1.827	(1-4)	0.835	—	0.578×10^{-1}	(11)
0.326	3.389	1.845	(1-4)	0.840	—	0.556×10^{-1}	(11)
0.344	3.391	1.906	(1-4)	0.845	—	0.535×10^{-1}	(11)
0.365	3.514	2.017	(1-4)	0.850	—	0.676×10^{-1}	(9)
0.400	4.149	2.137	(1-4)	0.852	—	0.661×10^{-1}	(9)
0.409	4.320	1.999	(1-4)	0.854	—	0.648×10^{-1}	(9)
0.419	4.459	1.930	(1-4)	0.856	—	0.640×10^{-1}	(9)
0.425	4.755	1.934	(1-4)	0.858	—	0.627×10^{-1}	(9)
0.443	4.929	1.195	(1-4)	0.860	—	0.620×10^{-1}	(9)
0.459	4.748	—	(1-4)	0.862	—	0.615×10^{-1}	(9)
0.460	—	0.510	(9)	0.864	—	0.606×10^{-1}	(9)
0.465	—	0.536	(9)	0.866	—	0.605×10^{-1}	(9)
0.470	—	0.500	(9)	0.868	—	0.601×10^{-1}	(9)
0.475	—	0.490	(9)	0.870	—	0.483×10^{-1}	(9)
0.480	—	0.464	(9)	0.872	—	0.338×10^{-1}	(9)
0.485	—	0.442	(9)	0.874	—	0.207×10^{-1}	(9)
0.490	—	0.425	(9)	0.876	—	0.105×10^{-1}	(9)
0.495	—	0.412	(9)	0.878	—	7.340×10^{-2}	(9)
0.495	4.427	—	(1-4)	0.880	—	4.549×10^{-2}	(9)
0.500	—	0.400	(9)	0.882	—	2.783×10^{-2}	(9)
0.505	—	0.387	(9)	0.884	—	1.808×10^{-2}	(9)
0.510	—	0.375	(9)	0.886	—	1.177×10^{-2}	(9)
0.515	—	0.363	(9)	0.888	—	0.664×10^{-2}	(9)
0.520	—	0.351	(9)	0.890	—	0.416×10^{-2}	(9)
0.525	—	0.339	(9)	0.892	—	0.262×10^{-2}	(9)
0.530	—	0.330	(9)	0.894	—	0.173×10^{-2}	(9)
0.535	—	0.320	(9)	0.895	3.603	—	(10)
0.540	—	0.313	(9)	0.896	—	0.112×10^{-2}	(9)
0.540	4.127	—	(1-4)	0.898	—	0.082×10^{-2}	(9)
0.590	3.848	—	(1-4)	0.900	—	0.639×10^{-2}	(9)
0.653	3.746	—	(1-4)	0.900	3.595	—	(10)
0.729	3.627	—	(1-4)	0.902	—	0.518×10^{-2}	(9)
0.775	—	0.667×10^{-1}	(11)	0.904	—	0.433×10^{-2}	(9)
0.780	—	0.696×10^{-1}	(11)	0.910	3.581	—	(10)
0.785	—	0.693×10^{-1}	(11)	0.920	3.569	—	(10)
0.790	—	0.692×10^{-1}	(11)	0.940	3.550	—	(10)
0.795	—	0.688×10^{-1}	(11)	0.940	3.534	—	(10)
0.800	—	0.682×10^{-1}	(11)	0.940	3.520	—	(10)
0.805	—	0.666×10^{-1}	(11)	1.000	3.509	—	(10)
0.810	—	0.658×10^{-1}	(11)	1.000	3.326	—	(11)
0.815	—	0.643×10^{-1}	(11)	1.000	3.900	—	(14)

λ (microns)	n	k	Reference	λ (microns)	n	k	Ref.
23.29	1.979		(7)	27.34		10.84	(7)
24.01	1.650		(7)	27.36	15.19		(7)
24.57	1.129		(7)	27.37		8.20	(7)
24.82		0.064	(7)	27.44		5.13	(7)
25.00	0.100		(7)	27.45	13.47		(7)
25.26		1.379	(7)	27.46		2.57	(7)
25.42	0.043		(7)	27.53		1.04	(7)
26.23		3.400	(7)	27.54	10.87		(7)
26.51	0.129		(7)	27.57		0.68	(7)
26.66		5.000	(7)	27.65		0.45	(7)
26.89		6.614	(7)	27.69	8.50		(7)
26.98	0.457		(7)	27.82		0.200	(7)
27.04		8.893	(7)	28.09		0.114	(7)
27.14		11.50	(7)	28.21	6.19		(7)
27.18	1.83		(7)	28.64		0.107	(7)
27.19	4.07		(7)	29.12		0.050	(7)
27.21	7.62		(7)	29.34	4.67		(7)
27.26	13.12		(7)	29.69		0.050	(7)
27.26		14.68	(7)	29.94	4.39		(7)
27.29		17.33	(7)	30.00	4.36	0.021	(7)
27.32	16.58	13.89	(7)				

REFERENCES

1. H. R. Philipp and H. Ehrenreich, *Phys. Rev. Letters* **8**, 92 (1962).
2. H. R. Philipp and H. Ehrenreich, *Phys. Rev.* **129**, 1550 (1963).
3. H. Ehrenreich, H. R. Philipp, and J. C. Phillips, *Phys. Rev. Letters* **8**, 59 (1962).
4. H. R. Philipp and H. Ehrenreich, Chapter 4 of this volume.
5. W. G. Spitzer, M. Gershenzon, C. J. Forsch, and D. F. Gibbs, *J. Phys. Chem. Solids* **11**, 339 (1959).
6. H. Y. Fan, *Rept. Progr. Phys.* **19**, 107 (1956).
7. D. A. Kleinman and W. G. Spitzer, *Phys. Rev.* **118**, 110 (1960).
8. O. G. Folberth and F. Oswald, *Z. Naturforsch.* **9a**, 1050 (1954).
9. H. Weiker, *J. Electron.* **1**, 181 (1955).
10. F. Oswald and R. Schade, *Z. Naturforsch.* **9a**, 611 (1954).